

Characterization of Uncertainty
in Measurements of Wind
from the NSF/NCAR Gulfstream V Research Aircraft

Al Cooper, Dick Friesen, Matt Hayman, Jorgen Jensen, Don Lenschow, Allen Schanot,
Scott Spuler, Jeff Stith
(and, we hope, many others)

DRAFT 4/6/2015

Contents

1	Introduction	4
2	Components of the wind-sensing systems	6
2.1	General comments	6
2.2	The radome-based system	8
2.3	The gust-pod system	18
2.4	The laser air-motion sensor	27
3	Uncertainty components and summary	40
3.1	General structure of an analysis of uncertainty	40
3.2	Preliminary estimates of uncertainty	40
3.3	Elemental sources, vertical wind	44
3.4	Elemental sources, horizontal wind	49
3.5	Summary	55
4	Sensitivity coefficients	59
4.1	Angle of Attack	59
4.2	Sideslip Angle	71
4.3	True Airspeed from the Gust Pod	75
4.4	Summary of sensitivity coefficients	80
5	Studies of the Vertical Wind	81
5.1	Overview	81
5.2	The vertical velocity of the aircraft	81
5.3	Timing of measurements	87
5.4	Correcting pitch for the Schuler oscillation	89
6	Studies of the Horizontal Wind	105
6.1	Analysis of circle maneuvers	105
6.2	The complementary filter	117

A Appendix: Conventions for uncertainty analysis	120
A.1 Why perform analyses of uncertainty?	120
A.2 Error, accuracy, and uncertainty	120
A.3 Standards for evaluating uncertainty	121
A.4 Classification of sources of error and of uncertainty	121
A.5 Recommended Guidelines	123
A.6 Estimating uncertainties	126
A.7 The composite or net uncertainty	128
A.8 Propagation of uncertainty estimates	128
A.9 Monte Carlo techniques	131
A.10 Reference Material	132
B Appendix: Reproducibility	135

1 Introduction

Wind is the motion of the atmosphere relative to the Earth. Most research aircraft have the capability to measure wind, and these measurements have many uses in research projects using aircraft. They help define the flow and so provide context for other measurements, and they are often used to study fluxes of atmospheric constituents, turbulence, wave motions, cloud updrafts and downdrafts, convergence and divergence, and many other topics. They can provide important information transferred to models for data assimilation or for validation tests of model results.

This report applies to the Gulfstream V research aircraft owned by the National Science Foundation and operated by the Research Aviation Facility (RAF), Earth Observing Laboratory (EOL), National Center for Atmospheric Research (NCAR). This aircraft is referred to here as the NSF/NCAR GV or simply the GV. Its range and endurance makes it possible to measure wind over large distances and so to characterize mesoscale and even larger features in the atmosphere. However, its high speed (typically Mach 0.8, or about 240 m s^{-1} for flight near 40,000 ft) poses special problems for wind measurement. The flow distortion around the aircraft perturbs pressure measurements that are central to the measurement of wind, and the measurement of air temperature, needed in the calculation of wind, requires corrections of typically more than 20°C to account for dynamic heating of the sensors. Accurate measurement of wind thus is particularly challenging on this and other high-speed aircraft.

This report documents how measurements of wind are made from the NSF/NCAR Gulfstream V research aircraft (hereafter, GV) and provides a characterization of the uncertainty associated with those measurements. The characterization applies to the system as it existed in 2014, in particular as it operated in the DEEPWAVE research project flown from New Zealand in June-July 2014. Key features of the instrumentation influencing the uncertainty in the measurements as characterized here are the presence of “OmniSTAR” GPS (Global Positioning System) measurements, providing measurements of the velocity of the aircraft relative to the earth, a calibration of airspeed provided by the Laser Air Motion Sensor ([Cooper et al. \[2014\]](#)), and a newly developed all-weather wind sensor or “gust pod” employing a Rosemount 858 probe mounted under the wing of the GV. These complemented the standard wind-sensing system comprised of a Honeywell Laseref IV inertial reference unit, GPS measurements from Novatel and Garmin units, and a gust-sensing system based on pressure ports in the nose radome. The results obtained here do not necessarily apply to measurements from earlier projects when not all these components were available in their present form, but they should apply to measurements subsequent to 2014.

The intent in this report is to follow the conventions established by the International Committee on Weights and Measures and by the National Institute of Standards and Technology. Appendix A summarizes key aspects of those recommendations and how they are addressed in this report. We also present additional information resulting from various studies of the measurements that have tested the validity of the measurements or have been used for calibration.

Section 2 describes the components of the wind-measuring system in more detail, with examples of the measurements and information on the specifications for the sensors involved. That section is followed by a summary of the uncertainty in wind measurements, with a tabulation

1 INTRODUCTION

of individual error sources and references to later parts of the document where studies reported here have led to estimates of limits on those error sources. It is our hope that this section will provide a summary of the results that can either stand alone or provide a guide to the further information in this report that has led to the conclusions summarized there.

Section 4 summarizes how the measurements have been calibrated, tested, and intercompared. Some related studies affecting the measurements are then presented in the next two sections. The section discussing vertical wind focuses on studies of the measurement of aircraft vertical motion, needed to calculate the vertical wind, and includes a correction procedure that can improve the measurement of pitch and hence the vertical wind. The section discussing horizontal wind uses circle maneuvers to check the measurement of horizontal wind and develop corrections to the heading and sideslip.

2 Components of the wind-sensing systems

2.1 General comments

2.1.1 Overview

Three wind-sensing systems are available for use on the GV:

1. The “standard” wind sensing system that uses pressure ports on the radome combined with airspeed measured using a pitot tube and ground-speed measured by an inertial reference unit and a global positioning system (GPS) receiver.
2. A gust-pod system consisting of a Rosemount 858 airflow sensor mounted under the wing combined with an inertial system co-located with the airflow sensor and linked to GPS measurements via a Kalman filter.
3. A laser air motion sensor (LAMS) described by Spuler et al. [2011] combined with its own IRU/GPS system. See also Cooper et al. [2014].

All three also depend on a measurement of temperature and, for the first two, humidity which is used to correct for the influence of moisture on the specific heats and gas constant of moist air. Those two also share dependence on the measurement of ambient pressure as delivered by static sources on the fuselage. Although the other measurement components differ, for each of these the measurement of wind involves the vector sum of two components, the motion of the air relative to the aircraft and the motion of the aircraft relative to the Earth. The former is the “relative wind” and is measured as a three-component vector having magnitude equal to the “true airspeed” and angles relative to the aircraft reference frame characterized by the angle of attack and the sideslip angle. The angle of attack is considered positive if the relative wind is from below the aircraft, and the sideslip angle is considered positive if the relative wind is from the starboard side of the aircraft. The relative wind defined in the coordinate system of the aircraft (conventionally with \hat{x}' forward, \hat{y}' in the starboard direction, and \hat{z}' obtained from the cross product $\hat{x}' \times \hat{y}'$ and so approximately downward but oriented to align with the aircraft reference frame) must be transformed to an Earth-based reference system (conventionally with \hat{x} toward east, \hat{y} toward north, and \hat{z} upward) so that the components can be combined to yield the Earth-relative wind. This transformation is a function of the attitude angles of the aircraft (heading ψ , pitch θ , and roll ϕ), measured by an inertial reference unit in all three cases discussed here. Once in an Earth-based reference system, the relative wind vector is added to the vector representing the aircraft motion relative to the Earth to obtain the wind. The sources of the various measurements entering this processing sequence vary among the three systems and will be discussed separately below for each system.

2.1.2 The Relative Wind

In the standard aircraft coordinate system with x forward, y starboard, and z downward, the three corresponding components of the relative wind \mathbf{v} (cf. Lenschow [1972] and RAF Bulletin 23) are:

$$\mathbf{v} = \begin{pmatrix} u_r \\ v_r \\ w_r \end{pmatrix} = \begin{pmatrix} V^* \\ V^* \tan \beta \\ V^* \tan \alpha \end{pmatrix} \quad (1)$$

where, if V is the true airspeed, $V^* = V / \sqrt{1 + \tan^2 \alpha + \tan^2 \beta}$ is the component of true airspeed along the aircraft longitudinal (x) axis, α is the angle of attack and β the sideslip angle. The sign convention is such that the relative wind is positive when *from* the direction of the axis for each component. (The magnitude of \mathbf{v} is thus V as required.) The relative wind is therefore determined from measurements of true airspeed, angle of attack, and sideslip angle.

2.1.3 Transformation to an Earth reference frame

The orientations of the aircraft, the gust pod, and the LAMS are measured by IRUs located respectively in the fuselage and in the pod itself. Each independently measures heading, pitch, and roll, so the calculations of wind from the three systems can be fully independent except that, because it is considered to have the smallest uncertainty, the true airspeed measured from the fuselage system is used also for the gust pod. In each case, the IRU measurements and GPS ground-speed components are used to transform the measurements to the reference frame of the Earth.

The required transformation is described by three rotation matrices, defined in [RAF Bulletin 23](#) Eqs. 2.5 and 2.6:¹

$$\mathbf{T}_1 = \begin{pmatrix} 1 & 0 & 0 \\ 0 & \cos \phi & -\sin \phi \\ 0 & \sin \phi & \cos \phi \end{pmatrix}$$

$$\mathbf{T}_2 = \begin{pmatrix} \cos \theta & 0 & \sin \theta \\ 0 & 1 & 0 \\ -\sin \theta & 0 & \cos \theta \end{pmatrix}$$

$$\mathbf{T}_3 = \begin{pmatrix} \cos \psi & -\sin \psi & 0 \\ \sin \psi & \cos \psi & 0 \\ 0 & 0 & 1 \end{pmatrix}$$

where $\{\phi, \theta, \psi\}$ are {roll, pitch, heading}.

The transformation needs to be in the following order to conform to conventional definitions of the attitude angles:

¹An additional correction is applied to account for the effect of the rotation rate of the aircraft on the measurements. This correction is needed when the reference unit for motion relative to the Earth, the IRU, is separated from the measurement of relative wind on the radome or gust pod. For the gust pod, this is negligible because the IRU is co-located with the gust-measuring system. See the cited reference for details.

1. Rotate by \mathbf{T}_1 using the roll angle ϕ (ROLL or CROLL_GP) to level the wings by a rotation about the x axis.
2. Rotate by \mathbf{T}_2 using the pitch angle θ (PITCH or CPITCH_GP) to level the aircraft by a rotation about the y axis.
3. Rotate by \mathbf{T}_3 using the heading angle ψ (THDG or CTHDG_GP) to obtain components in a true-north reference frame. At this point, the relative-wind vector in an Earth-reference coordinate system is $\mathbf{v}_r = \mathbf{T}_3(\mathbf{T}_2(\mathbf{T}_1\mathbf{v}))$ where \mathbf{v} is given by (1).

The measured ground-speeds (with components VNS, VEW, VSPD) then can be added to the relative wind to get the true Earth-relative wind. In the “R” file associated with this document, the required transformations are coded to provide a processing option, but the RAF “nimbus” routine “gust.c” provides the transformation as implemented in standard processing.

The final equations, defining the Earth-relative wind \mathbf{v}_E in terms of the three wind variables {WDx, WSx, WIx} where x denotes the measuring system (radome, gust-pod, or LAMS) and subscripts x or y the respective east or north component of the wind, are:

$$\mathbf{v}_E = \mathbf{v}_r + \begin{pmatrix} -VNS_x \\ -VEW_x \\ VSPD_x \end{pmatrix} \quad (2)$$

$$WD_x = \arctan 2(v_{E,y}, v_{E,x}) \quad (3)$$

$$WS_x = \sqrt{(v_{E,x}^2 + v_{E,y}^2)} \quad (4)$$

$$WI_x = v_{E,z} \quad (5)$$

2.2 The radome-based system

2.2.1 Overview

The primary measurement of wind on the GV is that based on measurement of true airspeed via a pitot tube, airflow angles via pressure differences measured on the nose radome, attitude angles measured by an inertial reference unit, and ground-speed components measured by the same inertial reference unit and also by a Global Positioning System receiver. A cursory description of this system was provided by [Cooper et al. \[2014\]](#). A more extensive description will be provided here. Table 1 provides a summary of the measurements used to determine the wind and the characteristics of the sensors used, and the [EOL instrument web pages](#) (cf. "State Parameters", "Wind") provide additional information on these measurements.

Measurement (VARIABLE)	Instrument	Range, Characteristics	Standard Uncertainty	Comments
pitch, roll (PITCH, ROLL)	Honeywell Laseref IV HG2001 GD03	ring gyros, strap-down system	0.05°	mixed bias and random error
heading (THDG)	"	"	0.2°	"
ambient pressure (PSF)	Paroscientific 1000-15A-28 (absolute)	0–15 psi \approx 0–1035 hPa	0.10 hPa	specs. assumed st. uncertainty
dynamic pressure (QCF, QCR)	Honeywell PPT0005-DXX2VB-5021	0–5 PSI \approx 0–345 hPa	0.34 hPa 0.68 hPa max.	"
pressure differences ($\{A,B\}$ DIFR)	Honeywell PPT0001-DXX2VB-5021	\pm 1~psi \approx \pm 68.95 hPa	0.07 hPa 0.14 hPa max.	the first is "typ.", average over the range
horizontal GV velocity components (VNS, VEW)	Laseref IV (see above)	strap-down accelerometers	2.1 m s^{-1}	0.1 m s^{-1} with slow updating to GPS
" (GGVNSB, GGVEWB)	Novatel OEM-3 differential GPS	(L1/L2) correction via OmniSTAR XP	0.03 m s^{-1}	$<0.1 \text{ m s}^{-1}$ when OmniSTAR is not available
vertical GV speed (VSPD)	Laserref IV (see above)	strap-down accelerometers	0.76 m s^{-1}	with baro-loop updating
" (GGVSPDB)	Novatel GPS (see above)		0.03 m s^{-1} with OmniSTAR	0.1 m s^{-1} without OmniSTAR
temperature (ATX)	HARCO 100009-1	–80 to +40°C, anti-iced	0.3°	needed for true airspeed
dewpoint (DPX)	Buck Research 1011C	–70 to +30°C	$<5^\circ$	for level flight

Table 1: Characteristics of measurements from the radome-based system that are used for the standard calculation of the wind. See the discussion of each measurement in the text of Sect. 2.2.

2.2.2 Attitude angles

Attitude angles (roll, pitch, and heading) are provided by the IRU discussed in the preceding sub-section, with specifications as listed in Table 1. There are duplicate inertial systems, so a measure of uncertainty is how well they agree. For DEEPWAVE flight 16, the mean difference in pitch was 0.2° and the standard deviation in the difference between measurements was about 0.015° (for measurements with absolute value of the roll smaller than 3°), and if the measurements are filtered to remove variations with period exceeding about 1000 s the slowly varying component of the difference has standard deviation of about 0.012° while the fast-varying component has standard deviation of 0.008° . This was characteristic of most flights, although there were two (8 and 20) that had slightly larger standard deviations. The project averages were 0.02° for the slow component and about 0.007° for the fast component. This is an indication that the system performs better than indicated by the specifications, and indeed additional evidence for this is provided in Section 3. The difference in pitch and enhanced standard deviation in turns likely arises from small mis-alignment of the units relative to the longitudinal axis of the aircraft. As discussed in Section 3, the error in pitch tends to precess with a period of about 84.4 min, so the slowly varying component tends to be dominated by this precession which, for periods short compared to 84.4 min, introduces a bias while the faster varying component has the character of a random error.

2.2.3 Ambient pressure

Ambient or “static” pressure is measured on the GV at pressure ports called static buttons that are located at positions on the fuselage where in normal flight the pressure is approximately the pressure present outside the airflow disturbance produced by the aircraft. Because there are residual effects of airflow that change with angle of attack and Mach number, corrections are applied to these measurements to obtain better representation of the true ambient pressure. These corrections are described in [this document on processing algorithms](#), Sect. 4.3, and in [Cooper et al. \[2014\]](#). The latter reference has additional information on the locations of the sensors and the system configuration. The transducer characteristics are listed in Table 1, and the transducer is temperature-compensated to maintain these characteristics in flight when the cabin-mounted transducer can encounter fluctuating temperature. It is a digital transducer with resolution of 0.001 hPa, equivalent to about 20-bit resolution, when sampling at 1 Hz. The characteristic response time of the sensor is 0.02 s and measurements are normally sampled at 50 Hz and filtered to 25 Hz. However, lines of length XXX and diameter XXX connect the transducer to the static buttons, and these lines affect the response time significantly, as discussed in Sect. . More information is available on the EOL instrument pages; see [this link](#).

2.2.4 Dynamic pressure

The dynamic pressure is the pressure difference above ambient that develops if air is compressed and adiabatically brought to rest relative to the moving aircraft. The total pressure, the sum of ambient and dynamic pressure, is sensed using a pitot tube, a tube pointed in the direction of the relative airflow and specially designed to be relatively insensitive to small-angle changes in

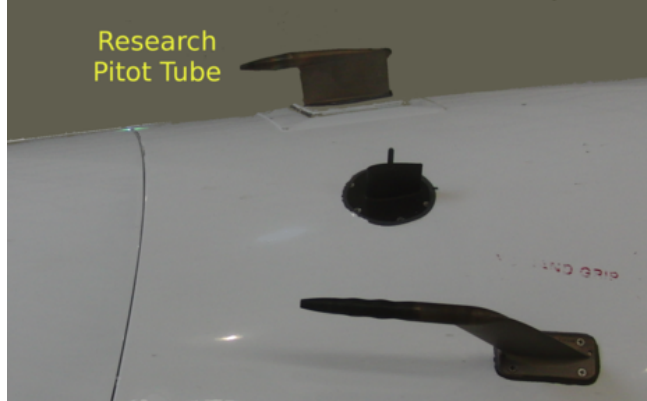


Figure 1: A pitot tube used for the measurement of dynamic pressure.

the direction of the relative airflow. Figure 1 shows the location of the research-system pitot tube on the GV as well as one of the avionics-system pitot tubes. The excess pressure above the ambient sensed by a pitot tube or, approximately, by the center port on the radome is $0.5\rho_a v^2$ where ρ_a is the density of air and v the airspeed, so this excess pressure can be used to determine the airspeed of the aircraft. On NSF/NCAR aircraft, the measurement of dynamic pressure is made using differential sensors connected between a static source and a total-pressure source from either a pitot tube (QCF) or the front port on the radome (QCR). The sensor used, with characteristics listed in Table 1, has these additional characteristics: Specified resolution is 0.0011% of full scale or 0.0076 hPa, which is better than 16-bit resolution; maximum sampling rate 120 Hz; response time 50ms and response delay 21 ms at 50 Hz sample rate, or about one sample period. The response time is affected further by the pressure lines between the pressure ports and the transducers; see Sect. XXX for discussion of this effect. The transducer provides 50-Hz output that is then filtered digitally to 25 Hz or 1 Hz in processing.²

Because any errors affecting the measurement of static pressure also affect the difference between dynamic and static pressure, the same corrections that are applied to static pressure (for errors in the pressure delivered by the static ports) are also applied to the dynamic pressure. See the EOL instrument pages for more information. Cooper et al. [2014] argue that the measurements of static and dynamic pressure, corrected for flow distortion or generation of a “static defect” at the static-pressure ports, each have standard uncertainty of 0.3 hPa and precision (for straight and level flight) of 0.1 hPa.

2.2.5 Airflow angles

The radome gust-sensing system consists of five pressure ports installed in a standard GV radome, as shown in Fig. 2. The pressure ports are connected to differential pressure sensors, one between the top and bottom ports (variable ADIFR), one between the left and right ports (variable BDIFR), and one between the center port and the static source (variable QCR).

²The specifications indicate that the appropriate time lag to apply in processing would be 21 ms but there is additional delay introduced by the sample tubing. Most processing including preliminary processing for DEEPWAVE has not introduced a delay for QCF or QCR.

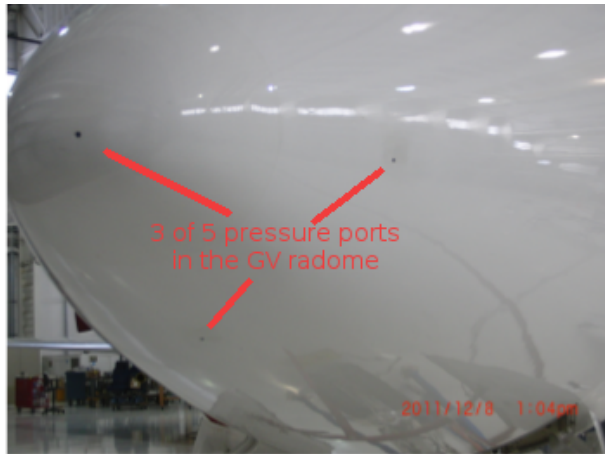


Figure 2: Photograph of the GV radome showing three of the five pressure ports on the radome used for measurement of components of the relative wind.

The latter provides an alternative measurement of dynamic pressure but is not normally used. The measurements ADIFR and BDIFR are obtained from differential pressure transducers, with characteristics as shown in Table 1. The transducers have specified response times of 0.05 s and resolution 0.0015 hPa, with quoted stability of about 0.03 hPa per year. These measurements are used with procedures discussed in Section 4.1.2 to find the angle of attack and sideslip angle of the relative wind. Additional information is available at [this URL](#).

2.2.6 Components of aircraft velocity relative to the Earth

There are two sources of information regarding the ground-speed vector, an inertial reference unit (IRU) and a Global Positioning System (GPS).

1. The IRU: The inertial system on the GV is a Honeywell Laseref IV Model HG2001 GD03, with characteristics as listed in Table 1. There are three units on the aircraft, two of which are recorded via the ARINC data bus to standard data files. These are strap-down ring laser gyro micro inertial systems. The measurements of ground-speed components are affected by errors that arise from initial alignment errors or orientation errors resulting from gyro responses to acceleration and so often exhibit a characteristic Schuler oscillation with magnitude that can be as much as $1\text{--}3 \text{ m s}^{-1}$. This is the primary source of error in the measurements of wind, so for aircraft velocity components it is important to remove these errors by comparison to lower-uncertainty measurements provided by the GPS that are not subject to the Schuler oscillation. In addition, there are signal delays that are accounted for in post processing to align measurements with other recorded data, and there are some inherent filters in the IRU computer that affect the signals transmitted to the GV data system. The orientation of this unit was defined and checked by initial survey to coincide with the aircraft reference axes.
2. The GPS: The primary GPS unit is a Novatel OEM-3 differential GPS unit (L1/L2) with OmniSTAR XP satellite update for (ionospheric) corrections. As used on the GV, it

reports ground-speed components at a rate of 5 Hz, although faster rates are possible. The claimed standard uncertainty for position is 0.15 m for vertical position; the standard uncertainty in velocity is 0.03 m s^{-1} when OmniSTAR corrections are available and $<0.1 \text{ m s}^{-1}$ otherwise.

XXX

2.2.7 Temperature

A measurement of temperature is needed to calculate the wind because the conversion from dynamic pressure to true airspeed involves the temperature, as documented in [this document on processing algorithms](#). The measurements of temperature were checked against expectations for height-vs-pressure changes from the hydrostatic equation by [Cooper et al. \[2014\]](#), with the result that the measurements were validated to an uncertainty of about 0.3°C . Documentation of the temperature uncertainty will be presented in more detail in a separate document.

2.2.8 Humidity (dew point)

The calculation of true airspeed from measured dynamic and static pressure involves the specific heats and gas constant for air, and this can depart from dry-air values when water vapor is present in significant amounts. This correction is usually insignificant for dew-point temperatures below about -20°C but can be important at higher dew-point temperature. The equations used are those in [the document on processing algorithms](#). The correction to true airspeed is approximately a factor of $(1+0.3q_h)$ where q_h is the dimensionless specific humidity, typically about 0.01 at 10°C dewpoint and 700 hPa pressure. In this case the correction to airspeed, typically 150 m/s at this altitude, is about 0.45 m/s, so the correction is not negligible but is relatively insensitive to uncertainty in the measured humidity. The dewpoint measurements become more uncertain than listed here at the low end of this range, but the humidity correction is insignificant there. They are likely better than listed here for the upper range, in level flight, but lags and overshooting introduce errors when conditions are changing rapidly as in climbs or descents.

2.2.9 Examples of measurements

Typical measurements of the attitude angles are shown in Fig. 3. The large difference in pitch is a result of the gust pod being installed in a canister below the wing where it points downward by several degrees relative to the aircraft longitudinal axis. (The pods were designed this way to provide better approaching airflow for cloud-imaging probes and other sampling from the airstream.) There is also a significant difference in heading and in roll for similar reasons.

The measurements of pressures and the true airspeed calculated from these measurements are shown in Fig. 4 for the same period as in the preceding figure. Corrections have been applied to the pressure measurements according to the calibration determined from LAMS measurements, as described by [Cooper et al. \[2014\]](#); these corrections vary with flight conditions but normally are smaller than a few hPa so are not evident in these plots. They are nevertheless crucial to reducing the uncertainty in the true airspeed to about 0.3 m s^{-1} , as shown in that reference.

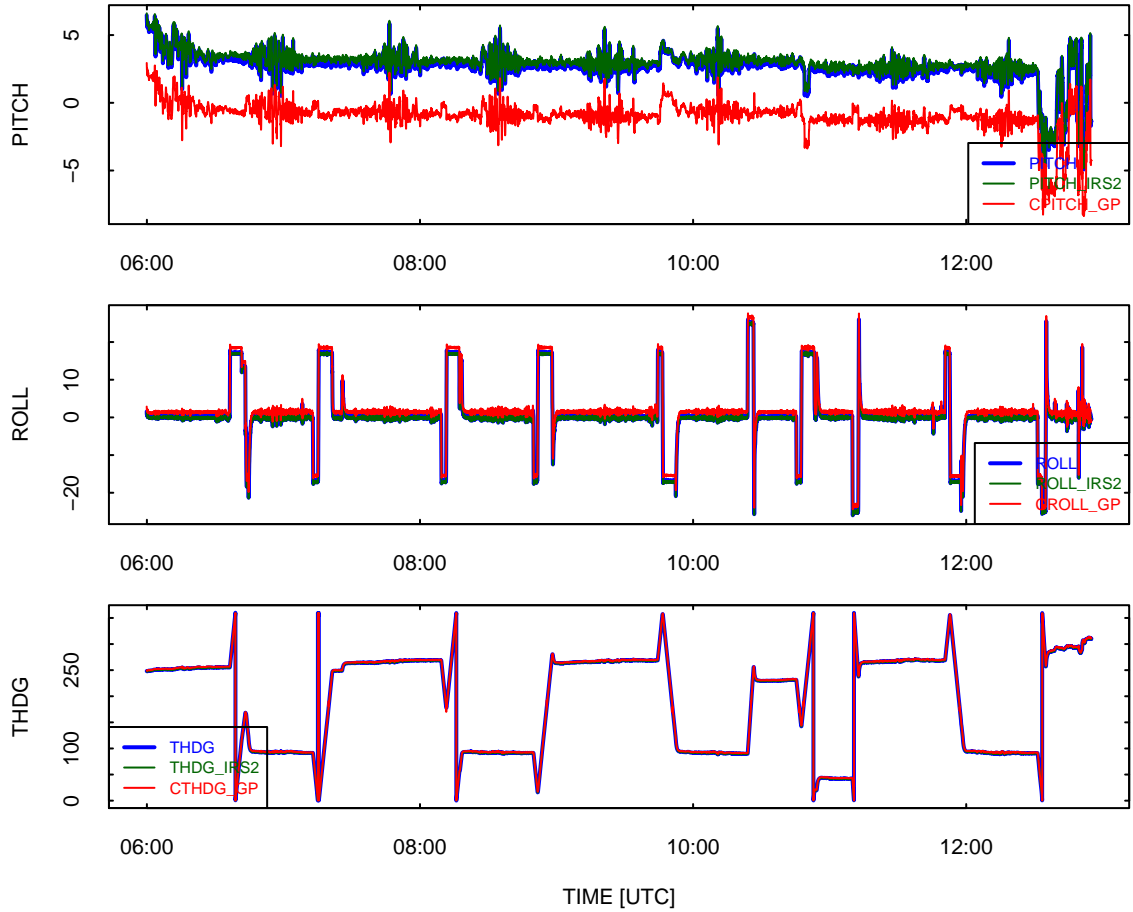


Figure 3: Attitude angles pitch, roll, and heading as measured by three independent systems inertial reference systems. The systems are: (1) the standard Honeywell IRU (PITCH, ROLL, THDG, blue lines); (2) a duplicate backup Honeywell IRU (PITCH_IRS2, ROLL_IRS2, THDG_IRS2, green lines), and the C-MIGITS-III IRU mounted in the gust pod (CPITCH_GP, CROLL_GP, CTHDG_GP, red lines). All units are degrees. Data from DEEPWAVE flight 16 (4 July 2014), 9:00:00 to 10:00:00

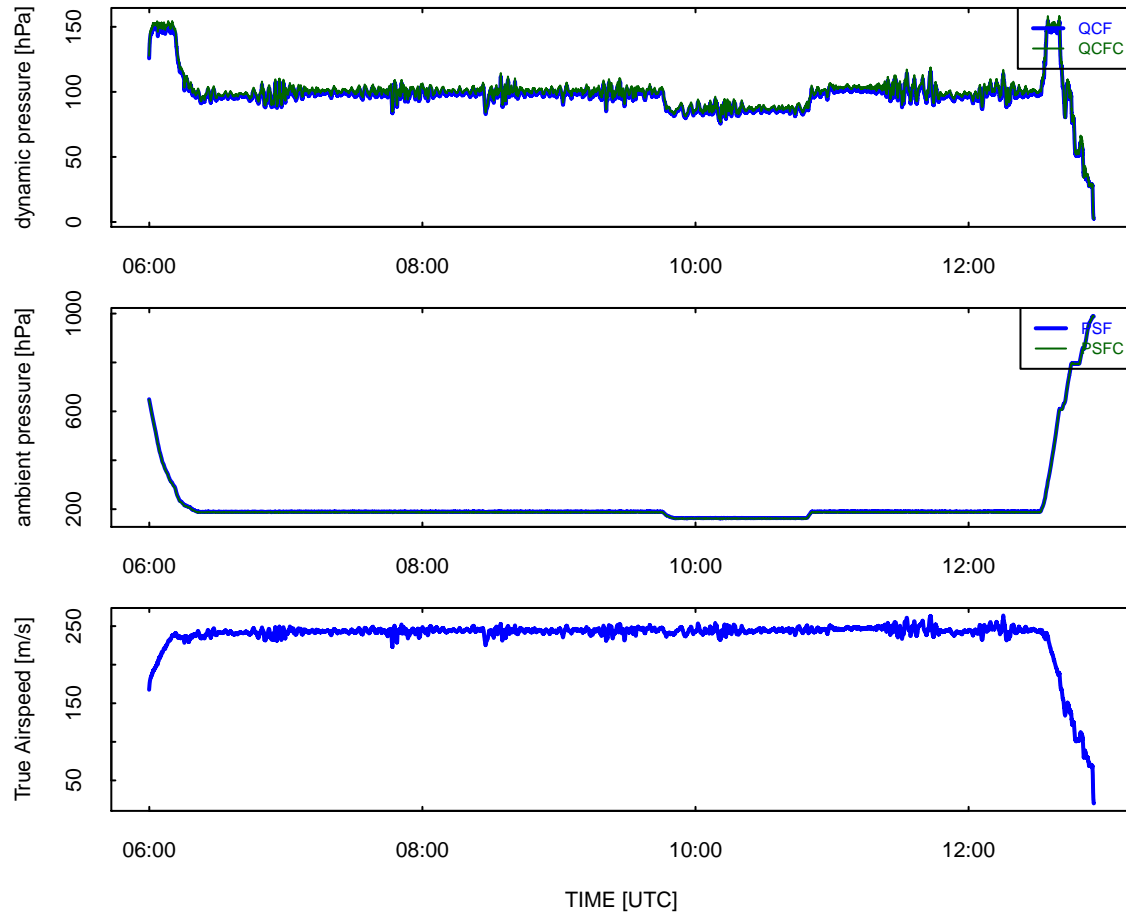


Figure 4: The measurements of dynamic pressure (QCF and, after correction QCFC), ambient pressure (PSF and corrected PSFC) and the resulting true airspeed TASX. Data from DEEP-WAVE flight 16.

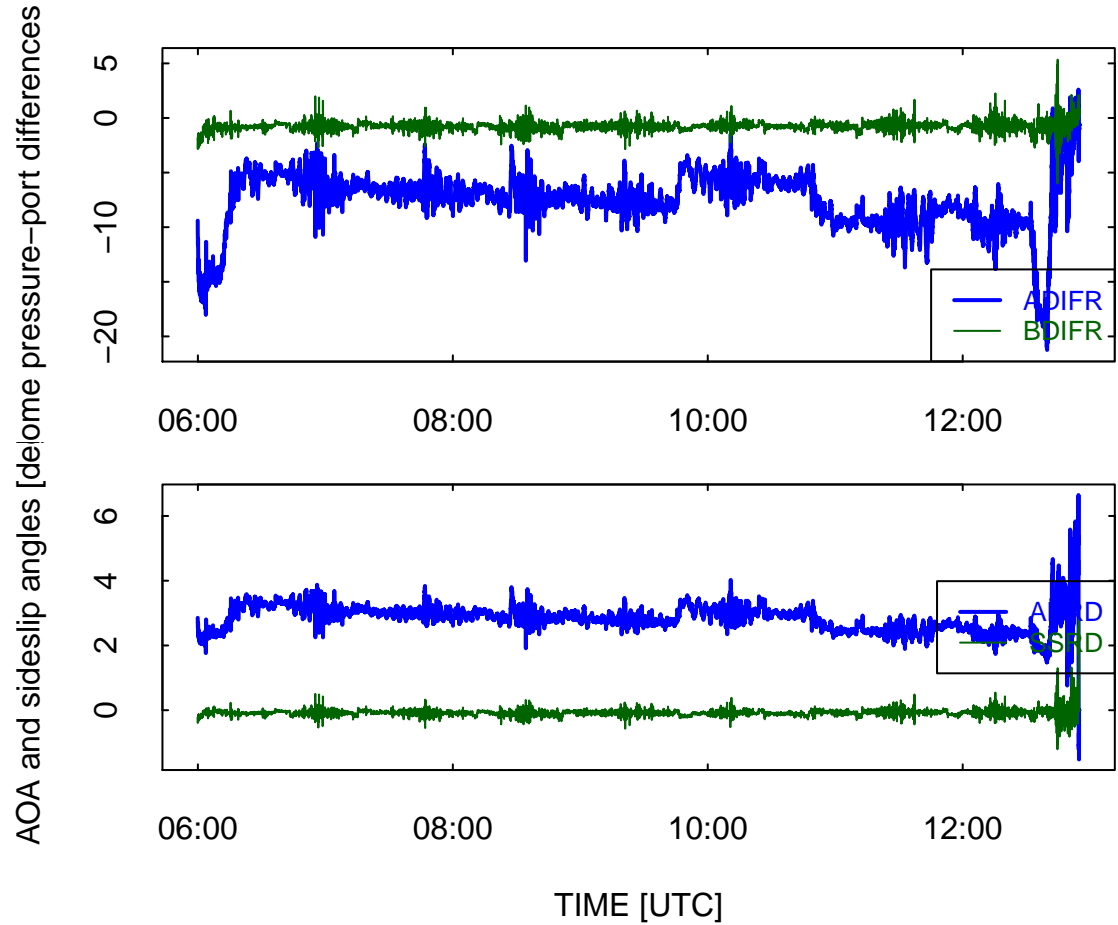


Figure 5: The pressure differences measured on the radome (ADIFR and BDIFR, respectively between the vertically separated ports and the horizontally separated ports) and the resulting airflow angles AKRD (angle of attack) and SSRD (sideslip angle). Data from DEEPWAVE flight 16.

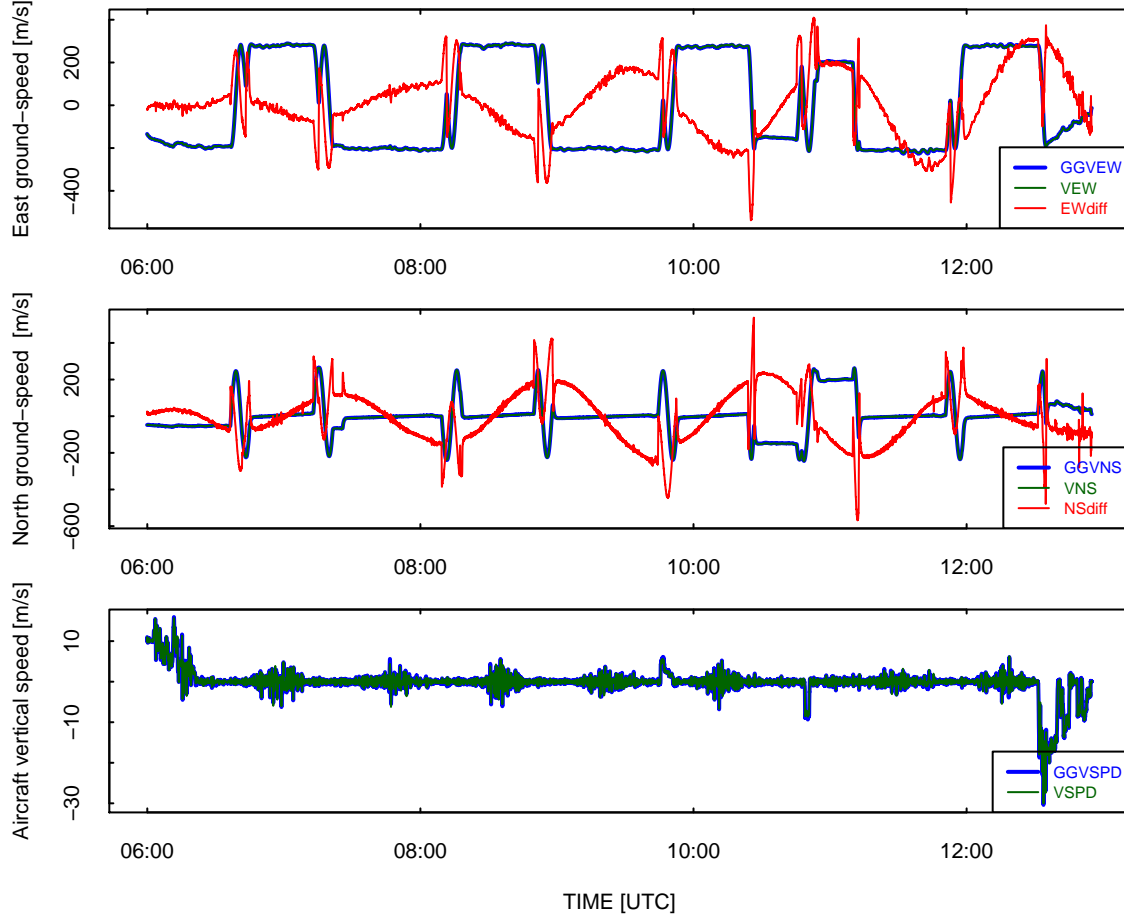


Figure 6: Top two panels: Ground-speed components as measured by the IRU and GPS, and (red lines) the difference between the two measurements multiplied by a factor of 100. Bottom panel: Aircraft vertical speed as measured by the IRU (with built-in damping to the pressure altitude) and by the GPS unit. Data from DEEPWAVE flight 16.

Figure 5 shows the measurements of differential pressure at the radome and the resulting angle-of-attack and sideslip angle calculated from those pressure differences. The calculation is described in Section 4 of this document. Fluctuations in sideslip angle are seldom more than a fraction of a degree, while there can be several-degree fluctuations in the angle-of-attack. The gradual decrease in angle-of-attack is a result of the change in fuel load on the aircraft, which requires a smaller angle-of-attack to keep the aircraft level as the weight becomes smaller.

The last set of components entering the measurement of wind consists of the measurements of the motion of the aircraft with respect to the Earth. These measurements must be combined with the measurement of relative wind to transform the measurements to an Earth-referenced measurement. Figure 6 shows the east and north components of the ground speed as measured by the IRU and GPS. They are close enough to lie almost on top of each other in this plot, but the red lines show the difference magnified by a factor of 100. They clearly show the Schuler oscillation that results from an IRU error in pitch, having magnitude of about $1\text{--}2 \text{ m s}^{-1}$. This

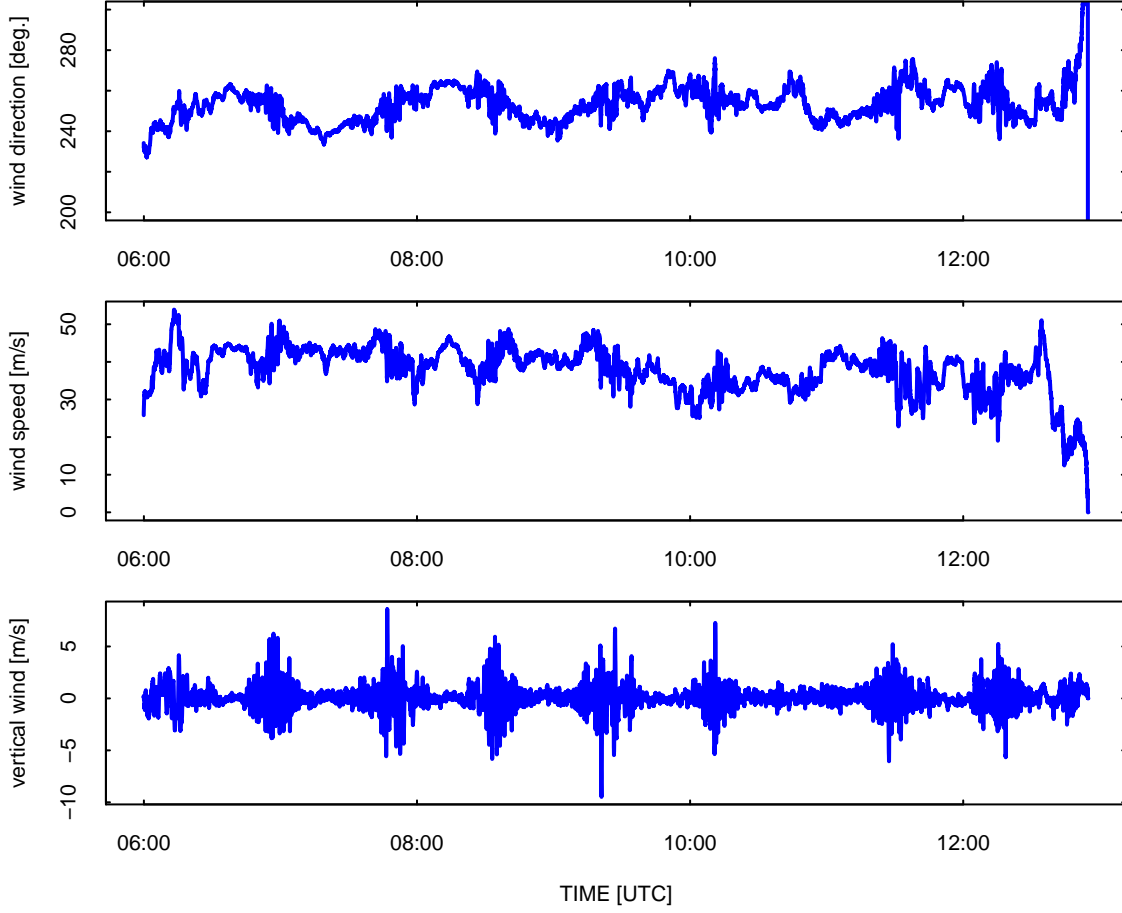


Figure 7: Wind measurements for DEEPWAVE research flight 16.

error is discussed in the next section, and Section 6.2 discusses how the IRU measurements (having good short-term response but long-term drift) and the GPS measurements (having long-term accuracy but inferior short-term response) are combined in the measurement of wind. In addition to the Schuler oscillation, additional perturbations associated with turns result from the mixing of pitch, roll, and heading errors when the aircraft is banked.

Finally, Fig. 7 shows the resulting wind measurements for this flight. These measurements will be discussed extensively in the remainder of this report, and the uncertainty associated with them will be estimated in the closing section.

2.3 The gust-pod system

2.3.1 Overview

The all-weather wind pod was developed by Allen Schanot and is available for mounting under the wing of the GV, where it was installed during the 2014 project DEEPWAVE. It was still

regarded as experimental for this project, and this is the first full documentation of its characteristics. It will be called the gust-pod system here; another name used has been the all-weather wind pod, because the primary reason for its development was to provide a backup wind measurement for cases when the radome system was not available, including times when it was blocked by ice or frozen water in the pressure lines. The gust pod fits into a standard “PMS-style” canister and uses a Rosemount 858 probe, but the location under the wing is one where there is substantial flow distortion in comparison to the free stream so an unconventional calibration is needed to use the measurements. The 858 probe is anti-iced by heaters and should be unaffected by icing or ice accumulation. Five ports are oriented forward, upward and downward 45°, and left and right 45° on the leading edge of the sensor, which has the shape of a hemisphere. There are also ports in a ring around the cylinder behind the hemisphere that provide a static source. The measurements are the pressure difference between the top and bottom ports (ADIF_GP), the pressure difference between the right and left ports (BDIF_GP), and the pressure difference between the forward port and the static ports (QC_GP). In addition, the pressure provided by the ring of static ports is recorded as PS_GP. The system incorporates a Systron-Donner C-MIGITSIII IRU, which is mounted in the pod to be able to measure vibrations and wing-flex motions that will affect the measurements of wind. This unit provides measurements of attitude angles, ground-speed components, and accelerations and uses a GPS signal in a Kalman-filter feedback loop to reduce errors in the measurements. The relevant specifications are listed in Table 2.



Photograph of the Gust Pod (bottom left) and the ports on the Rosemount 858 probe (right).

2.3.2 Attitude angles

The C-MIGITSIII INS/GPS unit provides measurements of the attitude angles, recorded as variables CROLL_GP, CPITCH_GP, and CTHDG_GP. The estimated standard uncertainty in measurement of pitch, 1 mrad (cf. Table 2), is supported by comparison to the cabin-mounted inertial systems; the standard deviation in the difference between the two systems was about $0.1^\circ \approx 1.7$ mrad for extensive multi-flight comparisons, while the expected difference for two systems each having standard uncertainties of 1 mrad would be 1.4 mrad. Some contribution would be expected from vibrations and wing flex that affect the gust pod, so these comparisons are good support for the approximate validity of the specifications. Some of the specifications

Measurement (VARIABLE)	Instrument	Range, Char- acteristics	Standard Uncertainty	Comments
velocity components (CVNS_GP, CVEW_GP, CVSPD_GP)	C-MIGITSIII	with GPS	0.1 m s^{-1}	horizontal and vertical
pitch, roll (CPITCH_GP, CROLL_GP)	C-MIGITSIII	with GPS	$1 \text{ mrad} \simeq 0.06^\circ$	with Kalman filter
heading CTHDG_GP	C-MIGITSIII	with GPS	$1.5 \text{ mrad} \simeq 0.09^\circ$	valid when in motion ^a
pressure differences,858 ports (ADIFR_GP, BDIFR_GP)	Honeywell PPT0001- DXX2VB- S021	$\pm 1 \text{ psi} \simeq \pm 68.95 \text{ hPa}$	0.07 hPa 0.14 hPa max.	the first is “typ.”; same transducers as for radome
dynamic pressure (QC_GP)	Honeywell PPT0005- DXX2VB- S021	$0\text{--}5 \text{ psi}$ $\simeq 0\text{--}345 \text{ hPa}$	0.34 hPa 0.68 hPa max.	“
ambient pressure (PS_GP)	Paroscientific 6000-15A-28	$0\text{--}15 \text{ PSI}$ $\simeq 0\text{--}1035 \text{ hPa}$	0.10 hPa	digital transducer

^aWithout occasional turns the heading error grows linearly at about $1\text{--}10^\circ/\text{hour}$

Table 2: Characteristics of measurements from the gust-pod that are used for the calculation of the wind. There is further discussion of each measurement in the text of Sect. 2.3.

(esp. for heading) degrade in the absence of turns or maneuvers that can be used by the Kalman filter to improve the measurements, as noted in Table 2.

2.3.3 Ambient or static pressure

Ambient pressure (variable PS_GP) is measured by a digital transducer with low uncertainty, as listed in Table 2. However, the Rosemount 858 probe is located under the wing in a location where there is significant airflow distortion, so these measurements often differ from the measurements from the static buttons on the fuselage by 10–20 hPa and significant corrections are needed if these measurements are to be used for pressure measurements. With the gust-pod, the use is as a reference for the differential measurement of dynamic pressure because the dynamic-pressure transducer is connected between the total-pressure port on the front of the 858 probe and the static ports. No calibration has been determined that would make this measurement useful as a measure of true ambient pressure, although that could be done by fitting to match the standard static pressure. In the absence of such a correction, PS_GP should not be considered an alternate measurement of ambient pressure. The use of this measurement to determine an alternate measure of true airspeed will be discussed in Section 4.3.

2.3.4 Dynamic pressure

The dynamic pressure QC_GP is measured by a differential pressure transducer, with characteristics shown in Table 2. The measurement is the pressure difference between the forward-pointing port on the Rosemount 858 probe and the static ports on the side of that probe. Because the system is located under the wing in a region of disturbed airflow, the dynamic pressure requires unconventional correction to obtain the airspeed, as discussed in Sect. 4. This measurement is also used in the calculation of flow angles from the gust-pod pressure ports, as also discussed in that section.

2.3.5 Airflow angles

The difference between pressures at the top and bottom ports of the Rosemount 858 probe (ADIFR_GP) and the corresponding difference between right and left ports (BDIFR_GP) are also measured using differential transducers listed in Table 2. These are analog transducers that produce voltages representing the pressure differences, and those voltages are digitized and recorded by the aircraft data system.

2.3.6 Components of aircraft velocity relative to the Earth

A Systron-Donner C-MIGITSIII INS/GPS, mounted with the gust pod, provides digital representations of the ground-speed components CVEW_GP and CVNS_GP and the vertical speed CVSPD_GP. (cf. Table 2). The unit incorporates a GPS receiver and uses GPS information as input to a Kalman filter for adjustment of these measurements and others discussed in this section.

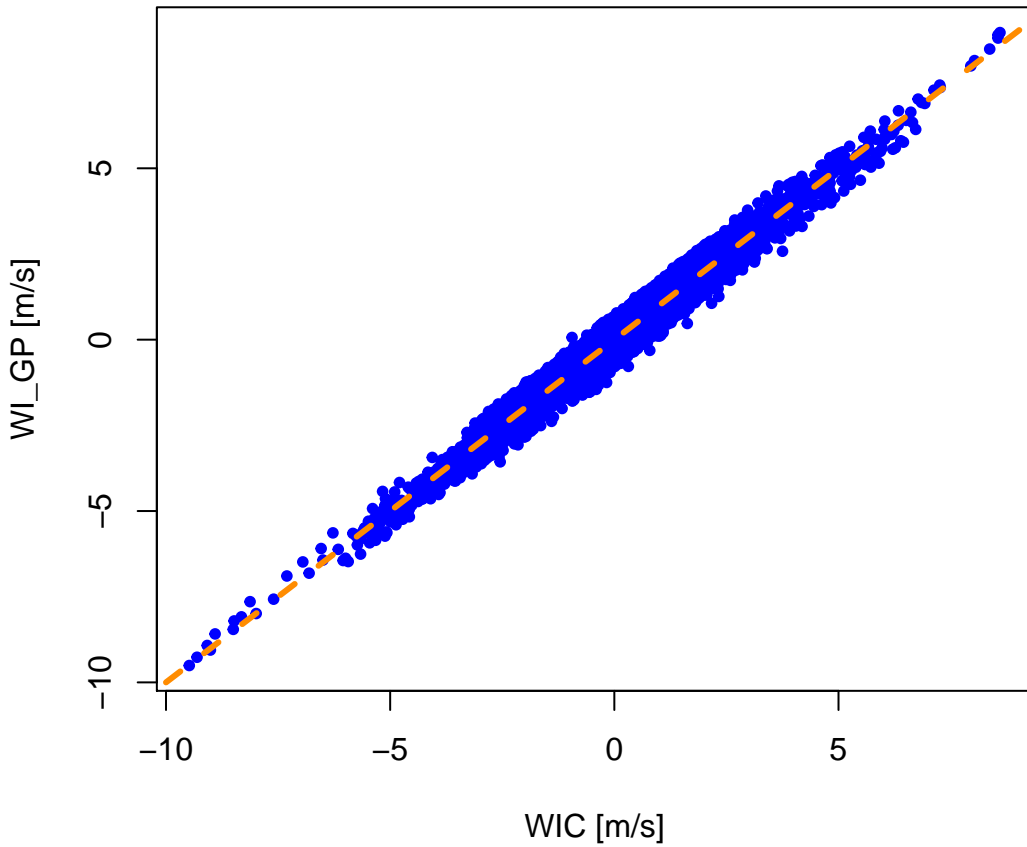


Figure 8: Comparison of vertical wind calculated from the gust pod (WI_GP) to the conventional measurement of vertical wind (WIC). The dashed orange line is a 1:1 reference line, and each blue dot represents a 1-s pair of corresponding measurements.

2.3.7 Temperature

Air temperature is measured in the same way as discussed for the radome system in Sect. 2.2.7, and the same variable (ATX) is used.

2.3.8 Examples of measurements

A preliminary calibration was in use for in-field processing during DEEPWAVE, but it did not perform very well. A new calibration is developed in Section 4. On the basis of that new calibration, it appears that the gust pod provides a useful alternative to wind measurements based on the radome. Plots and average values are presented there to support the validity of this measurement.

The following are some plots that show the results of this processing, in this case from DEEPWAVE flight RF16 on 4 July 2014. Figure 8 shows a comparison of the vertical wind calculated

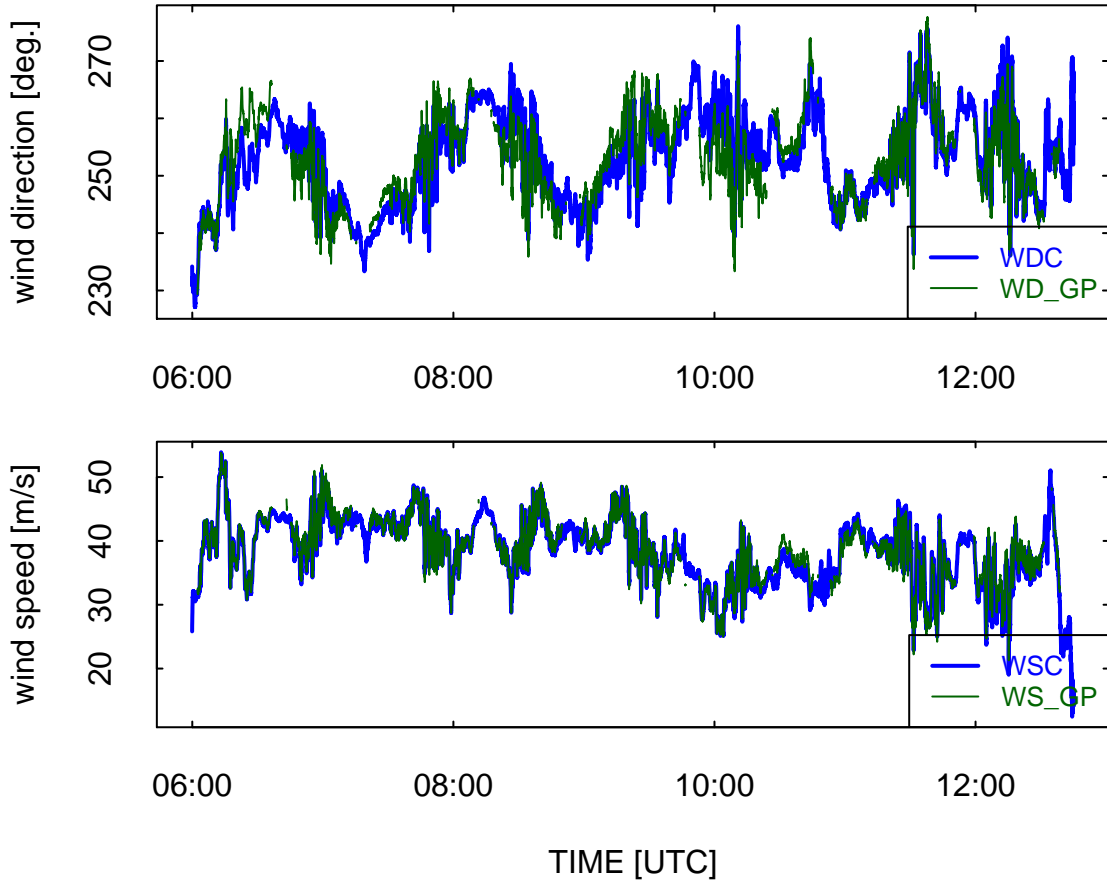


Figure 9: Comparison of horizontal wind direction (top panel) and horizontal wind speed (bottom panel) as determined from the gust pod and from the conventional radome-based system, for measurements where the true airspeed is greater than 130 m/s (to exclude periods of possible flap deployment). Only measurements considered valid are plotted for the gust pod; the restrictions where the gust-pod measurement is flagged as missing and therefore is not plotted here are: altitude (GGALT) > 5000 m, absolute value of roll (ROLL) < 5°. This causes exclusion of some measurements near the start and end of the flight and during turns.

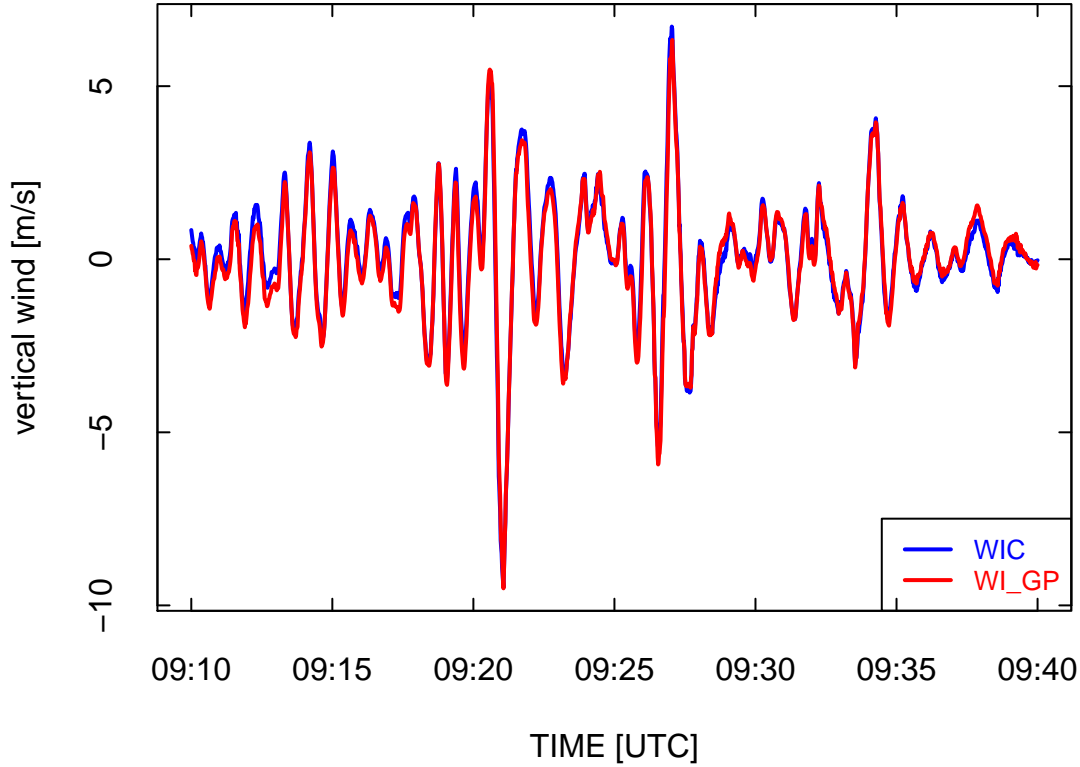


Figure 10: A 30-min segment from flight 16 of the DEEPWAVE project, showing the good agreement of the vertical wind measurements from the gust pod (WI_GP) and from the conventional wind-sensing system on the GV (WIC).

from the gust pod (WI_GP) vs the conventional vertical wind (WIC). The standard deviation between the two measurements is 0.27 m/s. This is a good illustration of performance because this is a flight with large-amplitude waves and some of the largest vertical-wind measurements in the DEEPWAVE project, so the consistency of these measurements even to extremes in this plot indicates that the measurements from the gust pod are useful even for these large-amplitude measurements. Figure 9 shows the corresponding horizontal-wind measurements, and also shows good agreement between the gust pod and the conventional wind-sensing system.³

A small segment of flight from a period with large-amplitude waves is shown in Fig. 10. The two measurements match quite well in regard to the structure of these waves and the amplitudes of the fluctuations. The measurements of horizontal wind speed are in similar agreement, but

³Some spikes would occur in turns if the exclusions listed in the figure caption were not applied to the measurements from the gust pod. These are the result of a problem with the C-MIGITSIII measurement of heading, which exhibits noisy fluctuations as it moves through 180°. These fluctuations introduce large perturbations in the horizontal wind measurements, affecting esp. the east component of the wind.

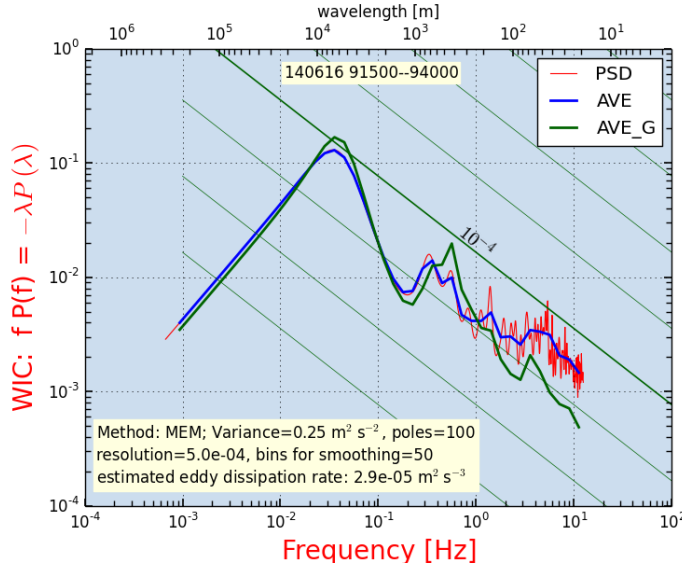


Figure 11: Variance spectra for WIC (red line labeled PSD, unsmoothed, and also shown smoothed as the blue line), compared to the smoothed spectrum for WIG from the gust pod (green line). Data from flight RF05, 9:15:00–9:40:00.

the wind direction for this period shows an offset for the gust pod measurement relative to the conventional measurement, varying from about 5° near the start of this period to about 1° near the end. This is a result of an apparent error in heading from the C-MIGITS IRU, a common feature to see near the start of flights but one that usually was made smaller during flight by the action of the GPS updating via Kalman filter in that unit.

The result of this error in wind direction and the problems with measured heading for flight exactly southbound complicate the use of the measurements of horizontal wind from the gust pod and make them of lesser quality than the standard measurements. Fortunately, in this and most projects, the horizontal-wind measurements are available from the radome-based system on all flights and are usually not compromised even when there is loss of the measurement of angle-of-attack from plugging of the lines in the radome, because the side-mounted ports for the measurement of sideslip seldom are plugged.

Figure 11 shows the high-rate variance spectra from the two systems. There is a significant difference at frequencies above about 3 Hz, with the gust-pod distribution dropping faster and the standard wind WIC showing more variance. The high frequency spectrum from the gust pod may be more realistic; it is unusual to see high variance at these frequencies without a related generating source. The coherence between the radome and gust-pod measurements was above 0.9 for frequencies less than 1 Hz but then fell to around 0.2 at 10 Hz. This is an indication that the two measurements are different in important ways at high frequency. This would not be the case if they were responding with different amplitudes; the signals must really be mostly incoherent at the highest frequency. The separation wing-to-fuselage is about 7 m lateral and 13 m longitudinal, so that doesn't seem enough to cause the low high-frequency coherence. The phase changes from in-phase at frequencies less than 1 Hz to 180° out-of-phase at 9 Hz, with WIG lagging, so this is consistent with the longitudinal offset. Shifting WIG relative to

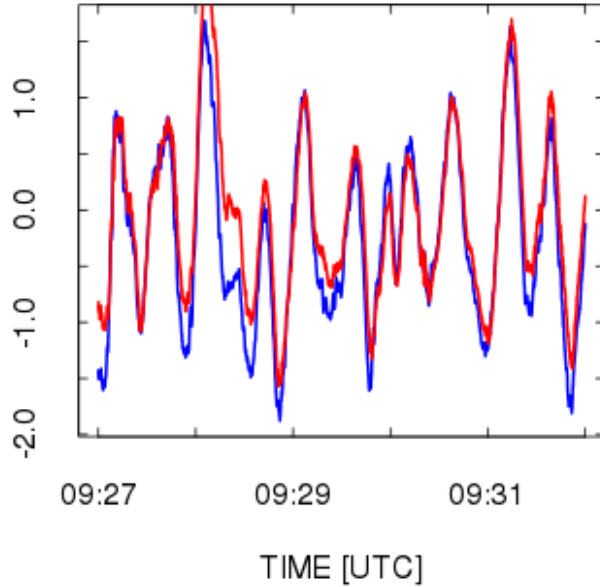


Figure 12: Comparison of WIG (red line) and WIC (blue line) after shifting WIG 1/25 s earlier to compensate for the longitudinal displacement of the sensor.

WIC also gave maximum coherence when WIG was shifted forward 1/25 s. Figure 12 shows an example of the good correspondence between gust-pod and radome measurements of vertical wind after application of such a shift to 25-Hz measurements.

2.3.9 Mixing of Attitude Angles for the Gust Pod

The attitude angles (pitch, roll, heading) as measured by the gust-pod IRU are defined relative to the orientation of the inertial unit in the gust pod, which is aligned a few degrees from the longitudinal axis of the aircraft. The canisters on the GV are oriented with axis pointing inward and downward relative to the aircraft longitudinal axis, in order to align with normal airflow at the pods. This is desirable for hydrometeor sampling and minimum drag, but it complicates the calculation of wind because roll introduced in turns, primarily a rotation about the aircraft longitudinal axis, will appear as a combination of attitude-angle changes in the gust pod. Errors arising from the initial alignment at the start of flights will also cause problems with the measured attitude angles, and it is likely that these will be more significant near the start of flights because the built-in Kalman filter uses GPS measurements to correct such errors in the course of the flight.

This problem with the reference frame for attitude angles has two consequences:

1. Measurements from the gust pod in turns have large errors in comparison to the errors in

level flight. The measurements from the gust pod should probably be flagged as of poor quality whenever the roll exceeds some threshold like perhaps $\pm 5^\circ$. The measurements usually look reasonable in turns despite this worry, but the largest errors occur there.

2. There may be an offset introduced by the mixing of sideslip and angle-of-attack, arising from the difference in roll angle, and this will affect the reference or average value of the measured vertical wind. Some flights (e.g., DEEPWAVE flight 18) have a significant offset in vertical wind from the gust pod at the start of the flight that is related to offsets in heading and roll, gradually corrected in the course of the flight via the C-MIGITSIII Kalman filter.

Because the weight of the aircraft decreases during the flight, so does the angle-of-attack. Because the wing flexes, the measured sideslip at the gust pod also varies with weight of the aircraft. This change in sideslip causes an offset in the mean lateral component of the wind as measured by the gust-pod system.

These effects suggest that the vertical wind measured by the gust pod may have an offset in some cases, particularly at the start of flights, and the sideslip can also have an offset that will contribute to the lateral component of the measured wind. These are weaknesses in the measurements from the gust pod that, at this stage, do not appear easily corrected. A future study implementing Schuler tuning in a post-processing step and correcting for the entwined-angle effects may be able to reduce these weaknesses, but that will require continued analysis not performed for this report. It may also be possible to develop special processing that corrects the measurement of attitude angles in turns, but that has not yet been developed or implemented.

XXX

2.4 The laser air-motion sensor

The laser air-motion sensor (LAMS) is still under development so results presented here will be less extensive than for the other systems. The characteristics and associated uncertainties in measured wind are discussed by Spuler et al. [2011] and Cooper et al. [2014]. Figure 13 shows the one-beam LAMS as installed on the GV, and Fig. 14 shows the configuration of the three or four-beam version.

The system consists of one, three or four fiber-based laser beams focused ahead of the aircraft and a collection system to detect the Doppler shift in light backscattered from aerosols. The transmitter optical components are mounted in an underwing pod, similar to that used for the gust pod, and like the gust pod the system incorporates a compact C-MIGITS inertial reference unit to measure the attitude angles and ground speed of the pod. Early measurements from this system have been used to determine corrections to the pressure measurements, and those serve an important role in reducing uncertainty in the wind measurements, as described in Cooper et al. [2014] and later in this report.

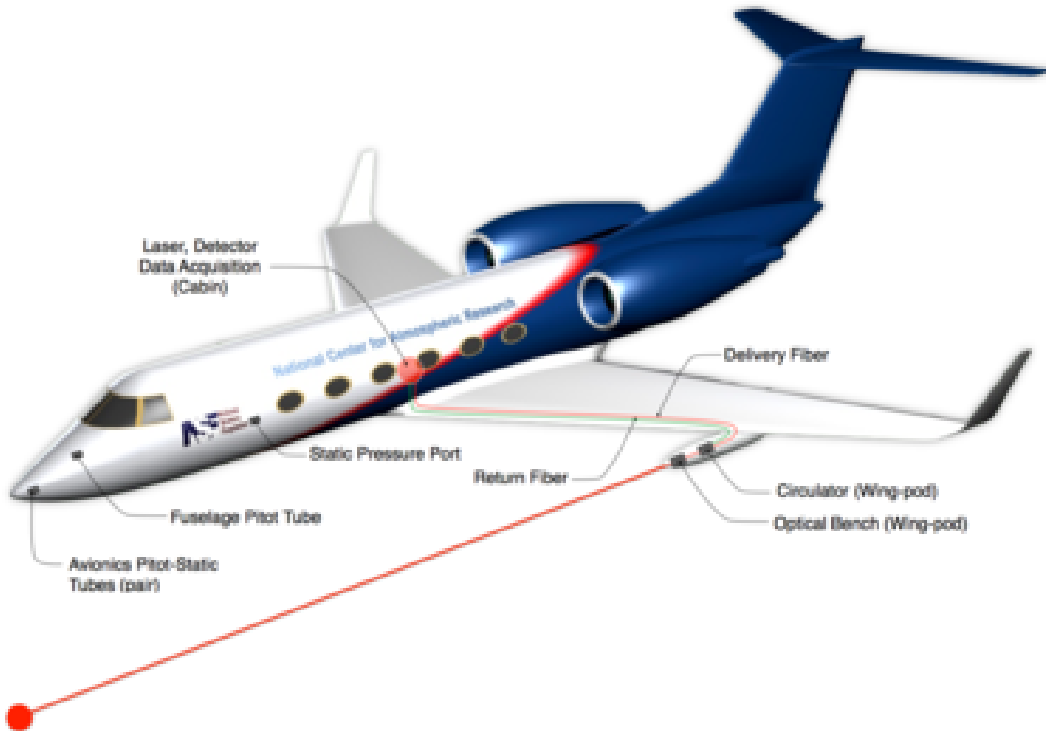


Figure 13: Diagram of the LAMS. Light generated by the laser in the cabin is transmitted by optical fibres to a wing pod, where it is transmitted in a beam that has a focal point well ahead of the aircraft (farther ahead than suggested by this not-to-scale diagram). The light backscattered from aerosol particles in the focal region is collected by the lens, and a circulator mixes a portion of the transmitted signal with the returned signal. The resulting signal, with interference patterns that measure the Doppler shift of the backscattered light, is returned via optical fibre to the cabin for digitization. Also illustrated in this figure are the approximate locations of the static pressure ports and the fuselage pitot tube used by the research data system to measure static and dynamic pressures. This figure appears in Applied Optics in the article by Spuler et al. [2011] and is used here with permission from the Optical Society of America.

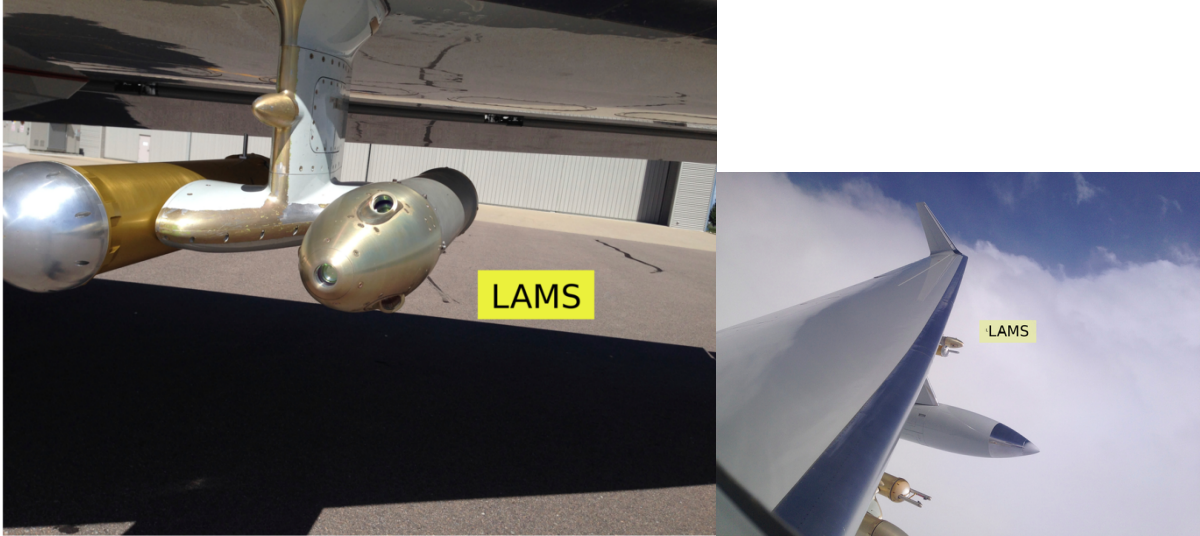


Figure 14: The four-beam configuration of the LAMS optical head as installed in a GV under-wing pod.

LAMS hardware supports up to four beams, with three pointing 35° off the forward direction, with 120° separation about the azimuthal direction. The fourth beam is directed forward from the LAMS unit. The LAMS channel designations changed after DEEPWAVE (summer 2014) when it was decided the instrument would benefit from having a lower noise channel for forward pointing measurements (the laser/detector on channel 4 had lower SNR than the other three channels). Table 2.4 summarizes the labels and pointing angles of each beam for both up to and after DEEPWAVE. Note the number designation refers to the laser, detector, and data processing channels. The letter designation is associated with the exit window on the LAMS head. The pointing angles reported here are ideal. The angle θ is measured relative to the forward direction of the LAMS pod (approximately the angle between the beam and \hat{x}') and the angle ϕ is the rotation angle about \hat{x}' relative to the \hat{z}' axis. This geometry is designed for GV installation where the LAMS pod is installed on the left wing, outboard pylon, outboard position. The pointing geometry relative to the aircraft may change based on the installation configuration on the C-130 (to be determined on ARISTO in fall 2015) where the LAMS optical fiber are routed to the aircraft right wing.

During IDEAS-4-GV, the LAMS beams were focused approximately 15 m from the LAMS exit ports on the pod. After this flight program, concerns were raised about the aircraft causing flow distortion in the LAMS sample volumes, and the beam focus was moved to 20 m from the exit port. In both cases the sample volume is approximately 2 m long.

2.4.1 Relative Beam Pointing

The relative pointing of the LAMS beams is defined by the orientation of each beam relative to the others. If the absolute pointing direction of one beam is known, the relative pointing may be used to determine the absolute pointing of all other beams. We define the relative pointing coordinates such that the z-axis is directed along the forward beam (D). The angle θ_L is the

Beam Name After DEEPWAVE	Beam Name Before/During DEEPWAVE	θ	ϕ
Beam 1/A	Beam 1/A	35°	180°
Beam 4/B	Beam 4/B	35°	60°
Beam 3/C	Beam 3/C	35°	-60°
Beam 2/D	Beam 4/D	0°	-

Table 3: Designations and ideal orientations of LAMS beams for installation on the GV.

angle between the beam and the z-axis and the azimuthal angle ϕ_L is measured relative to the x-axis such that beam 1 (A) is positioned at $\phi_L = 0$.

Two methods were used to determine the relative pointing angles. The first, performed prior to IDEAS-4-GV, used a Laser Survey, in which a commercial laser surveying company measured the positions of the LAMS head and the beam focal points.

The second method used a 30x beam expanded with focusing lens in a fixed position (referred to here as the receiver system) while LAMS was mounted in an astronomical telescope mount. A camera was placed at the focal point of the receiver system and the telescope mount was used to steer the LAMS beams into the receiver system such that each beam was centered on the CCD. This method had redundant pointing measurements, using both C-MIGITS data as well as the telescope mount angle read-outs.

Both methods were relatively accurate, with less than 0.2° difference in beam pointing. It should be noted that the fibers on the LAMS head may have moved slightly between the two measurement methods. The forward pointing beam was added after IDEAS-4-GV which required some disassembly of the LAMS head. So the relatively small difference in beam pointing may be partially attributable to that work.

Prior to IDEAS-4-GV in Sept.–Oct. 2013, a laser survey system was used to estimate the LAMS beam pointing angles of Beams 1, 2, and 3 (the forward pointing beam had not been added at that point). The LAMS head was positioned in the hanger so the bottom two beams were approximately parallel to the floor. Two IR card targets were placed at the focal points of those beams.

The laser survey system locked onto a corner cube reflector and register its position in space. The corner cube was first used to estimate the position of the LAMS exit ports by taking a series of points around their circumference. The tracker then registered the positions of the IR card targets by the same method. Once complete, the LAMS head was rotated by 120° and the process was repeated. This measurement was repeated for three different LAMS head rotations, where two beams were surveyed at a time.

After data was collected, the beam exit and target information were used to provide a best fit for the beam pointing.

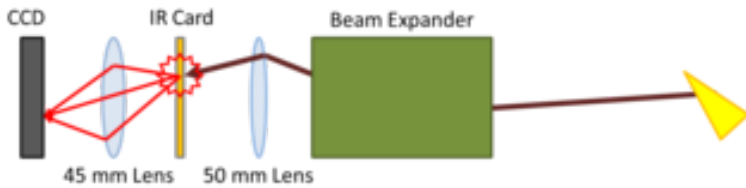


Figure 15: Diagram of the receiver system. The invisible infrared beam enters the beam expander which amplifies the angle of the beam relative to the telescope optic axis, and is then focused onto an IR card. The IR card fluoresces at a visible wavelength and that light is reimaged onto a CCD.

The benefits of this method are

- It measures the beam focal distance.

The weaknesses of this method are

- Only two beams can be surveyed at any one time.
- The measurement process can perturb the beam target.
- There is no reference to the C-MIGITS IRU.
- There is no independent redundant measurement and uncertainty is difficult to quantify.
- The survey can be expensive, requiring the hire of an outside vendor.

The results of the laser survey method were used to process IDEAS-4-GV data, but those angle calibrations have since been traded for the Telescope technique described below.

The relative positions of the LAMS system can be determined by defining a fixed reference vector and directing each beam onto it. The pointing of the LAMS module is recorded when each beam is directed on the reference. Without absolute knowledge of the reference vector, this only allows the relative beam geometry to be determined. Thus, we define a LAMS beam pointing coordinate frame such that the z-axis is along the forward beam.

The telescope beam measurement system was developed in house to provide position insensitive angular measurement. It uses a 30x beam expander consisting of an off axis parabola and convex secondary (exact type is unknown). The light from that beam expander is focused onto an IR card using a 50 mm lens, yielding a total focal length of 1.5 m. The IR card was then reimaged using a 45 mm lens onto a CCD to monitor the beam position (see Figure 15 and 16).

With the IR card at the back focus of the optical system, the beam image is position independent. Its location in this plane is dictated solely by the angle of the input beam. Even though each beam is slightly translated relative to its counterparts, we can still perform accurate angle measurements.



Figure 16: Photographs of the telescope angle measurement system in the RAF optics lab. View of the setup from behind the LAMS pod (top left), the receiver system (bottom left), LAMS mounted in the telescope mount (right).

The LAMS system is mounted in a precision telescope mount with accuracy on the order of $1''$ or about 0.0003° . The mount gives fine resolution in adjusting LAMS pointing into the receiver reference system and provides a digital readout of Alt/Az coordinates. These coordinates provide the first set of pointing data for the LAMS system. The second set of pointing data is provided by the C-MIGITS INS, which is attached and operating during our data collection. Thus, two measurements of the LAMS pointing are provided.

The telescope mount readout provides the quantities Alt, ϑ_T , and Az, φ_T . When a beam is directed into the reference telescope, it is accomplished through rotation operations:

$$\hat{r} = \mathbf{R}(\vartheta_T, \hat{x})\mathbf{R}(\varphi_T, \hat{y})\hat{u}, \quad (6)$$

where \hat{r} is the reference direction of the receiving telescope, \hat{u} is the beam pointing direction and $\mathbf{R}(\theta, \hat{v})$ is a rotation matrix of angle θ about the vector \hat{v} .

To determine the beam pointing angle, we invert the rotation operations (or perform the opposite rotations in the opposite order), which results in

$$\hat{u} = \mathbf{R}(-\varphi_T, \hat{y})\mathbf{R}(-\vartheta_T, \hat{x})\hat{r}. \quad (7)$$

To obtain a beam pointing vector, we first need to know the reference vector in some coordinate basis. We let Beam 4 (the forward pointing beam) define the z-axis in this coordinate basis and obtain \hat{r} by evaluating Eq. (6) for the recorded Alt/Az angles of Beam 4 (D) where $\hat{u} = [0 \ 0 \ 1]^T$. We then obtain all other beam vectors from their respective Alt/Az coordinates using Eq. (7).

The process for obtaining the beam pointing vectors from C-MIGITS is essentially identical to the process above, except that C-MIGITS provides roll, pitch and heading. It should be noted, as will be addressed later, the C-MIGITS heading is not reliable when the device is stationary.

Beam	Angle difference between C-MIGITS and Telescope Mount
Beam 1 (A) (Upward)	0.024°
Beam 2 (B) (Down-In)	0.004°
Beam 3 (C) (Down-Out)	0.003°
Beam 4 (D) (Forward)	0.024°

After the pointing angles of the beams are obtained from the telescope mount and C-MIGITS, the pointing angles need to be compared. However, the beam vectors are recorded in different coordinate frames and C-MIGITS heading data cannot be treated as reliable. A transformation matrix between these two frames and heading adjustments to C-MIGITS are determined using minimization of errors so we can compare the beam pointing results. Table 2.4.1 shows the difference in angle between each of the four beams after optimizing the transformation between the two coordinate frames. The two beam pointing measurements give results that are quite close.

An assessment of the beam pointing accuracy was performed by translating the focused beam across the IR card and finding the spread of angles accepted by the optical system. The full angle field-of-view of the system was approximately $2'$ or about 0.02° . The beam spot position can be repeated to greater accuracy than this (we can see when it is well centered using the CCD), however this is probably a reasonable uncertainty figure because the IR card may not be located at the exact Fourier plane of the optical system.

Beam	θ_L Telescope	θ_L C-MIGITS	θ_L Laser Survey	ϕ_L Telescope	ϕ_L C-MIGITS	ϕ_L Laser Survey
Beam 1 (A) (Upward)	35.03°	35.08°	34.95°	— ^a	—	—
Beam 2 (B) (Down-In)	34.86°	34.85°	34.96°	119.74°	119.74°	120.01°
Beam 3 (C) (Down-Out)	34.86°	34.85°	35.01°	120.16°	120.16°	120.00°

^aBeam 1 is used as the basis for $\phi = 0$ in the relative pointing coordinate frame

The benefits of the telescope beam measurement method are:

- All four beams are measured without changes to the setup.
- The measurement is "hands off", so there is very little risk of perturbing the system during the measurement processes.
- The processes provides redundant angle measurements (C-MIGITS INS and the telescope mount).
- The entire LAMS pod is used and referenced directly to the same C-MIGITS INS used in flight.

The weaknesses of this method are:

- Beam focal positions are not measured.
- Setup and alignment of the system is time consuming (approximately 2 days).
- The procedure still does not provide an absolute pointing measurement because the telescope acceptance vector is not known.

The following uncertainty analysis treats unknown biases in pointing as random variables with standard deviations or variances. These figures represent uncertainty, not stochastic processes. The resultant variances provide bounds on the LAMS wind vector accuracy based strictly on the instrument characterization, independent of other factors such as signal fidelity.

The accuracy to which we know the LAMS relative beam pointing directly impacts our estimates of airspeed and wind. A sequence of line-of-sight velocity measurements are given by the equation:

$$\vec{m} = \mathbf{U} \vec{v}_L, \quad (8)$$

where \vec{m} is the set of measurements (3 or 4 elements corresponding to the number of beams in use), \vec{v}_L is the air velocity vector in the LAMS beam coordinate basis and \mathbf{U} is the matrix describing each beam's pointing angle given by

$$\mathbf{U} = [\hat{u}_1 \quad \hat{u}_2 \quad \hat{u}_3 \quad \hat{u}_4]^T, \quad (9)$$

where \hat{u}_i is the i th beam pointing direction. The exact vector entries for \mathbf{U} are dependent on which beams are used for LAMS operation. For example, \hat{u}_4 would not be included for HCR-TEST (post-DEEPWAVE configuration) where the down-inboard beam was not used in that three beam configuration. For this analysis the beam and air velocity vectors are defined in the LAMS relative coordinate frame. Though this is not inherently required, it allows the analysis presented in this section to flow directly into further uncertainty analysis described in Section 2.4.2.

The covariance matrix of a beam pointing vector is given by

$$\Sigma_{\hat{u}_i}^2 = \left(\frac{\partial \hat{u}_i}{\partial \phi} \right) \sigma_\phi^2 \left(\frac{\partial \hat{u}_i}{\partial \phi} \right)^T + \left(\frac{\partial \hat{u}_i}{\partial \theta} \right) \sigma_\theta^2 \left(\frac{\partial \hat{u}_i}{\partial \theta} \right)^T, \quad (10)$$

where σ_ϕ and σ_θ are the standard deviation of the beam pointing angles. Note that the uncertainty in these angles may be different for each beam, but this analysis will treat them as identical.

The variance in a measurement due to beam pointing uncertainty is given by

$$\sigma_{m_{ii}}^2 = \vec{v}_L^T \Sigma_{\hat{u}_i}^2 \vec{v}_L. \quad (11)$$

The uncertainty in the relative pointing angles are assumed to be independent for each beam (common uncertainty in the instrument pointing will be addressed in section 2.4.2). Thus the total measurement covariance matrix is diagonal and given by

$$\Sigma_{\vec{m}}^2 = \begin{bmatrix} \sigma_{m_{11}}^2 & 0 & 0 & 0 \\ 0 & \sigma_{m_{22}}^2 & 0 & 0 \\ 0 & 0 & \sigma_{m_{33}}^2 & 0 \\ 0 & 0 & 0 & \sigma_{m_{44}}^2 \end{bmatrix}. \quad (12)$$

The total velocity uncertainty in the LAMS coordinate frame is ultimately bounded by its covariance matrix

$$\Sigma_{\vec{v}_L}^2 = \mathbf{U}_{inv} (\Sigma_{\vec{m}}^2 + \Sigma_f^2 + \mathbf{U} \Sigma_{\vec{v}}^2 \mathbf{U}^T) \mathbf{U}_{inv}, \quad (13)$$

where the velocity uncertainty resulting from beam pointing uncertainty is given by the covariance matrix $\Sigma_{\vec{m}}^2$ from Eq. (12), the uncertainty due to FFT Doppler peak estimation is described by the covariance matrix Σ_f^2 and is defined in section 2.4.3, the covariance matrix $\Sigma_{\vec{v}}^2$ is the result of velocity variability between the three or four beam sample volumes with \mathbf{U} being the beam projection matrix from Eq. (9) and \mathbf{U}_{inv} is the inversion matrix for finding the total velocity vector from the three or four line-of-sight measurements. In the case of the three beam LAMS, $\mathbf{U}_{inv} = \mathbf{U}^{-1}$. However, because the four beam system is overdefined, a pseudo-inverse may be used, or if the uncertainty in measurements are well known,

$$\mathbf{U}_{inv} = \left[\mathbf{U}^T (\Sigma_L^2)^{-1} \mathbf{U} \right]^{-1} \mathbf{U}^T (\Sigma_L^2)^{-1}, \quad (14)$$

where

$$\Sigma_L^2 = \Sigma_{\vec{m}}^2 + \Sigma_f^2 + \mathbf{U} \Sigma_{\vec{v}}^2 \mathbf{U}^T. \quad (15)$$

Assuming the angle uncertainty of all four beams is approximately 0.02° and an aircraft velocity of 200 m/s along the LAMS pointing direction, the total velocity uncertainty resulting from beam pointing uncertainty is approximately 0.06 m/s in the horizontal and vertical directions with the four beam configuration, 0.09 m/s in the horizontal and vertical directions with the three beam configuration used in HCR-TEST. To first order approximation, The forward velocity is insensitive to small perturbations beam pointing.

Add note that C-MIGITS cannot provide reliable heading information without moving. Heading adjustments had to be added to the fit of the two measurements.

2.4.2 C-MIGITS/Absolute Beam Pointing

With the relative pointing angles of the beams, an air velocity vector can be retrieved reliably in the predefined LAMS coordinate frame. However, the exact transformation between the LAMS beams and the C-MIGITS coordinate frame (defined by the unit's principle axes) is unknown. We typically assume that one C-MIGITS axis is exactly aligned to the forward pointing beam and one is directed along the angle beam 1. However, it stands to reason that there will be some slight differences between the LAMS beam coordinate frame and the principle axes of the C-MIGITS. At present, the only method we have for determining this transformation relies on making small angle adjustments based on flight maneuvers.

Let the transformation matrix between the LAMS relative coordinate frame and the C-MIGITS principle axes be \mathbf{T}_L . The velocity from LAMS is converted to the C-MIGITS coordinate frame using

$$\vec{v}_c = \mathbf{T}_L \vec{v}_L, \quad (16)$$

where \vec{v}_c is the air velocity vector in the C-MIGITS coordinate frame and \vec{v}_L the air velocity vector in the LAMS relative beam coordinate frame. To propagate error in the transformation matrix we reframe the problem by vectorizing the matrix such that Eq. (16) becomes

$$\vec{v}_c = \mathbf{V}_L \vec{t}_L, \quad (17)$$

where the matrix \mathbf{T}_L has been converted to the vector \vec{t}_L given by

$$\vec{t}_L = [T_{11} \ T_{12} \ \cdots \ T_{33}]^T, \quad (18)$$

where T_{ij} is the element of \mathbf{T}_L from the i th row and j th column. The matrix \mathbf{V}_L is constructed from the LAMS coordinate frame velocity vector \vec{v}_L and is given by

$$\mathbf{V}_L = \begin{bmatrix} v_1 & v_2 & v_3 & 0 & 0 & 0 & 0 & 0 & 0 \\ 0 & 0 & 0 & v_1 & v_2 & v_3 & 0 & 0 & 0 \\ 0 & 0 & 0 & 0 & 0 & 0 & v_1 & v_2 & v_3 \end{bmatrix}, \quad (19)$$

where v_i is the i th element of \vec{v}_L .

The covariance matrix of \vec{t}_L can be estimated from the uncertainties in the roll, pitch and yaw transformation angles denoted here as γ , β and α respectively using partial derivatives

$$\Sigma_{\vec{t}_L}^2 = \left(\frac{\partial \vec{t}_L}{\partial \gamma} \right) \sigma_\gamma^2 \left(\frac{\partial \vec{t}_L}{\partial \gamma} \right)^T + \left(\frac{\partial \vec{t}_L}{\partial \beta} \right) \sigma_\beta^2 \left(\frac{\partial \vec{t}_L}{\partial \beta} \right)^T + \left(\frac{\partial \vec{t}_L}{\partial \alpha} \right) \sigma_\alpha^2 \left(\frac{\partial \vec{t}_L}{\partial \alpha} \right)^T. \quad (20)$$

Thus the velocity covariance matrix in the C-MIGITS coordinate frame is given by

$$\Sigma_{\vec{v}_c}^2 = \mathbf{V}_L \Sigma_{\vec{v}_L}^2 \mathbf{V}_L^T + \mathbf{T}_L \Sigma_{\vec{v}_L}^2 \mathbf{T}_L^T, \quad (21)$$

where $\Sigma_{\vec{v}_L}$ is obtained from Eq. (13).

It should be noted that a similar analysis can be performed for the transformation between C-MIGITS and a Global or aircraft coordinate frame where uncertainties in C-MIGITS roll, pitch and heading are better known.

ADD DETAILS ON DETERMINING THIS TRANSFORMATION MATRIX FROM FLIGHT DATA.

With the C-MIGITS INS, the air velocity measurements can be transformed into a global coordinate frame. The transformation matrix is determined using \mathbf{T}_1 , \mathbf{T}_2 and \mathbf{T}_3 from the roll, pitch and yaw reported by C-MIGITS. The analysis needed for this step is covered in Section 2.1.3.

2.4.3 Frequency Precision

The LAMS A/D samples each beam detection channel at 200 MHz and performs a 1024 point FFT. The frequency resolution of the FFT is thus given by the sample rate divided by the number of data points

$$\Delta f = \frac{f_s}{N_s} = 195\text{kHz}. \quad (22)$$

The Doppler shift measured on a particular beam is

$$f_D = \frac{2}{\lambda} \hat{u} \cdot \vec{v}, \quad (23)$$

where λ is the laser wavelength (1560 nm), \hat{u} is the beam direction and \vec{v} is the velocity vector of the air relative to the instrument. A factor of two is included because the Doppler shift is imposed twice, first when the beam is absorbed by the aerosol and second when it is re-emitted. Along the beam line-of-sight, each FFT bin corresponds to a velocity resolution of $\Delta v_{LOS} = 0.15\text{m/s}$. With post processing the backscatter Doppler peak can be determined at sub-bin resolution. This is accomplished using linear interpolation on the derivative of the backscatter peak to find the derivative zero crossing. For the purposes of this analysis, we assume a sub-sample resolution of about 0.3, giving a line-of-sight velocity resolution of about $\Delta v_{LOS} = 0.05\text{m/s}$.

The resulting covariance matrix for each line-of-sight velocity measurement (only accounting for frequency accuracy) is diagonal with identically distributed variances

$$\Sigma_f^2 = \begin{bmatrix} \sigma_{v_{LOS}}^2 & 0 & 0 & 0 \\ 0 & \sigma_{v_{LOS}}^2 & 0 & 0 \\ 0 & 0 & \sigma_{v_{LOS}}^2 & 0 \\ 0 & 0 & 0 & \sigma_{v_{LOS}}^2 \end{bmatrix}, \quad (24)$$

where, for our purposes, we assume $\sigma_{v_{LOS}} = \Delta v_{LOS}$.

The analysis presented here assumes variance in the sample rate to be small compared to other error sources.

Note that at GV speeds, the Doppler shift is expected to exceed the Nyquist frequency at the present sample rate. We use the true air speed measurements from the aircraft radome to determine which frequency fold contains the Doppler peak.

2.4.4 Flow Distortion

Initial operation of the three beam LAMS on IDEAS-4-GV revealed that the aircraft can influence flow fields in the LAMS sample volume. This issue became recognizable when data processing showed the down-inboard beam registered significantly slower velocities than the other two beams. An analysis using Gulfstream's computational fluid dynamics analysis confirmed that all three beams could be expected to observe some flow distortion. The expected flow distortion depends on the aircraft flight parameters. The down-inboard beam is expected to experience the largest effect, typically observing a line-of-sight flow effect between -0.5 and -2.0 m/s when the beam is focused at 20 m. The upward beam may see flow effects on the order of ± 0.5 m/s and the down-outboard may see flow effects between 0 and -0.5 m/s.

On the GV, LAMS no longer uses the down-inboard beam due to the substantial flow effects in its sample volume. The flow effects around the C-130 will be better determined after the ARISTO flight campaign in Fall 2015.

2.4.5 Uncertainty arising from separation of measurement volumes

In turbulent conditions the three sensitive volumes can be characterized by slightly different values of the wind vector $\mathbf{v} = \{u, v, w\}$. The single forward beam measures u directly while the 3-beam system must solve for u using the relative wind measurements at three locations displaced from each other. If there are variations in the wind vector at these three locations, that will introduce an error that can be significantly larger than the measurement errors for a single-beam-forward system.

If for simplicity it is assumed that the 3-beam system is aligned so that the longitudinal axis matches the u axis and the vertical axis matches the w axis, then the unique solution (for a 35° diverging-beam angle) for the true airspeed (u) is

$$u = \frac{(a_1 + a_2 + a_3)}{3 \cos(35^\circ)} \quad (25)$$

where a_i is the relative airspeed measured by the i th beam. If each beam measures relative airspeed in its direction of alignment to an uncertainty δ , then a one-beam system aligned along the airflow measures with uncertainty δ while a three-beam system measures to uncertainty $\sqrt{3}\delta/(3 \cos(35^\circ)) = 0.7\delta$, so if each beam is an independent measurement the 3-beam system measures TAS more accurately than a single-beam system. However, the unique solution for the wind vector obtained from the 3-beam system relies on the assumption that all three beams are viewing air that has the same wind vector \mathbf{v} . If there is variation in the wind vector at the three

viewed locations, that variation is not necessarily just variation in u (that it might be desirable to average) but can also result from other variations because the beams are not aligned along the u axis.

Because the uncertainty δ is less than 0.1 m/s, variations of this magnitude would introduce errors comparable to the measurement error. The spatial separation between any two sensitive volumes in the 3-beam system is about $1.5(\sqrt{2}L\sin(35^\circ)) \approx 18$ m for focal distance $L=15$ m. The variance in the wind for points separated by 18 m can be estimated as follows:

$$(u')^2 = \int_{k_0}^{\infty} \alpha \varepsilon^{2/3} k^{-5/3} dk = \alpha \varepsilon^{2/3} \frac{3}{2} k_0^{-2/3} \quad (26)$$

where $k_0 = 2\pi/\Delta$ with $\Delta = 18$ m. For modest eddy dissipation rates in the range $\varepsilon = 0.001$ to $0.01 \text{ m}^2\text{s}^{-3}$, and for $\alpha = 2/3$ (FIND REFERENCE XXX), (26) results in estimates of the velocity variance of about $.02\text{--}0.1 \text{ m}^2\text{s}^{-2}$, or standard deviations of about 0.14 to 0.3 m/s. These fluctuations, entering (25), will cause errors in the estimate of u that are not negligible in comparison to the measurement errors in $\{a_1, a_2, a_3\}$.

3 Uncertainty components and summary

3.1 General structure of an analysis of uncertainty

Here we follow a particular style for construction of an analysis of uncertainty by including these components:

1. A description of the measuring system. Section 2 of this report serves this function by providing extensive discussion of each component contributing to the measurement of wind, and it discusses what is known about specifications for uncertainty associated with those components. It also includes description of the algorithm leading to components of the measured wind, and it discusses the three independent systems available for measuring wind on the GV.
2. Tests and calibrations. Section 4 provides key information on how calibration maneuvers are used to determine the sensitivity of some of the measurements to components of the wind. This section on calibration is key to the uncertainty analysis because to a large extent many of the potential errors from sensors are removed by this calibration, and the calibration becomes the central factor affecting the final uncertainty. Other intermediate sections discuss some specific tests applied to the measurements in order to check or reduce the uncertainty limits associated with these measurements. These sections (3, 5, and 6) go somewhat beyond a conventional analysis of uncertainty in that there are some new developments discussed there and some unconventional ways of checking the measurements.
3. Discussion of the elemental contributions to uncertainty. This discussion will follow in this section, but first it appears useful to provide a more general although incomplete discussion of what is expected from that detailed analysis. The standard tabulation of elemental sources of uncertainty then follows in subsections 3.3 and 3.4.
4. Summary and comprehensive estimate of uncertainty. This follows at the end of this section and presents the key conclusions of this study.

Because three wind-measuring systems are characterized in this report, they will be discussed separately. However, the standard system is the radome-based system, so that will be treated in the most depth. The other two systems, the under-wing gust pod and the LAMS, are new systems and their characteristics are still being developed and explored, so their discussion necessarily will be incomplete until additional flight data are collected.

3.2 Preliminary estimates of uncertainty

Vertical wind. Because the calculation of wind from the contributing measurements involves coordinate transformations, evaluation of the uncertainty in wind components involves difficult error propagation through the transformation matrices and other equations of Sect. 2.1. For

application to straight-and-level flight (or flight where the intent is to remain level), simplified equations suffice for evaluation of the error terms, but it will also be useful to employ Monte-Carlo simulations to be sure that error contributions are propagated correctly.

For the vertical wind, Eq. 44 provides an approximate relationship that leads to straightforward error propagation, esp. if it is assumed that the angle of attack α and pitch θ are small angles so that

$$w = V(\alpha - \theta) + w_p \quad (27)$$

and errors in w (δw) can be related to the errors in the basic measurements (δV , $\delta \alpha$, $\delta \theta$, δw_p) by differentiating Eq. 27:

$$\delta w = (\alpha - \theta)\delta V + V(\delta \alpha - \delta \theta) + \delta w_p . \quad (28)$$

Correlations among these error terms are possible, so a full evaluation that does not assume independence among the errors leads to:

$$\begin{aligned} \langle (\delta w)^2 \rangle &= (\alpha - \theta)^2 \langle (\delta V)^2 \rangle + V^2 (\langle (\delta \alpha)^2 \rangle + \langle (\delta \theta)^2 \rangle) + \langle (\delta w_p)^2 \rangle \\ &\quad + 2 ((\alpha - \theta) (V(\langle \delta V \delta \alpha \rangle - \langle \delta V \delta \theta \rangle) + \langle \delta V \delta w_p \rangle)) \\ &\quad + 2V (\langle \delta \alpha \delta w_p \rangle + \langle \delta \theta \delta w_p \rangle) - 2V^2 \langle \delta \alpha \delta \theta \rangle \end{aligned} \quad (29)$$

The approximate magnitudes of these terms, discussed in detail below, are: $\delta V = 0.1$ m/s, $\delta \alpha = 0.1^\circ \simeq 2$ mrad, $\delta \theta \simeq 1$ mrad, and $\delta w_p = 0.03$ m/s. Other typical magnitudes are $V \simeq 200$ m/s, $\alpha \simeq \theta \simeq 2^\circ \simeq 3.5$ mrad. For these typical magnitudes, the only terms in Eq. 29 that make potentially significant contributions are:

$$\langle (\delta w)^2 \rangle = V^2 (\langle (\delta \alpha)^2 \rangle - 2 \langle \delta \alpha \delta \theta \rangle + \langle (\delta \theta)^2 \rangle) \quad (30)$$

The error in pitch arises from measurements from the IRU and is affected mostly by an initial offset during alignment and then further changes in this error arising from the Schuler oscillation and from accelerations that affect this error. The error in angle-of-attack, on the other hand, arises from a combination of measurement error from the pressure transducers and error in the formula used to deduce angle-of-attack from the pressure measurements. This error is not independent of the error in pitch, however, because the calibration as presented in Section 4.1 relies on the measured difference between pitch and angle of attack being zero when the vertical wind and vertical aircraft motion are zero. Thus any bias in pitch is transferred to a bias in angle of attack, so this component of the error in (30) should cancel. The remaining errors arise from sources that are independent and likely uncorrelated, so the middle term on the right side of (30) will be neglected in this preliminary analysis.

It is possible to estimate the magnitudes of these errors from measurements. Because the GV instrumentation includes two identical inertial systems, the difference in measurements of pitch

from those two systems provides one lower-bound estimate of the uncertainty in pitch. Measurements discussed in Sect. 2.2.2 suggest that, for periods when the roll of the aircraft was within 5° of zero, the difference between these redundant measurements was about 0.3 mrad or less than about 0.02° . Section ?? presents additional evidence from evaluation of the Schuler coupling between pitch or roll errors and ground-speed errors, also indicating that typical pitch errors are of about this magnitude. This is significantly smaller than the manufacturer's specified uncertainty for this instrument, $\pm 0.05^\circ$.

This uncertainty in pitch is comparable to the estimated random uncertainty in angle-of-attack, for which the variance spectra discussed in Sect. 5.2.2 suggest a random error of about $0.02^\circ \simeq 0.35$ mrad.⁴ The estimated uncertainties in angle-of-attack and pitch are thus comparable, and both influence the uncertainty in vertical wind.

The rough-estimate uncertainty in vertical wind (to be refined later) is then, for flight at about 230 m/s, about $230\sqrt{0.0003^2 + 0.00035^2} \simeq 0.1$ m/s. Other factors, esp. the radome calibration, need to be considered for a refined estimate, as presented in Section 3.3.

Horizontal wind Errors in measurements affect the longitudinal and lateral components of the horizontal wind in different ways. For the longitudinal component (along the aircraft longitudinal axis), the relative-wind measurement (essentially the true airspeed) has been calibrated by comparison to measurements of the single-beam LAMS, leading to an estimated standard uncertainty of about 0.1 m/s (Cooper et al., 2014). The LAMS measurement is based on measurement of the Doppler shift and thus has low limits for bias and precision, dependent primarily on the uncertainty associated with determining the peak in the returned Doppler spectrum in the presence of turbulence. The lateral component is measured using the sideslip angle, which is determined in a manner similar to that used to calibrate the measurement of angle-of-attack. However, the zero reference angle for attack is determined well by assuming that, on average in quiescent air, the vertical wind should be zero. No similar reference angle exists for sideslip, and trim adjustments to the aircraft can change the mean sideslip angle, so a different procedure with additional sources of uncertainty must be used.

Two maneuvers are particularly effective for determining the zero reference for sideslip (at which angle the lateral horizontal component of the relative wind would be zero): (i) Reverse-heading maneuvers, where a straight leg is flown for a short time (typically 2 min), then the aircraft reverses heading and flies back along the reverse heading, with the result that the wind component perpendicular to the longitudinal axis of the aircraft should reverse sign; or (ii) constant-bank circles flown drifting with the wind, for which the lateral component of the wind should exhibit a sinusoidal variation around the circle reflecting a possible heading and/or sideslip error. Both maneuvers can provide a reference for correcting a combination of heading and sideslip errors, and the circle maneuver provides a mechanism for determining the sideslip error alone, as discussed in Sect. 6.1. There the uncertainty associated with the bias in sideslip was indicated to be about 0.06° and the random uncertainty in heading was estimated to be less than 0.09° , with a bias limit comparable to that in sideslip.

⁴DEEPWAVE flight 15, 3:40–3:55, spectrum for AKRD, compared to simulated spectrum with random-noise amplitude of 0.07. As generated, this has mean of half the amplitude, so it corresponds to a standard deviation of $0.07/\sqrt{12} \simeq 0.02^\circ \simeq 0.35$ mrad.

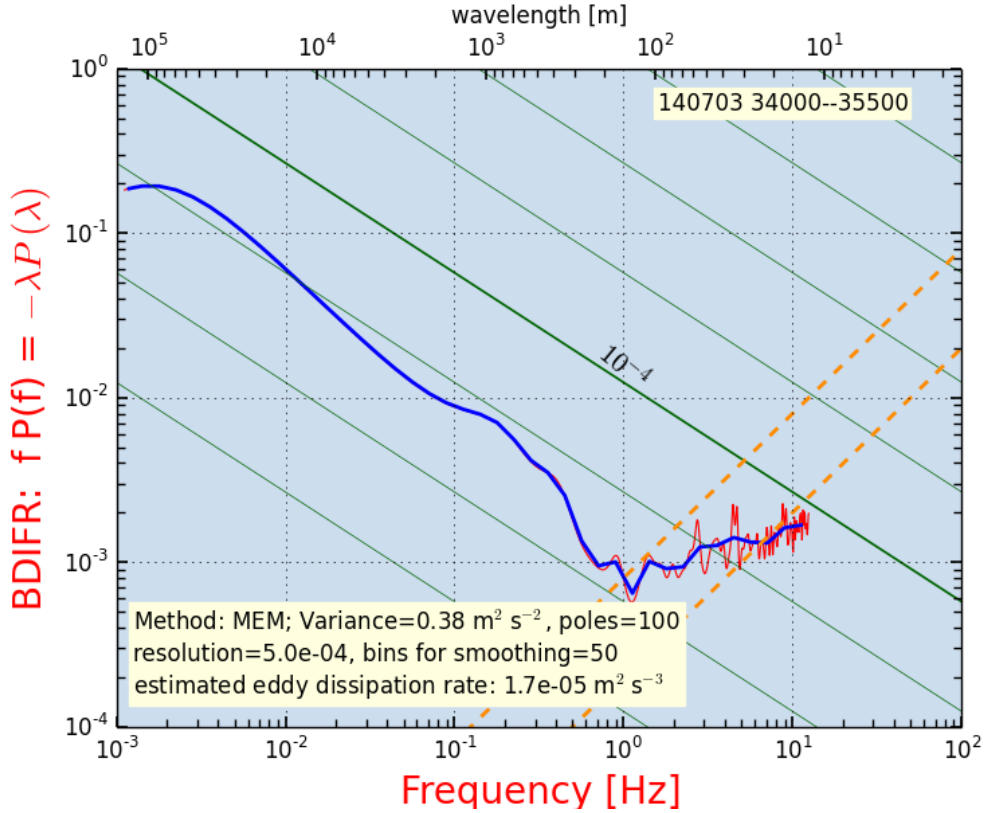


Figure 17: Variance spectrum for BDIFR for DEEPWAVE flight 15, 3:40–3:55 UTC. The dashed orange lines indicate expected white-noise spectra for respective standard deviations of 0.1 and 0.05 hPa. Units for $fP(f)$ are hPa² per logarithmic interval in frequency.

As for vertical wind, the GPS-measured components of aircraft motion relative to the Earth have uncertainty significantly less than that of the relative wind, so errors are dominated by those arising from the relative-wind components and from the transformation to Earth coordinates. The first-order equation for the lateral component of the relative wind (v_y), analogous to Eq. 27, is $v_y = V\beta$ where β is the sideslip angle. V is known to typically 0.05% so the error is dominated by that in sideslip and in heading. For the random error, one limit is obtained as for angle-of-attack by examining the variance spectrum in calm conditions. However, BDIFR and SSLIP do not exhibit such pure noise spectra at high frequency as did ADIFR and AKRD. The QCF variance spectrum has characteristics of noise for amplitudes of random errors of about 0.15 hPa, slightly higher than estimated for ADIFR. For BDIFR, an example is shown in Fig. 17.

The slope in the high-frequency region does not match that expected for a white-noise signal, for which the variance would be constant and in these plots, where the spectral density is multiplied by the frequency, the plotted line should increase linearly with frequency parallel to the orange dashed lines. Instead, the spectrum for BDIFR has smaller slope than this, looking perhaps as if the spectrum starts out at a point where a white-noise spectrum with standard deviation 0.1 hPa

element	uncertainty source	bias	random	δ_w bias [m/s]	δ_w random [m/s]
1	ADIFR transducer	0.07 hPa	0.002 hPa	–	–
2	AKRD coefficients	0.01°	0.001°	0.04	0.004
3	BDIFR transducer	0.07 hPa	0.002 hPa	–	–
4	QCF transducer	0.34 hPa	0.01 hPa	<0.02	0.001
5	pitch	0.02°	0.007°	0.08	0.03
6	GV vertical velocity	0.03 m/s	<0.03 m/s	0.03	<0.03
7	PSF transducer	0.10 hPa	0.001 hPa	–	–
8	ATX	0.3°	0.1°C	–	–

Table 4: Elemental contributions to the uncertainty in measurement of vertical wind by the radome-based system. Entries ‘–’ indicate negligible contribution to uncertainty.

would be appropriate, but then is filtered or otherwise smoothed⁵ so that at the high-frequency limit the equivalent white-noise standard deviation would be 0.05 hPa. The spectrum for SSLIP looks similarly filtered, with an equivalent white-noise spectrum somewhere in the range of 0.02°, similar to that characterizing AKRD. However, the estimated uncertainty in the bias for the combined effects of sideslip and heading was, from the circle analysis, 0.02 ± 0.09 °, and these lead to contributions to the uncertainty in bias of the lateral wind of about 0.3 m/s. The horizontal wind thus has an asymmetrical estimated uncertainty, about three times as large for the lateral component as for the longitudinal component.

Like vertical wind, this uncertainty estimate for the horizontal wind needs to be refined for application to the Earth-relative wind by consideration of the uncertainty in the determination of sensitivity coefficients for sideslip and other contributions to the net uncertainty in wind.

3.3 Elemental sources, vertical wind

Next, we tabulate the elemental sources of uncertainty in the measurement of vertical wind.

3.3.1 Radome-based system

Table 4 summarizes the results for the radome-based wind system. The following is a discussion of the individual elements in that table.

1. **ADIFR:** See Sect. 2.2.5 and Table 1. The uncertainty is assigned to bias because it is likely a calibration uncertainty and the resolution and stability are much smaller than this

⁵perhaps by the response in the lines connecting the ports to the pressure sensors

bias. However, a calibration bias in this measurement does not affect the final wind measurement because the procedure in Sect. 4.1.2 determines the angle of attack from flight data in a way that can be considered a calibration of the measurement of angle of attack, and a bias in ADIFR would be reflected in a change in sensitivity coefficients determined in that section that would compensate for that bias. Only random errors in ADIFR would propagate to the final measurement w , and such errors are thought to be negligible, so the propagated error for ADIFR is listed as negligible. The next item considers the determination of sensitivity coefficient for angle of attack and is the dominant contribution to uncertainty in w arising from the measurement of angle of attack.

2. **AKRD coefficients:** The calibration procedure of Sect. 4.1.2 effectively removes the effects of possible biases in ADIFR and QCF and instead replaces them with uncertainties arising from the coefficients $\{c_0, c_1\}$ in (37). The estimated bias and random error are those obtained and discussed in that section using the estimated uncertainties in the coefficients in (37). For propagation to vertical wind w , (31) indicates that the result is approximately $\delta w = V \delta \alpha$ where V is true airspeed TASX, with additional contributions from correlated errors involving V that are small in comparison to that listed. A typical value for V is about 240 m s^{-1} , leading to the listed elemental uncertainties in w arising from uncertainty in AKRD. It is important, though, that the calibration is dependent on the assumption that the mean vertical wind where the calibration data were collected be zero. This is discussed in Sect. 4.1.2. There is no independent way to check this except by comparing results from different regions as done in this report. That remains a major weakness in calibration and is the major contributor to uncertainty in angle of attack, but it introduces a bias arising from a possible calibration error. Fluctuations from the mean value are measured with uncertainty a factor of ten smaller than this bias. The assumed mean value of the vertical wind leading to this bias was $\pm 0.03 \text{ m/s}$, which could well be an over-estimate for the large datasets used in Section 4.1.2.
3. **BDIFR:** The sideslip angle has negligible effect on the vertical wind as long as the roll angle is small, so for measurements made during straight-and-level flight this contribution to uncertainty in vertical wind is negligible.
4. **QCF:** The values listed are the characteristics of the transducer. Application of the calibration procedure based on comparison to the laser air motion sensor (Cooper et al. [2014]) led to an alternate uncertainty estimate of 0.3 hPa . As in the case of ADIFR, the procedure to determine sensitivity coefficients removes any effect of bias in QCF by calibration in terms of the coefficients $\{c_0, c_1\}$ so the effect on bias in w is replaced by possible bias in those coefficients, as discussed for element 2. The effect of a random error in QCF of 0.01 hPa is, from (37), to introduce an uncertainty in angle of attack of about 0.0002° or a contribution to uncertainty in w of less than 0.001 m s^{-1} . QCF is also used to determine the true airspeed, which affects w , but the effect is negligible for the estimated uncertainty in QCF ($<0.2\%$ of the measured value of w , or 0.02 m s^{-1} for 10 m s^{-1} vertical wind).
5. **PITCH:** The estimates listed are those that apply without the pitch-correction procedure of Sect. ???. In that section, it was estimated that the standard error in pitch is 0.02° and

that this is primarily in the form of a slowly varying error that, over measurement periods short compared to the Schuler oscillation period of 84.4 min, will appear as a bias. The correction procedure represented by Eq. 60 corrects for this error well enough to leave the residual bias negligible, so the bias entry in Table 4 can be eliminated by application of that algorithm. The partitioning between bias and random uncertainty depends on the interval considered, because Schuler precession will cause variation in this error with the Schuler-oscillation period of about 84 min. For periods long compared to this the error will have the character of a random-error component, so using 0.08 m/s would be appropriate for random uncertainty of such long-term measurements while the bias should be reduced substantially, perhaps to 0.02 m/s. For periods small compared to the Schuler period, the pitch error appears as a bias and there is a much smaller random error, evaluated in Sect. ?? to be about 0.007° in pitch or about 0.03 m/s in vertical wind. This is the usual case for measurements of interest, so the bias and random errors are partitioned as appropriate for this case in the table. The uncertainty in pitch is the leading contributor to the standard uncertainty in vertical wind and is also the leading contributor to the overall estimate of bias. The correction technique of Sect. ?? is not incorporated in routine processing so needs special calculation.

6. **Aircraft Vertical Velocity:** The measurement used for vertical motion of the aircraft is discussed in Sect. 5.2. The values listed here are those specified for measurements when “OmniSTAR” corrections are available; if not, the values should be increased to about 0.1 m s^{-1} and so will make a contributor to uncertainty in vertical wind that is comparable to the contributions from pitch and angle of attack. The error in aircraft vertical speed is likely a mixture of bias and random error, because the primary source is uncertainty in ionospheric corrections which will be persistent for important parts of flights but likely to change at least from flight to flight. Because of the likely persistence of the error, it is assigned here primarily to bias.
7. **PSF:** The measured ambient pressure affects vertical wind only through the dependence of true airspeed TASX on PSF, as described in the document on [RAF processing algorithms](#), Section 4.7.1. Evaluation at typical values shows that the dependence of measured vertical wind on uncertainty in this variable is negligible. For example, TASX for PSF=300 hPa, QCF=80 hPa, and ATX=-40°C differs from that for PSF=300.1 by 0.03 m s^{-1} or about 0.01%, so this would also be the percentage change in vertical wind.
8. **ATX:** Temperature is needed to calculate TASX, but as for PSF the effect is negligible. This was tested as for PSF by evaluating at representative points. A representative result was that the listed bias in temperature would lead to a bias in TASX of about 0.05%, leading to a similar percentage change in the value of the vertical wind. This is negligible in comparison to other sources of uncertainty.

The result of adding the elemental sources of uncertainty in quadrature is a bias estimate of 0.10 m s^{-1} and a random-uncertainty estimate of 0.04 m s^{-1} , with pitch correction. Without the correction, the bias estimate increases to 0.35 m s^{-1} , so the pitch correction results in significant reduction in uncertainty and without that correction the uncertainty is dominated by the bias introduced by the measurement of pitch. In the corrected case, the dominant contributions

element	uncertainty source	bias	random	δ_w bias [m/s]	δ_w random [m/s]
1	ADIF_GP transducer	0.07 hPa	0.002 hPa	–	–
2	AK_GP coefficients	0.01°	0.001°	0.04	0.004
3	BDIF_GP transducer	0.07 hPa	0.002 hPa	–	–
4	QCF/QC_GP transducer	0.34 hPa	0.01 hPa	0.02	0.001
5	pitch	0.04°	0.02°	0.17	0.08
6	GV vertical velocity	–	0.07 m/s	–	0.07
7	PS_GP transducer	0.10 hPa	0.001 hPa	–	–
8	ATX	0.3°	0.1°C	–	–

Table 5: Elemental contributions to the uncertainty in measurement of vertical wind using the gust pod. Entries ‘–’ indicate negligible contribution to uncertainty.

are those from pitch and angle of attack, as was argued in the preliminary discussion in Section 3.2. The bias and random errors from pitch and from angle of attack, as listed here, arise from different sources so it is reasonable to combine them in quadrature to obtain composite estimates.

The APPLANIX IRU should provide another route to improvement in the measurement of pitch, because it offers significantly lower specified uncertainty. It achieves this through use of a full Kalman-filter correction to the measurements, which would remove the need for the pitch correction proposed in this document.

3.3.2 Gust-pod system

For the gust pod system, many of the uncertainties associated with measurement components are known less well than for the radome system, but some similar estimates can be made. This section will duplicate the structure of the radome-based system, but will be less definitive and more sketchy in some of the components while emphasizing the differences that apply to the gust pod.

Table 5 lists the elemental contributions to uncertainty in the measurement of vertical wind from the gust-pod system. The following is a discussion of the individual elements in that table.

1. **ADIF_GP:** See Sect. 2.2.5 and Table 1. See the discussion related to the radome. The same transducers are used for the pressure measurements on the gust pod, although the configuration of ports is different. The next item considers the determination of sensitivity coefficient for angle of attack and is the dominant contribution to uncertainty in w arising from the measurement of angle of attack.

2. **AK_GP coefficients:** The calibration procedure of Sect. 4.1.3 effectively removes the effects of possible biases in ADIFR and QCF and instead replaces them with uncertainties arising from the fit coefficients $\{b_{0--3}\}$ in (38). It was necessary to use additional terms to obtain a good fit in this case, but the final result provided a very good representation of the data, as good as in the radome case. We have therefore used the same uncertainty estimate as for the radome, although with less justification and study. As for the radome, the dominant source of bias is again the uncertainty in vertical wind in the calibration region, which is the same for this data set as for that used to determine the radome sensitivity coefficients, so this estimate remains the same as for the radome. The uncertainties also propagate to the vertical wind in the same way. However, the restriction to low roll angle (less than 5° from vertical) is still more important in the case of the gust pod because the CMIGITS IRU used with the gust pod is not aligned with the aircraft longitudinal axis but rather is mounted in an under-wing pod that was designed to point into the airflow and therefore slightly inward relative to the longitudinal axis. That causes significant problems in turns because the IRU rotates in ways that mix the attitude angles.
3. **BDIF_GP:** The sideslip angle has negligible effect on the vertical wind as long as the roll angle is small, so for measurements made during straight-and-level flight this contribution to uncertainty in vertical wind is negligible.
4. **QCF and QC_GP:** Two measurements are listed because both are used in the calculation of vertical wind. QC_GP is used with ADIF_GP to determine the angle of attack, and the calibration described with item 2 effectively replaces uncertainty in this measurement with uncertainty in the sensitivity coefficients. However, true airspeed is determined using QCF because the conventional true airspeed is thought to be superior to the new value determined solely from the gust pod (Section 4.3). Therefore, the effect of uncertainty in QCF on vertical wind is the same as that for the radome because the same calculated true airspeed is used for both.
5. **pitch (CPITCH_GP):** As was the case for the cabin-mounted inertial systems, there were two nearly identical inertial systems used in the wing pods, one for the gust pod and the other for the LAMS, so it is again possible to compare the measurements and obtain estimates of the random errors in their measurements. For both units (LAMS and gust pod), the inertial systems use GPS measurements with a Kalman filter to apply corrections, but they align independently and so have different errors and Schuler oscillations. There were many flights in DEEPWAVE where one of these was not operational: 1–4, 6–7, 15, 17, 19. For the other flights, the standard deviation in the difference in pitch between these two units was 0.06° , so this is a reasonable estimate of the random error that characterizes these measurements.⁶ As for the radome, a true bias in this measurement (e.g., from misalignment at installation) has been subsumed by the calibration of item 2 so does not enter in this item. However, the remaining error on most flights has a slowly varying component (consistent with the long time period of the Schuler oscillation) and so appears as a bias for any measurement made over a period short compared to the Schuler

⁶The standard deviation in the difference between two variables is actually $\sqrt{2} \times \delta$ where δ is the standard deviation in each variable, so a better estimate is 0.04; this correction has not been made throughout this document.

oscillation, so it appears appropriate to assign the observed standard deviation primarily to a bias because it will appear steady in normal applications that look at vertical wind over periods short compared to the Schuler oscillation. We have therefore partitioned the standard deviation into estimated components of 0.04° bias and 0.02° random error. The uncertainty in pitch is the leading contributor to the standard uncertainty in vertical wind and is also the leading contributor to the overall estimate of bias.

6. **Aircraft Vertical Velocity:** For the gust pod, the measurement of vertical motion of the aircraft must be that from the IRU mounted in the under-wing pod because the wing can flex and vibrate and the aircraft can roll in ways that cause that vertical motion to differ from that sensed in the cabin. Again, comparing the two units mounted in side-by-side wing pods provides the best indication of the random component of uncertainty in this measurement, because both units experience almost identical vertical motion. These two units measure project-mean vertical aircraft motions that differ by 0.04 m/s , with standard deviation in that difference of 0.07 m/s . It seems reasonable then to estimate the random component of uncertainty as 0.07 m/s , but the bias is more uncertain. Good flights usually produced mean vertical aircraft motion from takeoff to landing of less than 0.005 m/s , so it is reasonable to neglect the possible bias in this measurement (which is updated for stability in the IRU using pressure altitude as a reference).
7. **PSF:** The measured ambient pressure affects vertical wind only through the dependence of true airspeed TASX on PSF, as described in the document on [RAF processing algorithms](#), Section 4.7.1. The effect is the same as for the radome, and is negligible; see the discussion above for the radome system.
8. **ATX:** Temperature is needed to calculate TASX, but as for PSF the effect is negligible. See the radome discussion above.

The result of adding the elemental sources of uncertainty in quadrature is a bias estimate of 0.18 m s and a estimate of random uncertainty of 0.11 m s^{-1} . The dominant contribution in both cases is that from measured pitch, although the uncertainty in vertical motion of the aircraft also makes a significant contribution to the random component of uncertainty. It is important that these estimates only apply to cases where the roll is within 5° of level.

3.4 Elemental sources, horizontal wind

3.4.1 Radome-based system

Table 6 lists the elemental contributions to uncertainty in the measurement of horizontal wind from the radome-based system. The following itemization discusses each element.

1. **BDIFR:** The primary uncertainty in BDIFR is assigned to bias because it is likely a calibration uncertainty and the resolution and stability are much smaller than this bias. However, a calibration bias in this measurement does not affect the final wind measurement because the procedure in Sect. 4.1.2 determines the sideslip angle from flight data

element	uncertainty source	bias	random	$\delta u_{\perp, \parallel}$ bias [m/s]	$\delta u_{\perp, \parallel}$ random [m/s]
1	BDIFR transducer	0.07 hPa	0.002 hPa	–	–
2	SSRD coefficients	0.03°	0.002°	(0.12, –)	(0.01, –)
3	ADIFR transducer	0.07 hPa	0.002 hPa	–	–
4	QCF transducer	0.34 hPa	0.01 hPa	(see item 9)	
5	heading	0.09°	0.04°	(0.38, –)	(0.17, –)
6	pitch	0.02°	0.02°	–	–
7	horiz. velocity of GV	0.03 m/s	<0.03 m/s	0.03	0.03
8	PSF transducer	0.10 hPa	0.001 hPa	–	–
9	ATX	0.3°	0.1°C	(–, 0.16)	(–, 0.05)
10	δq	0.2 hPa	0.1 hPa	(–, 0.3)	(–, 0.15)

Table 6: Elemental contributions to the uncertainty in measurement of horizontal wind by the radome-based system. Entries ‘–’ indicate negligible contribution to uncertainty. Entries with subscript \perp refer to the lateral component of the horizontal wind, and those with subscript \parallel indicating parallel refer to the longitudinal component (along the axis of the aircraft).

in a way that can be considered a calibration of the measurement of sideslip, and a bias in BDIFR would be reflected in a change in sensitivity coefficients determined in that section that would compensate for that bias. Only random errors in BDIFR propagate to the final measurement of horizontal wind, and the effect of the listed random error is typically less than 0.0001 m/s in lateral wind, with even smaller contribution to the longitudinal wind. These contributions therefore are listed as negligible in the table. The next item considers the determination of sensitivity coefficient for sideslip and is the dominant contribution to uncertainty in horizontal wind arising from the measurement of sideslip.

2. **SSRD coefficients:** The calibration procedure of Sect. 4.1.2 effectively removes the effects of possible biases in BDIFR and QCF and instead replaces them with uncertainties arising from the coefficients $\{e_0, e_1\}$ in (41) and the ability of the selected formula to represent the calibration data. The uncertainty in the first coefficient, the main contributor to sideslip bias, is obtained from the standard deviation in the mean of results from the circle analysis, summarized in Sect. 6.1.6. For propagation to lateral horizontal wind, (??) indicates that the result is approximately $\delta u_{lateral} = V \delta \beta$ where V is true airspeed TASX, with additional contributions from correlated errors involving V that are small in comparison to that listed. A typical value for V is about 220 m s^{-1} , leading to the listed elemental uncertainties in horizontal wind arising from uncertainty in SSRD.
3. **ADIFR:** See Sect. 2.2.5 and Table 1. The angle of attack has negligible effect on the horizontal wind as long as the roll angle is small, so for measurements made during straight-and-level flight this contribution to uncertainty in horizontal wind is negligible.

4. **QCF:** The values listed are the characteristics of the transducer. Application of the calibration procedure based on comparison to the laser air motion sensor (Cooper et al. [2014]) led to an estimated standard uncertainty of 0.1 m/s for steady flight conditions and 0.3 m/s for fluctuating conditions, so this is used for the table entry pertaining to the wind component in the direction of the longitudinal axis of the aircraft. For the lateral component, QCF affects the calculated sideslip SSRD, but as in the case of AKRD the procedure to determine sensitivity coefficients removes any effect of bias in QCF by calibration in terms of the coefficients $\{c_0, c_1\}$ so a potential bias in QCF does not enter the lateral component of the horizontal wind but instead is replaced by possible bias in those coefficients, as discussed for element 2. The effect of a random error in QCF of 0.01 hPa for a typical value of $\text{QCF} \approx 100 \text{ hPa}$ is, from (??), to introduce an uncertainty in sideslip of about 0.01% or, because typical values of sideslip are smaller in magnitude than 1° , an error propagated to horizontal wind smaller than 0.001 m/s. This contribution is therefore neglected.
5. **HEADING:** The random error in heading can be evaluated by comparing two duplicate IRUs, as was done for pitch. The two systems on the GV for DEEPWAVE differed in mean heading by about 0.45° , evidently a result of an alignment error on installation. However, the standard deviation of the difference between the two measurements was only 0.04° , a value that indicates the systems may perform better than the manufacturer's specification (0.2°) would indicate. The uncertainty in the bias evaluated from the circle-maneuver study of Sect. XXX is about 0.09° , so this will be used as the bias estimate while 0.04° is considered the random component of uncertainty in heading.
6. **PITCH:** The contribution to uncertainty from the measurement of pitch was discussed above in connection with measurement of the vertical wind. However, in the case of horizontal wind, for level flight with negligible roll an uncertainty in pitch makes negligible contribution to uncertainty in either component of the horizontal wind.
7. **Horizontal Velocity Components of the Aircraft:** The measurement of horizontal wind is the sum of the relative wind and the horizontal motion of the aircraft relative to the Earth, so uncertainty in this component enters directly into uncertainty in the measured wind components.
8. **PSF:** The measured ambient pressure affects horizontal wind only through the dependence of true airspeed TASX on PSF, as described in the document on **RAF processing algorithms**, Section 4.7.1. Evaluation at typical values shows that the dependence of the measured lateral component of the horizontal wind on uncertainty in this variable is negligible. For example, TASX for $\text{PSF}=300 \text{ hPa}$, $\text{QCF}=80 \text{ hPa}$, and $\text{ATX}=-40^\circ\text{C}$ differs from that for $\text{PSF}=300.1$ by 0.03 m s^{-1} or about 0.01%, so this would also be the percentage change in the lateral component of the relative wind.
9. **ATX:** Temperature is needed to calculate TASX, and other studies (Cooper et al. [2014]) indicate that the temperature uncertainty is about 0.3°C , and this error will propagate to uncertainty in both components of the horizontal wind. Typical values of Mach number for the DEEPWAVE project were 0.8, for which a temperature change of $+0.3^\circ\text{C}$ led to an

increase in true airspeed of about 0.16 m/s. The temperature error is likely a bias, so this difference also should be treated as a bias. The result is that the longitudinal component of the horizontal wind has an elemental contribution from temperature of 0.16 m/s, while the lateral component (being small and having an error proportional to the error in TASX of about 0.16/240 or smaller than 0.1%) has negligible error from this source.

10. **PCOR:** The dynamic and static pressure measurements are corrected for the static defect at the pressure ports using the formulas developed in (Cooper et al. [2014]). The uncertainty in the determination of the correction was estimated in that source as less than 0.3 m/s. Here we use similar estimates of 0.2 (bias) and 0.1 hPa (random error), correlated such that the error in static pressure is the negative of the error in dynamic pressure. For DEEPWAVE research flights these errors propagate to 0.3 m/s bias and 0.15 m/s random uncertainty.

For the lateral component of the wind, adding the elemental contributions to uncertainty in quadrature leads to a net bias estimate of 0.4 m/s and a random uncertainty of 0.2 m/s. The measurement of heading makes a dominating contribution to each. For the longitudinal component, the corresponding results are 0.3 and 0.2 m/s. Here the dominant contribution arises from the corrections applied to dynamic pressure to address the measured static defect as determined from calibrations. Measurements of the longitudinal wind provided by the LAMS have uncertainty of only about 0.1 m/s, so when this instrument is available the uncertainty could be reduced; the tabulated uncertainty includes an estimate of how well the parameterized function used to correct pressure in the absence of LAMS actually represents those measurements adequately. Some of the uncertainty entering this assessment arises because the LAMS and the radome gust-sensing system measure at locations displaced from each other and so may encounter slightly different wind conditions.

3.4.2 Gust-pod system

1. **BDIF_GP:** The primary uncertainty in BDIF_GP is assigned to bias because it is likely a calibration uncertainty and the resolution and stability are much smaller than this bias. However, a calibration bias in this measurement does not affect the final wind measurement because the procedure in Sect. 4.2.2 determines the sideslip angle from flight data in a way that can be considered a calibration of the measurement of sideslip, and a bias in BDIF_GP would be reflected in a change in sensitivity coefficients determined in that section that would compensate for that bias. Only random errors in BDIF_GP propagate to the final measurement of horizontal wind, and the effect of the listed random error is typically less than 0.0001 m/s in lateral wind, with even smaller contribution to the longitudinal wind. These contributions therefore are listed as negligible in the table. The next item considers the more uncertain determination of sensitivity coefficient for sideslip.
2. **SS_GP coefficients:** The calibration procedure of Sect. 4.2.2 effectively removes the effects of possible biases in BDIF_GP and QC_GP and instead replaces them with uncertainties arising from the coefficients $\{e_0, e_1\}$ in (41) and the ability of the selected formula to represent the calibration data. For sideslip, the fit procedure used values of heading

element	uncertainty source	bias	random	$\delta u_{\perp, \parallel}$ bias [m/s]	$\delta u_{\perp, \parallel}$ random [m/s]
1	BDIFR transducer	0.07 hPa	0.002 hPa	–	–
2	SSRD coefficients	0.03°	0.3°	(0.12, –)	(1.25, –)
3	ADIFR transducer	0.07 hPa	0.002 hPa	–	–
4	QCF transducer	0.34 hPa	0.01 hPa	(see item 9)	
5	heading	0.17°	0.3°	(0.7, –)	(1.2, –)
6	pitch	0.02°	0.02°	–	–
7	horiz. velocity of GV	0.05 m/s	0.05 m/s	0.05	0.05
8	PSF transducer	0.10 hPa	0.001 hPa	–	–
9	ATX	0.3°	0.1°C	(–, 0.16)	(–, 0.05)
10	δq	0.2 hPa	0.1 hPa	(–, 0.3)	(–, 0.15)

Table 7: Elemental contributions to the uncertainty in measurement of horizontal wind from the gust pod.. Entries ‘–’ indicate negligible contribution to uncertainty. Entries with subscript \perp refer to the lateral component of the horizontal wind, and those with subscript indicating parallel refer to the longitudinal component (along the axis of the aircraft).

and ground speed components determined from the gust-pod IRU, but wind components determined from the radome system. This allowed better determination of sensitivity coefficients than would have been possible from "bootstrapping" gust-pod measurements using repeated iterations, because the wind measurements from the radome system have lower uncertainty than those from the gust-pod system. However, this means for example that the offset in sideslip or heading will be dependent on the values from the radome system. Adjustment using the circle maneuvers of Sect. 6.1.5 is not possible for the gust pod because the wind measurements are compromised at the high bank angles required for the circle maneuver, so other adjustment is necessary. Values of SS_GP are at least as uncertain as those from SSRD because the SS_GP calibration uses wind measurements determined from SSRD, so the values in Table 6. 0.03 and 0.002°, are lower limits for the uncertainty in calibration coefficients from the gust pod. However, the standard deviation between sideslip measured by the radome (SSRD) and that measured by the gust pod (SS_GP) is typically about 0.3°, an indication that the uncertainty in SS_GP may be much larger.⁷ This large standard deviation might arise partly from different turbulent components being measured at the radome and at the gust pod, but this seems unreasonably high for that explanation because the standard deviation corresponds to a standard deviation in the difference in lateral wind at the two locations of 1.25 m/s. Instead, it appears that there is some source of error affecting SS_GP and that the elemental uncertainty assigned to the random error arising from application of the SS_GP calibration must be increased

⁷For comparison, the standard deviation in the difference between AKRD and AK_GP is only 0.09°.

to 0.3° until this discrepancy between SSRD and SS_GP can be resolved.

3. **ADIFR:** See Sect. 2.2.5 and Table 1. The angle of attack has negligible effect on the horizontal wind as long as the roll angle is small, so for measurements made during straight-and-level flight this contribution to uncertainty in horizontal wind is negligible.
4. **QCF and QC_GP:** The values listed are the characteristics of the transducers. Application of the calibration procedure based on comparison to the laser air motion sensor ([Cooper et al. \[2014\]](#)) led to an estimated standard uncertainty of 0.1 m/s for steady flight conditions and 0.3 m/s for fluctuating conditions, so this is used for the table entry pertaining to the wind component in the direction of the longitudinal axis of the aircraft. For the lateral component, QC_GP affects the calculated sideslip SS_GP, but the procedure to determine sensitivity coefficients removes any effect of bias in QC_GP by calibration in terms of the coefficients $\{c_0, c_1\}$ so a potential bias in QC_GP does not enter the lateral component of the horizontal wind but instead is replaced by possible bias in those coefficients, as discussed for element 2. The effect of a random error in QCF of 0.01 hPa for a typical value of $\text{QCF} \approx 100 \text{ hPa}$ is, from [\(??\)](#), to introduce an uncertainty in sideslip of about 0.01% or, because typical values of sideslip are smaller in magnitude than 1° , an error propagated to horizontal wind smaller than 0.001 m/s. This contribution is therefore neglected.
5. **HEADING (CTHDG_GP):** The random error in heading can be evaluated by comparing the two duplicate IRUs for the gust pod and the LAMS, as was done for pitch. In DEEPWAVE, these two systems differed in mean heading by about 1.3° , evidently a result of being installed at different angles relative to the aircraft longitudinal axis. The standard deviation in the difference in heading measurements from the two systems, after excluding some additional flights (18, 22, 25) where there appeared to be problems with the measurement, was 0.3° , so the uncertainty associated with this measurement is much higher than that for the radome-based system. The mean difference between the two measurements of heading, averaged over flights, had a standard deviation of 0.17° , so this may be a reasonable estimate of bias, as entered into the table.⁸
6. **PITCH:** The contribution to uncertainty from the measurement of pitch was discussed above in connection with measurement of the vertical wind. However, in the case of horizontal wind, for level flight with negligible roll an uncertainty in pitch makes negligible contribution to uncertainty in either component of the horizontal wind.
7. **Horizontal Velocity Components of the Aircraft:** The measurement of horizontal wind is the sum of the relative wind and the horizontal motion of the aircraft relative to the

⁸Special processing, using a hybrid heading obtained by complementary filtering (cf. Sect. [??](#)) with CTHDG_GP considered the "fast" signal and THDG the "slow" signal, with appropriate adjustment for the discontinuity at 360° and with exclusion of data during and for 1 min after turns, reduced the standard deviation of the difference in heading to less than 0.10° with a similar reduction in estimated bias. The resulting heading variable retains the high-frequency response of the gust-pod IRU, needed to address issues like wing flex or vibration of the pod, but used the higher-quality measurement of heading from the fuselage IRU for long-term updating. This can improve the measurement of horizontal wind from the gust pod significantly, at the expense of having the measurements use a reference measurement outside the instrument. If improvement in the measurement of horizontal wind from the gust pod becomes important, such processing can be used for special cases.

Earth, so uncertainty in this component enters directly into uncertainty in the measured wind components. Comparison among the different measurements of velocity components of the aircraft (<{GGVEW, CVEW_GP, CVEW_LAMS} and {GGVNS, CVNS_GP, CVNS_LAMS}) indicate that, for DEEPWAVE flights with good IRU operation (flights 5, 8–14, 16, 20–21, 23–24, 26) the standard deviations among these measurements are consistent with an uncertainty of 0.05 m/s. This characterizes some combination of bias and random error, so to be conservative this value has been assigned to each in the table.

8. **PSF:** This measurement has the same effect on the wind measurement from the gust pod that it has on the measurement from the radome-based system because the same true airspeed measurement is used for both. See the discussion for the radome system that follows Table 6.
9. **ATX:** Temperature affects wind measured by the gust pod in the same way as that measured by the radome-based system. See the discussion for the radome system that follows Table 6.
10. **PCOR:** The same correction to true airspeed is applied to wind measured by the gust pod as that applied to measurements from the radome-based system. See the discussion for the radome system that follows Table 6.

For the gust-pod system, the uncertainties in the two components of the horizontal wind (lateral and longitudinal relative to the aircraft) are quite different. For the lateral component of the wind, adding the elemental contributions to uncertainty in quadrature leads to a net bias estimate of 0.7 m/s and a random uncertainty of 1.7 m/s. The measurement of heading makes a dominating contribution to each, and the values used for these estimates are the result of inter-comparisons between units and are much higher than the best specifications for the unit listed in Table 2, but as noted there the error can increase fairly significantly if not updated with frequent course changes. For the longitudinal component, the corresponding results are 0.3 and 0.2 m/s. Here the dominant contribution arises from the corrections applied to dynamic pressure to address the measured static defect as determined from calibrations, just as for the radome-based system, because the measurements of the longitudinal component of the wind are the same for both systems.

3.5 Summary

This subsection summarizes the net uncertainty in wind measurements as developed in the earlier parts of this section. See Table 8 for the key results.

3.5.1 The radome-based system.

The standard wind measuring system on the GV is called the radome-based system and results in the basic wind measurements WDC, WSC, and WIC representing the horizontal wind direction (degrees relative to true north), horizontal wind speed (m/s) and vertical wind speed

Table 8: Summary of uncertainty for measurements of wind from the GV. The two entries for bias for the horizontal wind are first the component lateral to the axis of the aircraft and second the component parallel to the axis of the aircraft.

Measurement	bias	random uncertainty	net uncertainty	notes
vertical wind, radome	0.1	0.04	0.1	lower with pitch correction ^a
horizontal wind components, radome	0.4 , 0.3	0.2	0.4	roll < 5° ^b
vertical wind, gust pod	0.18	0.11	0.2	roll < 5° ^c
horizontal wind components, gust pod	0.7, 0.3	1.7, 0.2	1.8, 0.4	best conditions ^d

^aWith application of the pitch-correction algorithm of Sect. ??, Eq. 60, the bias estimate is 0.05 m s⁻¹ and the net uncertainty is 0.06 m/s.

^bExpect minor degradation in turns.

^cErrors may be much larger in turns.

^dSelected flights in DEEPWAVE; can be factor-of-2 more uncertain for worst flights. Must qualify heading measurement by comparison to another measurement to get the listed performance. Not valid in turns.

(m/s). For this system, the estimated bias limit, random component of standard uncertainty, and combined standard uncertainty are listed in Table 8. The combined uncertainty is obtained by adding the estimate of bias and the estimate of random error in quadrature, but this characteristic can be questioned because the bias estimate does not have normal statistical characteristics. It is preferable to use the estimates of bias and of the random component of standard uncertainty separately when characterizing a measurement. As an approximation, it is reasonable to consider about 0.4 m/s as the uncertainty in each component of the measurement of horizontal wind and 0.1 m/s as the corresponding uncertainty in vertical wind. In any specific direction, the uncertainty in horizontal wind remains about 0.4 m/s, so this is also the uncertainty in measured wind speed. Translation to uncertainty in wind direction depends on the magnitude of the wind speed: If the wind speed is u and the uncertainty in the component of the wind transverse to the wind speed is δ_u , the uncertainty in wind direction $\delta\xi$ is about δ_u/u . For example, for $u = 20$ m/s and $\delta_u = 0.4$ m/s, $\delta\xi = 0.02$ rad. or about 1° .

There is some potential for improvement in the vertical wind if the pitch-correction algorithm of Section ?? is applied. The improvement in effect removes the bias contribution from pitch, so it reduces the estimated bias to 0.05 m/s and the standard uncertainty to about 0.06 m/s. Further reduction would require independent evidence that the calibration maneuvers are flown where the average wind is smaller than the 0.05 m/s value assumed when obtaining these results, because this then is the dominant remaining uncertainty.

In the case of horizontal wind, the leading uncertainty is that associated with heading, which could be improved by implementation of a full Kalman filter to adjust the heading or by replacement of the IRU with a higher-quality system with inherent Kalman filtering. There are systems available with much lower specified uncertainty that could reduce the uncertainty in lateral wind significantly.

3.5.2 The gust-pod system

The vertical wind measured by the gust pod is surprisingly good, when it is considered that the measurements are made under the wing of the aircraft in a region of seriously distorted airflow. While of lesser quality than the measurements from the radome, the measurements based on the gust pod have estimated uncertainty only about twice that of the radome-based measurement. On the other hand, the measurements of horizontal wind from the gust pod have significantly greater uncertainty than those from the radome. The uncertainty approaches 2 m/s even in the selected best cases, and there are examples where the discrepancy between similar measurements of heading becomes much larger than the tabulated values and the associated uncertainty in horizontal wind becomes even larger. Vertical and horizontal winds are both problematic in turns and should not be used for roll angles exceeding about 5° in magnitude. The problem with measurements in turns arises because the gust-pod system is not aligned with the longitudinal axis of the aircraft so, in turns, the three attitude angles (pitch, roll, heading) become intermixed. It may be that the appropriate angle transformations can be found to handle this problem, but current processing leads to obvious errors in turns.

Some support for this value of uncertainty in vertical wind from the gust pod was provided by Fig. 8, where the two measurements of vertical wind were compared for all measurements from

one flight. The standard error in the difference between the two measurements was 0.27 m/s, while the uncertainties in Table 8 would suggest an expected uncertainty in the difference of 0.22 m/s. While this is slightly lower than the measured difference, some of that difference can arise from real differences in vertical wind at the two locations on the aircraft and from timing differences, so the measured standard error is in reasonable agreement with the expectations from the uncertainty analysis.

Using measurements of horizontal wind from the gust pod is not recommended. That system was designed to provide a back-up measurement that could be anti-iced to remain operational in heavy cloud. In the case of vertical wind, it appears that the system fills this back-up roll well. However, the horizontal wind from the gust pod is much inferior to that from the radome-based system and probably should be used only with much caution. That would involve checking that the measurement of heading from the gust-pod IRU provides measurements in reasonable agreement with other units, considering installation differences in orientation) and excluding turns. An additional restriction arises from the fit restrictions used to determine the coefficients in the equation representing angle of attack. Those restrictions were: true airspeed (TASF) greater than 130 m/s, absolute value of roll less than 5°, and altitude greater than 5000 m. Outside these limits, extrapolation errors can lead to significant errors in the measurements from the gust pod.

The straightforward way to improve the measurements from the gust pod would be to improve the measurement of heading. It might be possible to calculate a surrogate heading from the fuselage IRU and the known installation offset of the gust-pod IRU, but this hasn't been investigated yet and would require continued study beyond that reported here.

3.5.3 Conclusion

The first three lines in Table 8 claim that wind can be measured with low uncertainty from a high-speed aircraft such as the NCAR/NSF GV. This is particularly challenging at high speed because the aircraft introduces flow distortions and pressure variations over and near the fuselage that affect many of the sensors used to measure wind. Calibration by comparison to a laser air-motion sensor has led to improvement in the measurement of horizontal wind and is the basis for achieving these tolerances. Calibration maneuvers, especially those involving flying circles, have provided evidence for the claimed limits to uncertainty and have refined some of the calibrations used to achieve these limits. The fourth line in the table indicates disappointing performance for the gust-pod measurement of the component of horizontal wind lateral to the aircraft, so in general this measurement should not be used for research without further improvement. However, the measurement⁴ of vertical wind from the gust pod provides a useful back-up to the conventional measurement.

4 Sensitivity coefficients

This section reviews the determination of "sensitivity coefficients" that provide parameterized measurements of the angles of the relative wind (angle of attack and sideslip angle) in terms of measured quantities like pressure differences between ports on the radome. These sensitivity coefficients are essential for measurement of the relative wind, as described in Sect. 2.1.2, Eq. (1). DEEPWAVE Flight RF15 on 3 July 2014 was devoted to calibration maneuvers, and measurements from that flight, combined with similar calibration maneuvers flown on RF11 at 40,000 ft, are used to determine sensitivity coefficients for angle of attack (AKRD and AK_GP) and for sideslip (SSRD and SS_GP). A larger data set, described below, is also used to study the representativeness and uncertainty of the resulting sensitivity coefficients. This section also discusses some aspects of the relative timing of the measurements.

4.1 Angle of Attack

4.1.1 Equations underlying the calibration

The first-order expression for the vertical wind w is

$$w = V \sin(\alpha - \phi) + w_p \quad (31)$$

where V is the true airspeed, α the angle of attack, ϕ the pitch, and w_p the vertical motion or rate-of-climb of the aircraft. The solution for the angle-of-attack is

$$\alpha = \phi + \arcsin \frac{w - w_p}{V} \quad (32)$$

If it is reasonable to assume for some period of flight that w is zero, or that it averages to zero, then

$$\alpha^* = \phi - \arcsin \frac{w_p}{V} \quad (33)$$

can be used as a reference angle-of-attack to which to fit a parameterized formula. This fit reference depends on measurements of pitch, rate-of-climb, and true airspeed. Even in the presence of waves, fitting functions of the radome measurements and other flight characteristics to this reference should average any real effects of vertical wind as long as the vertical wind over the flight segments used averages to zero.

The danger in this approach is that a particular data set may not have negligible average mean wind. For example, if a flight spent more time in the updraft regions in the ascending portion upwind of the island and less in the downdraft region downwind of the island, the mean measurement of vertical wind may not be negligible. The functions used for representation of angle of attack always include an offset term along with functions of measurements, so it may be appropriate to adjust that offset if there is evidence that the mean vertical wind should not be zero.

Other steps can be taken to check that offset coefficient, as discussed in subsequent sections. One compromise, followed below, is to determine any coefficients other than the offset term from comprehensive data sets but then revised the constant coefficient in the fit on the basis of special periods expected to average to zero vertical wind, like flight over the ocean well away from weather disturbances or special calibration flights in conditions with apparently level air motions.

In the case of the radome, the relevant variables are $\phi = \text{PITCH}$, $w_p = \text{GGVSPD}$, and $V = \text{TASX}$. The radome measures the pressure difference (ADIFR) between top and bottom ports on the radome, and this pressure is usually normalized by some measure of dynamic pressure like QCF or QCXC or QCRC. The former is preferable because the use of corrected QCXC requires the application of static-defect corrections that themselves depend on α , leading to circularity in the calculation, and QCR and QCRC are sometimes affected by icing or freezing of accumulated water even when ADIFR continues to function.

For the gust pod, the relevant variables are $\phi = \text{CPITCH_GP}$, $w_p = \text{CVSPD_GP}$, and $V = \text{TASX}$. The gust-pod measurements differ from those measured relative to the fuselage; for example, the pitch of the gust pod is several degrees different from that of the fuselage because of the way in which the gust-pod IRU is installed. However, the true airspeed V in (33) is measured better by the fuselage system, so TASX will be used for V . The equation with the appropriate variables is then:

$$\alpha^* = \text{CPITCH_GP} - \arcsin \frac{\text{CVSPD_GP}}{\text{TASX}} \quad (34)$$

”Calibration” of the angle-of-attack (i.e., determining the sensitivity coefficients) then requires determining a function $f(\{x_i\})$ of measured quantities that matches α^* determined from (34). Possible terms $\{x_i\}$ in that function may include ADIFR and related measurements of pressure and dynamic pressure as well as Mach number, and powers and products of these terms. For the Rosemount 858 sensor used with the gust pod, it is expected from theory that one element of $\{x_i\}$ will be ADIF_GP/QC_GP. Wind tunnel and theoretical studies predict how the pressure will vary on a hemispheric surface with changing angles, but those don’t necessarily apply to the mounting location on the GV because there is considerable flow distortion at the under-wing location of the pod and that affects the pressure response to changes in flow angles. Therefore, the best approach is to use the above approach for that sensor also and determine a functional response that matches the calibration data.

4.1.2 Application to the radome

The best method for calibrating angle-of-attack is through the use of speed runs. In this maneuver, the aircraft is slowed to a speed near the lower range of its operating range, then accelerated to near the upper limit, and then slowed again to normal cruise. If this is done while flying a level track, the angle of attack will vary through its normal range and the pitch will vary similarly. If there is no vertical wind or if a fluctuating vertical wind averages to zero, (33) then can be used to provide a reference angle α^* that serves as reference for the parameterized fit. There were three speed runs during RF15, at the times 3:21–3:29, 4:15–4:23, and 5:01–5:11 UTC. On RF11, there was a similar speed run flown from 10:30–10:40. For the purpose of this

first determination of sensitivity coefficients for angle-of-attack, only those periods were used. In addition, because some of the measurements at minimum speed deviated from the otherwise simple fits, only measurements with true airspeed in excess of 130 m/s were used; this eliminated some of the slowest parts of the speed runs, but that is a flight speed not used in normal operation.

In the code being used (cf. WindUncertainty.Rnw), the line

```
AOAREF <- PITCH - asin(GGVSPD/TASX) / Cradeg
```

represents Eq. (33).

The sensitivity to the pressure difference between vertically separated ports is the most important part of the calibration of angle of attack. Secondary terms are sometimes needed to adjust the value to maintain a correct zero. Therefore, the fit was done in two stages. First, the four speed runs alone were used to determine the sensitivity to the pressure ratio, and then a larger dataset was used to incorporate a wider range of flight conditions to check that the fit determined from the speed runs remained representative of the larger data set.. The first fit was to the following simplified equation:

$$\alpha^* = c_0^* + c_1^* \frac{\Delta p_\alpha}{q} \quad (35)$$

A fit to the data is shown in Fig. 18 and tabulated in the following summary of the fit, which was produced by the “R” call at the top of the listing. AOAREFC is α^* with correction to pitch as in Section ?? and AQR= $\Delta p_\alpha/q$.

```
## lm(formula = AOAREFC ~ AQR, data = Data2)
## [1] "Coefficients:"
##              Estimate Std. Error t value Pr(>|t|)
## (Intercept)  4.394    0.005672 774.6     0
## AQR         20.986   0.068937  304.4     0
## [1] "Residual standard error: 0.121, dof=1977"
## [1] "R-squared 0.979"
```

This fit gave coefficients c_0^* and c_1^* equal to 4.394 and 20.986. The fit accounted for 97.9% of the variance and had a residual standard error of 0.12° , so it represents the speed-run data well. In Fig. 18, the thin gray line under the thick orange dashed line represents the uncertainty in the fit result and shows that the uncertainty in representing these data with this set of coefficients is negligible. The more significant uncertainty, however, comes from the assumption that the vertical wind is zero for these periods of the speed runs. Therefore, additional studies will be used below for further evaluation of the uncertainty introduced by this assumption.

This calibration would be affected by a time difference between the IRU measurement of pitch and the data-system sampling of the pressures involved, especially that from the radome. The IRU outputs measurements with a time delay that can be variable and unknown but is expected to be <0.1 s, and normal processing uses an adjustment of 60 ms to compensate for this delay. To guard against this delay affecting the calibration, fits like that leading to the above formula and

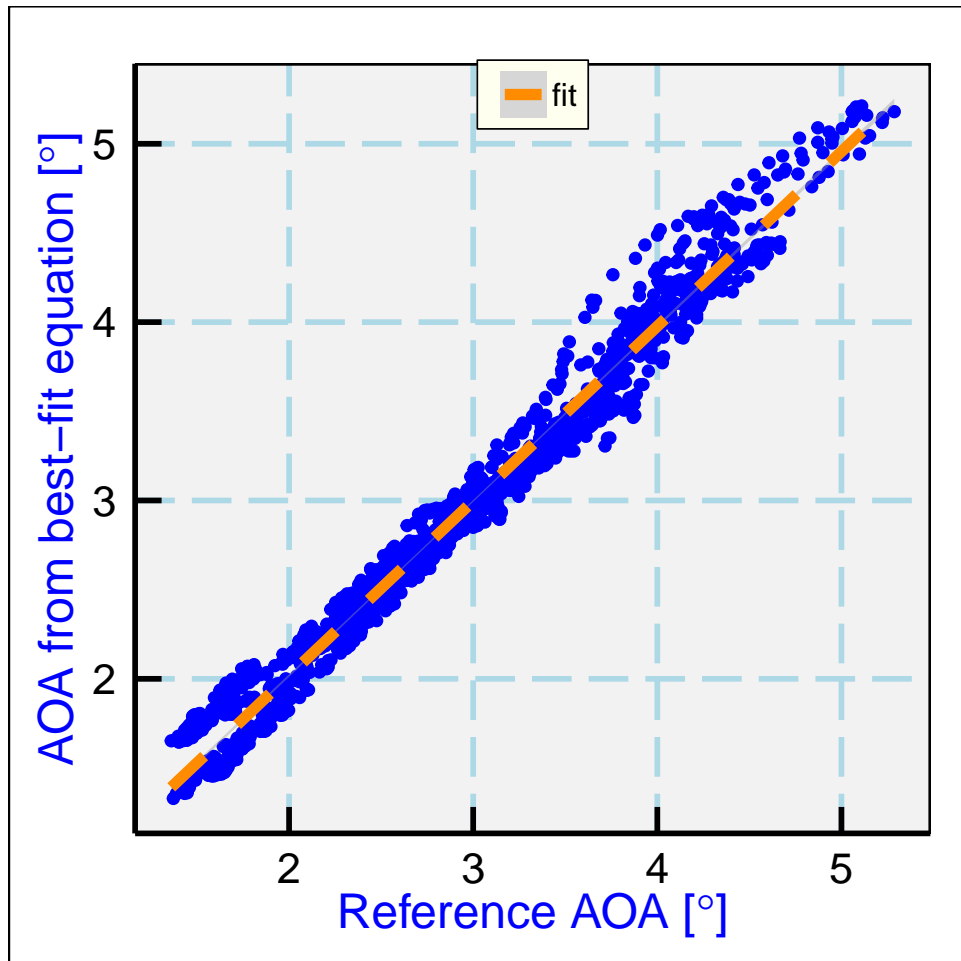


Figure 18: The angle-of-attack determined from the fit to pressure measurements from the radome, as a function of the reference angle provided by Equation (35), for the combination of data from all four speed runs as listed in the text.

coefficients were repeated after shifting the measurement of pitch by various time intervals, both forward and backward. For shifts within about 0.5 s, the results did not change significantly, although the fit with adjustment of pitch *backward* by about 0.5 s had the smallest standard error . Equivalently, a similar standard error was obtained if the measurement of the pressure ratio from the radome (δp_α) were moved forward in time by a similar amount. Neither of these shifts seems likely at this magnitude, and the change in standard error was only about 0.002° , so we interpret this as indicating insensitivity of the calibration to small shifts in time. That is likely a result of the calibration data being from speed runs where the flight speed is gradually increased and then decreased, so any effect of a lag partially cancels in such data segments.

The calibration would also be affected by pitch errors such as are discussed in Sect. ???. Therefore the correction procedure discussed in that section was applied to these data before finding the preceding fit. In comparison to the fit without this correction, the standard error was changed only negligibly and the two fit coefficients changed by -0.007 and -0.004, respectively, so this correction also had only minor effect on the fit, with changes comparable to or smaller than the standard errors in these coefficients. This insensitivity perhaps arises because the period of the calibration spanned a few hours and so included enough time for the Schuler oscillation of pitch to average over the dataset used for calibration.

Previous studies of the radome where low-altitude flight segments were included indicated that an additional term was needed in the calibration to adjust the zero for vertical wind for flight in the boundary layer over the ocean. The standard calibration determined in that way is that given in the RAF document on [Processing Algorithms](#):

$$\alpha = c'_0 + \frac{\Delta p_\alpha}{q} (c'_1 + c'_2 M) \quad (36)$$

with coefficients $\{c'\} = \{4.604, 18.67, 6.49\}$. The last term provides some adjustment dependent on Mach number and corrects an offset often seen in vertical wind at low airspeed.

Figure 19 shows the angle of attack determined from this fit vs. that from the standard formula. The plotted shapes show the distribution in values for centered intervals in the predicted angle-of-attack of $(1/3)$ degree, where the blue shapes and orange line are the results from the fit to the speed-run measurements and the green shapes are the distributions that would result from using the standard calibration. The standard calibration is close to that determined from the speed runs, but the RMS difference between predicted values and fit values increases from 0.12° for the speed-run fit to 0.15° for the standard fit. The difference is most evident for measurements at large angle-of-attack, where the standard coefficients produce increasingly higher values as the angle-of-attack increases.

Because the standard fit in use for the GV include an additional terms representing dependence on Mach number, the benefit of using such a fit for DEEPWAVE is worth considering. The primary reason for that fit has been that otherwise the measurements of vertical wind at low level tend to be biased, but most of the useful flight data from DEEPWAVE was at intermediate or high levels so this may not be a concern for this project.

```
## lm(formula = AOAREF ~ AQR + AQRM, data = Data2)
## [1] "Coefficients:"
```

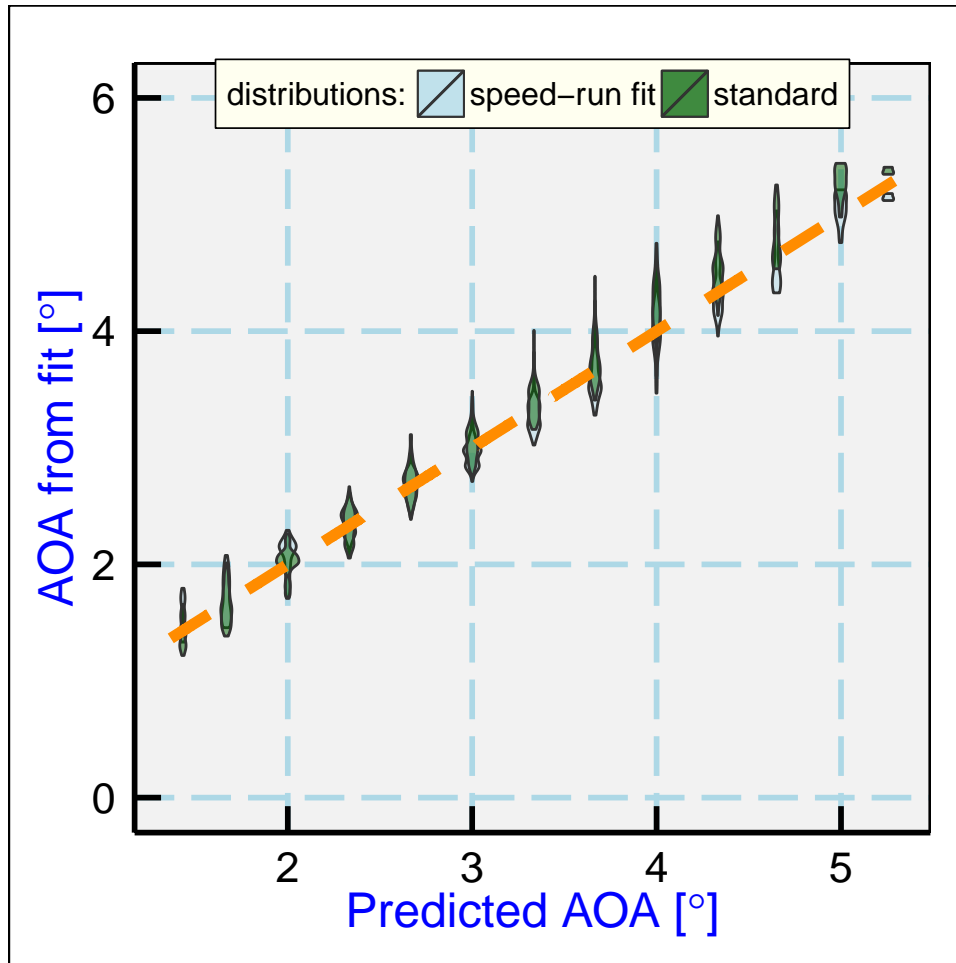


Figure 19: The angle of attack determined from the simple fit to the pressure ratio from the radome, as a function of the angle-of-attack predicted for zero vertical wind from the formula in the text (blue shapes), and the corresponding distribution that would result from using the standard calibration (green shapes). The shapes show the distributions for measurements in centered bins at (1/3)-deg increments in the predicted angle-of-attack. The dashed orange line is the best fit to the speed-run measurements.

```

##             Estimate Std. Error t value
## (Intercept) 4.387   0.005402 812.09
## AQR         17.924   0.216747  82.70
## AQRM        4.295   0.288585 14.88
##             Pr(>|t|)
## (Intercept) 0.000e+00
## AQR         0.000e+00
## AQRM        1.445e-47
## [1] "Residual standard error: 0.115, dof=1976"
## [1] "R-squared 0.981"

```

Fitting (36) to the speed-run data gave a standard error that is reduced by $<0.006^\circ$, so for those measurements this small improvement does not seem to justify adding another term to the fit. This will be revisited later in this section with an expanded data set.

The next step was to expand the data set to include flights from a range of altitudes including up to FL450, and to see if it is necessary to refine the fit to include additional terms like that in Eq. 36 to constrain the zero of the angle-of-attack while preserving the measured sensitivity as in (35). This expanded dataset included RF14, with a FL450 leg from 11:30 to 12:20 UTC; RF16, with a FL430 leg from 9:30 to 11:00 UTC; RF03, all measurements above 35,000 ft flight altitude (to incorporate a long flight where fuel burn-off changed the angle of attack); and an expanded section from RF11 (in addition to the speed runs) from 7:00 to 10:00 UTC, to include a long leg at FL400.

Various fit equations were explored involving terms including the Mach number, the air density, the measured pressures, and various products and powers of these terms including terms multiplied by the basic pressure ratio already included in (35). None of these produced enough improvement over the single-term fit to warrant their inclusion; the best improvement in the residual standard error was about 2%.⁹

The results from the two-coefficient fit to the expanded data set, using

$$\alpha = c_0 + c_1 \frac{\Delta p_\alpha}{q} , \quad (37)$$

led to best-fit coefficients $\{c_0, c_1\} = \{4.468, 21.481\}$ and a standard error of 0.12 for 17,715 measurements. The small increase in standard error in comparison to the speed-run measurements is expected because this expanded data set includes regions more likely to have non-zero vertical wind, which contributes to this error. Expanding this fit to include a third coefficient as in (36) resulted in negligible improvement (0.001°) in the standard error, and introduction of a set of eight possible dependencies while exploring for better fits only led to reduction in the standard error by 0.003° , so more complicated equations than (37) do not appear to be

⁹Additional terms that did improve the fit significantly were those correlated with the terms in Eq. 33, esp. pitch, but including such terms is not consistent with finding a fit that would represent the angle-of-attack in conditions with non-zero vertical wind. For example, including "PITCH" as a term in the fit resulted in a coefficient for this term of about 0.4, and such a large correlation between resulting measurements of angle-of-attack and pitch would bias the response to a true vertical wind. As an extreme example, inclusion of a term based on the right side of Eq. 33 leads to a perfect fit, but use of such a fit would ensure that all measurements of vertical wind would be zero. For this reason, pitch and vertical aircraft motion were excluded from the candidate terms in the fit.

needed.¹⁰ Another fit considered with this expanded data set was to set the slope parameter to the value obtained from the speed-run data, 20.986, and then fit using the expanded data set to determine a value of the offset coefficient that minimized the mean vertical wind. That gave a value for the first coefficient of 4.43 and a standard error negligibly different from that for the two-coefficient fit, so that is another indication that the speed-run dataset and the expanded dataset give consistent results.

The recommended calibration for DEEPWAVE, determined with correction of the pitch errors as discussed in Sect. ??, is (37) with these values for the coefficients: $\{c_0, c_1\} = \{4.468, 21.481\}$.

Evaluation of all the points in the expanded dataset using three fits, that from the expanded dataset, from the speed runs alone, and using the "standard" fit discussed above, gave only very small differences in the results. In Fig. 20 the values of angle-of-attack obtained using the fit to data from the expanded dataset are compared to those obtained using the fit to the speed-run dataset. The angle-of-attack evaluated from the expanded-dataset coefficients resulted in values $0.036 \pm 0.007^\circ$ larger than those from the speed-run coefficients and $0.037 \pm 0.036^\circ$ larger than those from the standard coefficients, so using any of these formulas would give about the same results.

The standard errors in the coefficients for the expanded dataset are respectively 0.0035 and 0.046, so the coefficients are tightly constrained by the fit. The correlation between error terms was very high and positive, but the second coefficient is applied to a term ($\delta p_\alpha/q$) that is typically negative with representative magnitude of about -0.0037° so the correlated uncertainties partially cancel, leaving a net uncertainty in angle of attack of 0.0007° (for 0.99 correlation between the uncertainty terms) as a result of uncertainty in the fit.

The expanded dataset provided results consistent with those from the speed runs alone but contained 17,721 measurements vs. only 2,019 for the speed-run dataset, so this larger set provides an opportunity to examine the consistency of results from subsets of the measurements. For this purpose, randomly selected but exclusive subsets of the data were selected repeatedly and the fit coefficients were determined from each of these subsets. In one example, the dataset was divided randomly into 100 exclusive subsets and the fit coefficients were calculated for each of those subsets, and then this process was repeated 50 times. The resulting standard deviations in the fit coefficients were 0.070 and 0.88. With resampling, the independent samples entering these averages are fewer than 5000 but more than 100, suggesting that the means for the coefficients are known with uncertainties of between 0.007 – 0.001 for the first coefficient and 0.09–0.012 for the second. The estimates from the fit (0.004, 0.053) are midway in these ranges, so the fit results are consistent when the data are partitioned into various subsets. The fit results thus appear reasonably characterized by the estimated standard errors from the fit.

Repeating this for different subset sizes N indicated that the standard deviations in the coefficients scaled in a manner consistent with \sqrt{N} behavior, suggesting that the results are not biased

¹⁰This simpler representation applies to the normal research flight levels of the DEEPWAVE project, levels above about 10,000 ft. Because expanded representations were needed in other projects to represent low-level flight data, and low levels are not included in this expended data set, it may be necessary to revisit this calibration with more terms if lower-level flight segments are to be analyzed.

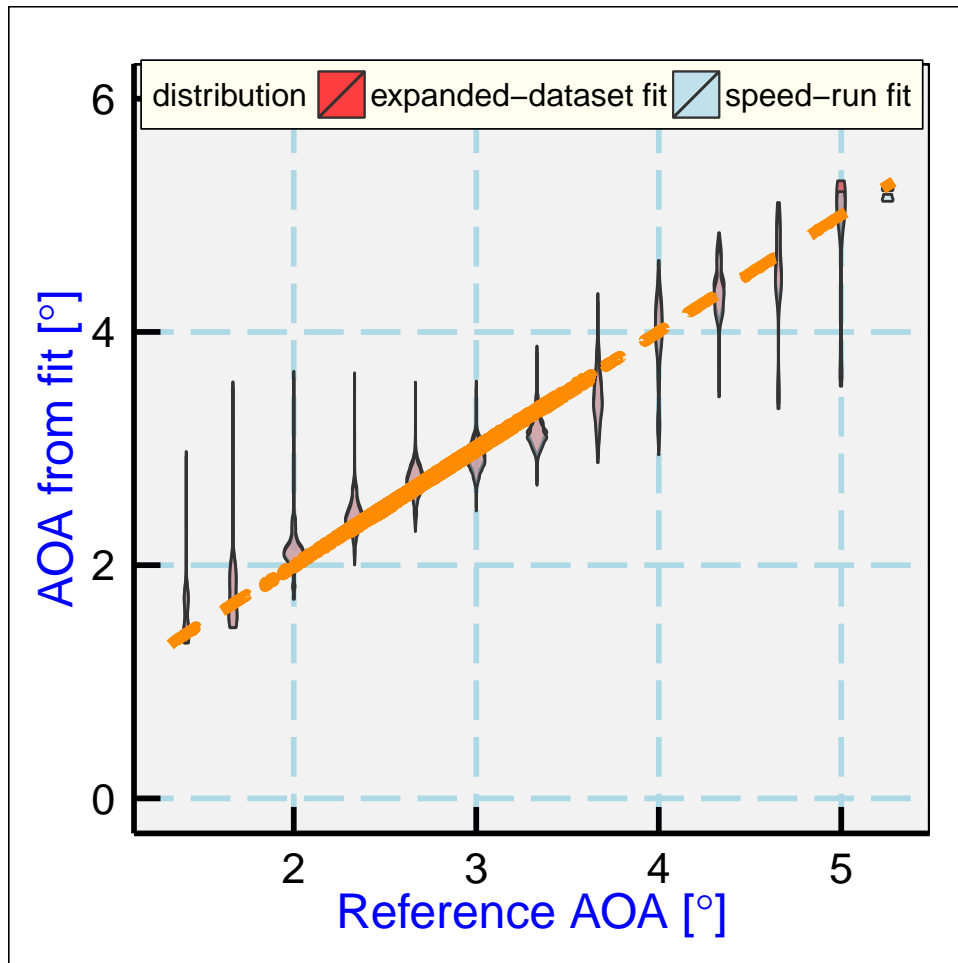


Figure 20: Distributions in the angle-of-attack determined from the two-coefficient fit to the expanded dataset, plotted with the distributions that would result from use of the equation based on the speed-runs only. The pink color denotes regions covered by both distributions.

by isolated outlier measurements such as would occur from regions of extended non-zero vertical wind. The subsetting also produced resulting values for the individual coefficients that were highly correlated, with correlation coefficient around 0.99. This also supports the partial cancellation of uncertainty as evaluated for the fits.

These estimates of uncertainty characterize how well the sensitivity coefficients characterize the data, but the validity of the result is dependent on the mean vertical wind being zero, as discussed in connection with Eq. (32). A non-zero mean vertical wind of 0.1 m/s will introduce bias into the first sensitivity coefficient of magnitude 0.02° , a value much larger than the estimated uncertainty in angle of attack resulting from the fit. This then is the major uncertainty affecting angle of attack and hence vertical wind, and it is difficult to quantify except by estimates of how large the vertical wind might be. For all 1-s measurements of vertical wind in the DEEPWAVE project, the mean vertical wind was 0.03 m/s without correction for pitch errors and <0.01 m/s with such correction, in both cases with a standard deviation of about 0.5 m/s. When measurements are partitioned into groups within $1\text{--}5^\circ$ longitude upwind and downwind of the island crest, using a slanted dividing line approximately matching the orientation of the island, the two groups had respective mean vertical wind measurements of -0.026 and +0.032 m/s, so even over the South Island of New Zealand there was no significant mean vertical wind at the altitude of research flights. It therefore seems reasonable to use a limit of about 0.05 m/s as applicable to the calibration process, and so a bias limit on the first sensitivity coefficient of magnitude 0.01° . This is then the dominant uncertainty component entering the measurement of angle of attack.

One additional test was used to check the consistency of the measurements and to ensure that the project-mean vertical wind would be near zero for research-flight conditions. All flights that appeared to provide good data for the calibration procedure were combined into one dataset. The excluded flights were 6 and 7 (where there were problems with plugged lines in the radome), and 15 (the calibration flight, mostly at lower than research flight altitude). Also, the period from 9:50 to 10:30 UTC on flight 23 was excluded because the radome measurements looked suspicious and might have been affected by blockage. Pitch corrections as discussed in the preceding section were applied to these flights, and then the following tests were used to exclude periods not significant for the calibration: a) measurements where the true airspeed was less than 130 m/s, to exclude periods of anomalously high angle-of-attack, esp. during takeoff and landing when flaps and/or landing gear might be deployed; (b) periods when the roll angle was less than -5 or more than $+5^\circ$, to exclude turns; and (c) periods of flight below 35,000 ft pressure altitude, to emphasize the altitudes most used during research flights. More than 400,000 measurements were available for the fit after these exclusions.

```
## lm(formula = AOAREF ~ AR, data = DataC)
## [1] "Coefficients:"
##              Estimate Std. Error t value Pr(>|t|)
## (Intercept)  4.435   0.001014   4373      0
## AR          21.166   0.013268   1595      0
## [1] "Residual standard error: 0.115, dof=439552"
## [1] "R-squared 0.853"
```

The result was fit coefficients 4.435 and 21.166. These coefficients are similar to those determined for the subset data used previously, but they could be used instead if the goal is to

minimize the offsets in mean vertical wind for the project because, for the constraints used, they will force a project-mean vertical wind of 0. A test of these coefficients for the segment of flight 12 away from the influence of South Island indeed led to a mean wind very close to zero, and flight-by-flight averages also are reasonably small with these coefficients.

4.1.3 Application to the gust pod

A similar approach was taken for the gust pod, but with variables translated to apply to the gust-pod instead of the radome: $\Delta P_\alpha = \text{ADIF_GP}$, $q = \text{QC_GP}$, $p = \text{PS_GP}$, and the Mach number M was that determined from the uncorrected measurements p and q from the gust pod. Apparently because of the under-wing location in disturbed airflow, a fit involving more terms was needed to represent the reference measurements from Eq. 34. After exploration of various possible terms, the fit selected to represent the gust-pod was the following:

$$\alpha = b_0 + \frac{\Delta p_\alpha}{q} (b_1 + b_2 M) + b_3 \frac{q}{p} \quad (38)$$

```
## lm(formula = AOAREF_GP ~ AQR_GP + AQRM_GP + RR2_GP, data = Data2)
## [1] "Coefficients:"
##               Estimate Std. Error t value
## (Intercept) -0.9033   0.007859 -114.94
## AQR_GP       3.6025   0.068942   52.25
## AQRM_GP      4.2860   0.137571   31.16
## RR2_GP       1.3299   0.033658   39.51
##               Pr(>|t|)
## (Intercept) 0.000e+00
## AQR_GP      0.000e+00
## AQRM_GP     1.128e-173
## RR2_GP      4.153e-252
## [1] "Residual standard error: 0.099, dof=1975"
## [1] "R-squared 0.989"
```

The results of this formula are compared to the reference data in Fig. 21. The best-fit coefficients were $\{b_i\} = \{-0.903, 3.602, 4.286, 1.330\}$ and the square of the correlation was 0.989 with residual scatter (residual standard error) of 0.099. The fit was thus even better than that obtained for the radome for these same speed runs.

As for the radome, an all-project fit was obtained for the gust pod. In this case, different flights were excluded: 2, 3, 4, 11, 15, 17, 18, 19, 23, 24, 25 and the flight period from 8:05–8:40UTC on flight 1. In most cases, this was because the CMIGITS IRU providing gust-pod measurements of pitch seemed to have larger than normal deviations that appeared suspicious, so it was thought preferable to fit without those periods of suspicious measurements. The fit summary is as follows:

```
## lm(formula = AOAREF_GP ~ AQR_GP + AQRM_GP + RR_GP, data = DataC)
## [1] "Coefficients:"
##               Estimate Std. Error t value Pr(>|t|)
## (Intercept) -0.8083   0.002366 -341.7      0
```

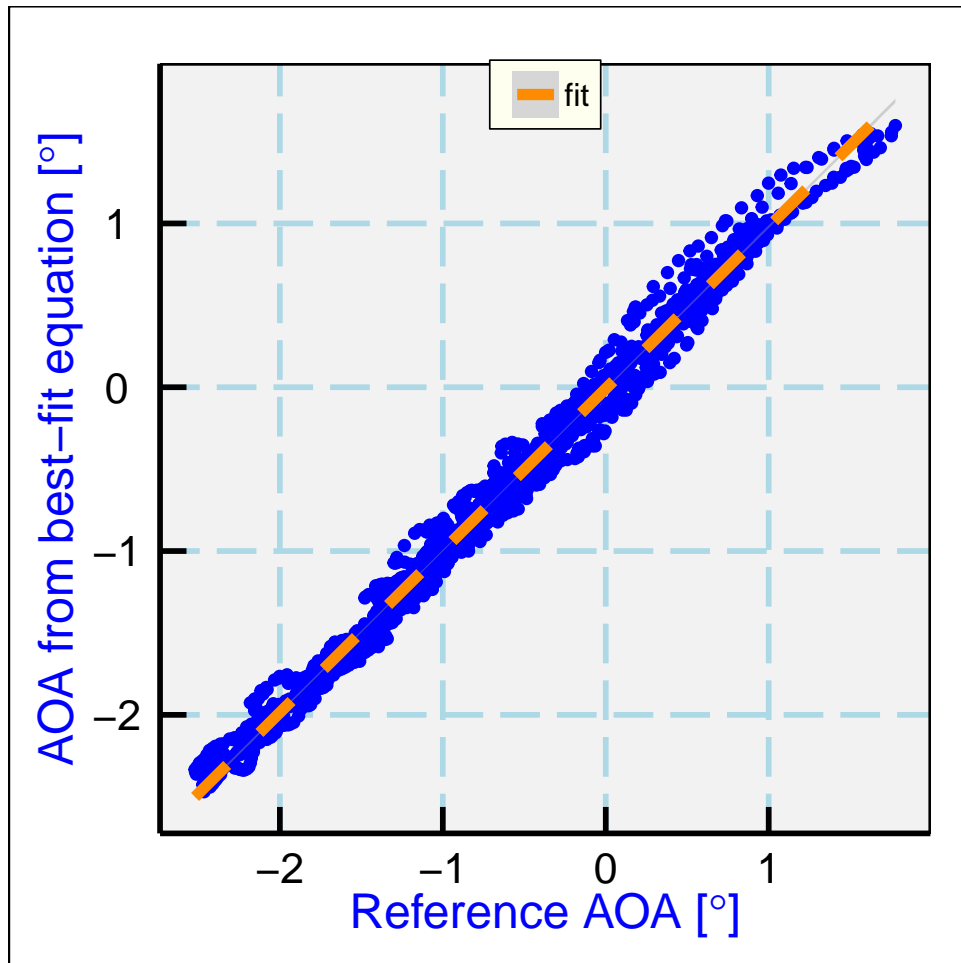


Figure 21: For the gust pod, the angle-of-attack determined from the fit as a function of the reference angle provided by (34), for the combined four speed runs. Compare to Fig. 18, the corresponding plot for the radome.

```

## AQR_GP      3.2478   0.030399  106.8      0
## AQRM_GP     5.3507   0.049025  109.1      0
## RR_GP       1.2820   0.007171  178.8      0
## [1] "Residual standard error: 0.163, dof=315554"
## [1] "R-squared 0.861"

```

These coefficients $\{-0.808, 3.248, 5.351, 1.282\}$ may be preferable to the coefficients obtained above if it is desirable to minimize the all-project mean vertical wind for the gust-pod measurements.

4.2 Sideslip Angle

4.2.1 Equations underlying the calibration

Calibration of the sideslip angle is more difficult, both because the equations are more complicated and because the maneuver is very hard to fly. Ideally, the sideslip maneuver should only change yaw angle and heading without change in roll, altitude, or angle-of-attack, but that is impossible to fly. It is practical, however, to minimize roll and change in altitude, and that was how these maneuvers were flown. The three sets of yaw maneuvers were at these times: 3:32:00–3:35:30, 4:31:00–4:33:30, and 5:26:40–5:29:30 UTC.¹¹ In the case of yaw maneuvers, the calibration is based on the expectation that the horizontal wind remains constant. The first-order equations for the east and north components of the wind, u and v , are:

$$\begin{aligned} u &= -U_a \sin(\Psi + \beta) + u_p \\ v &= -U_a \cos(\Psi + \beta) + v_p \end{aligned} \quad (39)$$

where U_a is the true airspeed, Ψ the heading, β the sideslip angle, and u_p and v_p are the eastward and northward ground-speed components of the aircraft. These two equations lead to the following reference formula for β :

$$\beta^* = -\Psi + \arctan\left(\frac{u_p - u}{v_p - v}\right) \quad (40)$$

where the second term represents a correction for the change in direction of motion of the aircraft, which is difficult to avoid in the yaw maneuver. The measurements thus provide β^* , an estimate of the sideslip during the yaw maneuvers.

There is, however, a circular component in (40) because it involves the wind components and those require β for their measurement when sideslip changes. To reduce the feedback from this term, the horizontal wind components u and v were low-pass-filtered with periods ranging from

¹¹Because the yaw maneuvers on rf11 (10:25:00 to 10:30:00) were flown less well, they were not combined with these new measurements, but it does not appear that the sideslip calibration has any significant dependence on altitude.

5–60 s and the filtered values were used in (40). Filtering made small differences in the fit coefficients but increased the residual error significantly, but 60-s filtering was still selected because that is a period long in comparison to the yaw maneuvers so it should reduce possible bias in the fit coefficients from use of the older sensitivity coefficients and any associated fluctuations in the wind measurements during maneuvers.

4.2.2 Application to the radome-based and gust-pod systems

For both systems, a relatively simple fit was sufficient, in the following form:

$$\beta = e_0 + e_1 \frac{\Delta p_\beta}{q} \quad (41)$$

where Δp_β is the pressure difference between horizontally separated pressure ports and q the dynamic pressure. For the radome, $q = \text{QCF}$ and $\Delta p_\beta = \text{BDIFR}$; for the gust-pod, $q = \text{QC_GP}$ and $\Delta p_\beta = \text{BDIF_GP}$. The resulting fit for the radome is listed below:

```
## lm(formula = SSREF ~ BQR, data = DataV)
## [1] "Coefficients:"
##              Estimate Std. Error t value
## (Intercept)  0.09187   0.005428 16.92
## BQR         22.30224   0.170344 130.92
##             Pr(>|t|)
## (Intercept) 7.164e-50
## BQR          0.000e+00
## [1] "Residual standard error: 0.114, dof=441"
## [1] "R-squared 0.975"
```

The best-fit coefficients were $\{e\} = \{0.092, 22.302\}$, the squared correlation was 0.97 and the residual standard error was 0.11, as listed above. The plotted measurements and this fit are shown in Fig. 22. The sideslip offset that is represented by this term will be determined later by other means; cf. Section 6.1.5.)

The standard calibration in use for the GV has coefficient $e_1=21.155$, so this fit has slope about 5% greater than the standard values. These maneuvers were flown with special care to minimize altitude and roll changes, so this value may be preferable to the older values. The standard error of the fit, about 0.1° , is likely much larger than the error in representing the values of sideslip via (41) because much of the variability likely arises from real fluctuations in the horizontal wind, which would contribute this magnitude error for wind fluctuations of only about 0.4 m/s. The respective uncertainties in the fit coefficients were about 0.005 and 0.17° , the former leading to a possible bias error and the latter to an error of $0.17/22.3$ or less than 1% in the value of the sideslip. Measurements of sideslip are seldom larger than 0.2° , so a fractional error of 1% is not significant and will be neglected here. The bias in sideslip is intertwined with possible bias in heading, so further study of this offset will be deferred to Section 6.1.5 where it will be determined by a better method that separates it from the offset in heading.

For the gust-pod, the same approach was followed, giving a fit with characteristics as listed below:

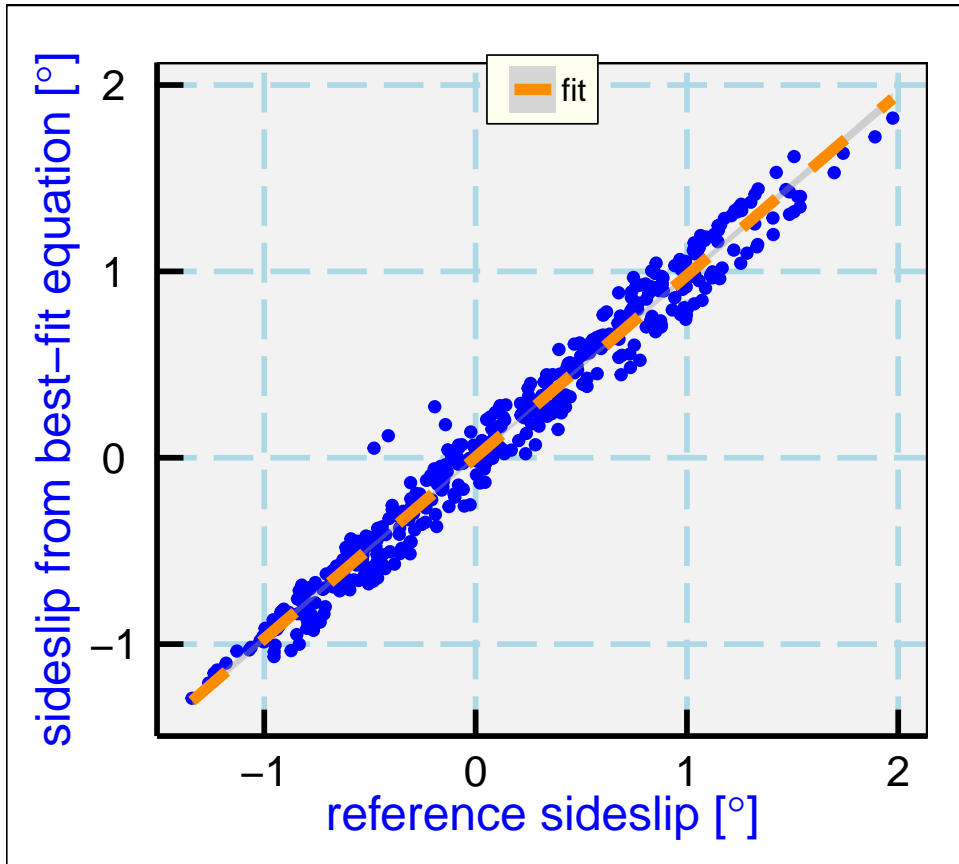


Figure 22: The sideslip attack determined from the fit, as a function of the reference angle provided by Equation (40), for the combination of data from all three yaw maneuvers listed in the text. The gray area underlying the dashed orange line denotes the standard-uncertainty range for the fit.

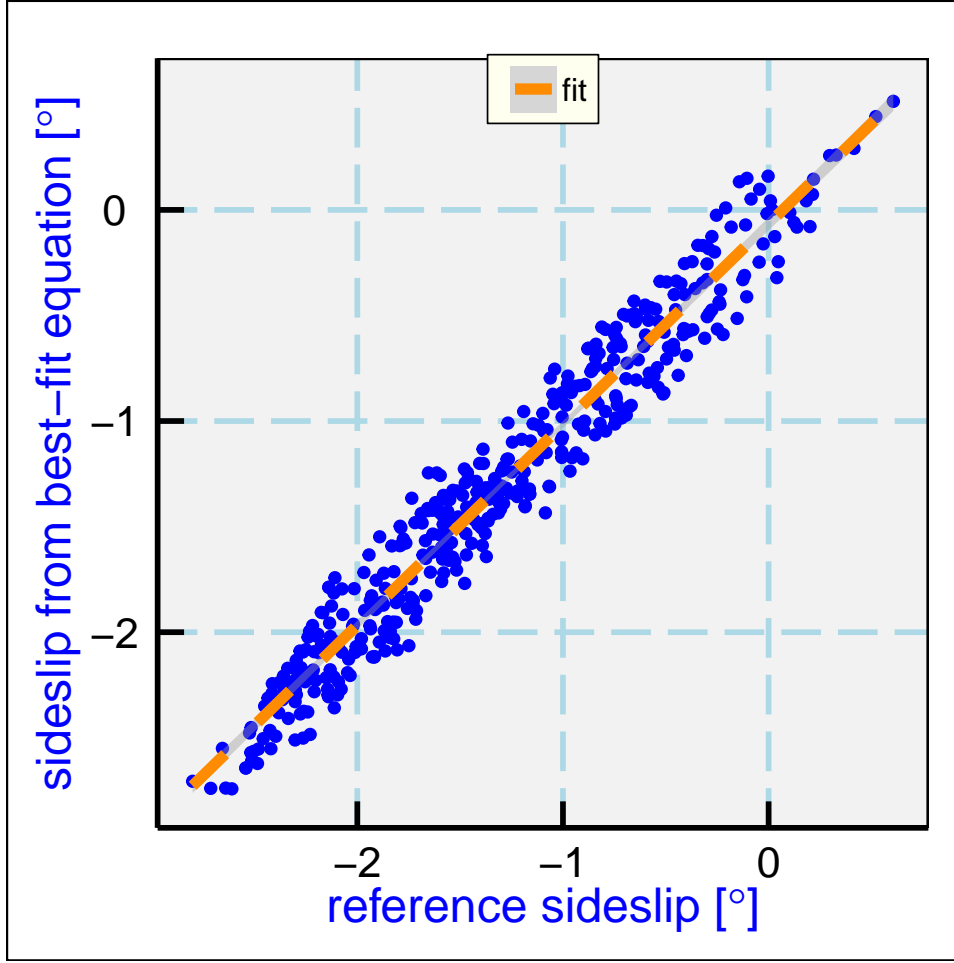


Figure 23: As in the preceding figure but for the gust-pod system.

```
## lm(formula = SSREF_GP ~ BQR_GP, data = DataV)
## [1] "Coefficients:"
##              Estimate Std. Error t value Pr(>|t|)
## (Intercept) -3.621     0.02624 -138.0  0.0e+00
## BQR_GP       12.184    0.13287   91.7 2.5e-289
## [1] "Residual standard error: 0.164, dof=441"
## [1] "R-squared 0.950"
```

The squared correlation of this fit was 0.95 and the residual standard error was 0.164° . The best-fit coefficients were $\{-3.621, 12.184\}$. The difference in first coefficient vs the radome is a result of the offset in heading between the aircraft longitudinal axis and the gust pod. The detailed report for the fit is listed above, and the result of applying these sensitivity coefficients to the measurements from the gust pod is shown in Fig. 23.

An additional study is needed to separate a possible offset in sideslip from a similar error in heading, because the approach used here assumes that the heading is accurate. In the data files used for this study, an offset in heading of -0.08° was imposed; without that offset, the offset in sideslip (coefficient e_0) would be reduced by 0.08. A method of determining these separate

offsets is developed later in this report (Section 6.1), where a set of circles flown with constant roll angle are used to obtain a better estimate of the sideslip offset. That study results in a corrected value for e_0 .

XXX

4.3 True Airspeed from the Gust Pod

The measurements ADIF_GP and BDIF_GP, normalized by QC_GP, are used with the calibrations in the preceding section to find the angle-of-attack and sideslip. In addition, to find the relative wind, a measurement of true airspeed (TAS) is needed. In an effort to allow the gust-pod system to operate independently of the standard radome-based system, it is desirable to determine the true airspeed directly from the gust-pod measurements. However, the standard system has been calibrated to low uncertainty by reference to the Laser Air Motion Sensor, so for the purpose of calibration that true airspeed (TASX) will be used as a reference. Once the gust-pod measurement of true airspeed is calibrated, the gust-pod system still measures wind without future reference to the standard system, but the calibration process links the two systems to have a common reference for TAS.

Therefore, the next step needed to use the gust pod wind-sensing system is to determine a functional relationship between gust-pod measurements and the true airspeed. The approach taken is to fit the basic pressure ratio q/p as measured by the 858 probe to match the corresponding pressure ratio provided by the conventional measurements of dynamic and static pressure. The relationship represents the true ratio of dynamic to static pressure, so using that ratio the normal calculation of true airspeed can be used to determine the TAS measured by the gust pod. For this purpose, all the measurements from the calibration flight (RF15) were used qualified only by requiring TASX>130 m/s.

The measurements entering the resulting fit are as follows: $q = \text{QCXC}$ is the reference dynamic pressure, $p = \text{PSXC}$ is the reference ambient pressure, $q_g = \text{QC_GP}$ is the gust-pod dynamic pressure, $p_g = \text{PS_GP}$ is the gust-pod static pressure, M is the Mach number determined from the reference measurements, M_g the Mach number determined from the gust-pod static and dynamic pressure, and $\Delta p_{\alpha,g} = \text{ADIF_GP}$ is the pressure difference between top and bottom pressure ports on the gust-pod sensor. The following equation was found to provide a useful representation of the reference ratio q/p in terms of quantities measured only by the gust-probe system:

$$\frac{q}{p} = b_0 + b_1 \frac{q_g}{p_g} + b_2 M_G \frac{q_g}{p_g} + b_3 \left(\frac{q_g}{p_g} \right)^2 + b_4 \frac{\Delta p_{\alpha,g}}{q_g} + b_5 M_G + b_6 \left(\frac{\Delta p_{\alpha,g}}{q_g} \right)^2 + b_7 \frac{\Delta p_{\alpha,g}}{q_g} M_G \quad (42)$$

This complexity in the equation was needed to obtain a good fit (with residual error translating to a typical error in true airspeed of about 0.5 m/s for typical DEEPWAVE research legs), and all terms were indicated to be significant in the fit. The fit details are listed below:

```
## lm(formula = B1 ~ B2 + BxM + I(B2^2) + AQR_GP + MachG + I(AQR_GP^2) +
##      I(MachG * AQR_GP), data = DataV)
## [1] "Coefficients:"
```

```

##               Estimate Std. Error t value
## (Intercept)    1.1940   0.031653 37.72
## B2             27.2893   0.844564 32.31
## BxM            -29.0483   0.965719 -30.08
## I(B2^2)         13.6231   0.411740 33.09
## AQR_GP          -0.5936   0.004224 -140.54
## MachG           -7.5812   0.226389 -33.49
## I(AQR_GP^2)     0.1554   0.002811 55.27
## I(MachG * AQR_GP) 1.2607   0.007205 174.97
##                  Pr(>|t|)
## (Intercept)      3.365e-305
## B2              1.114e-225
## BxM             3.094e-196
## I(B2^2)          2.311e-236
## AQR_GP           0.000e+00
## MachG            5.543e-242
## I(AQR_GP^2)      0.000e+00
## I(MachG * AQR_GP) 0.000e+00
## [1] "Residual standard error: 0.002, dof=34524"
## [1] "R-squared 0.998"

```

The resulting fit is shown in Fig. 24. With this result for G^* from (42), the true airspeed can then be obtained using the usual formula, with G^* used in place of q/p :

$$V = \sqrt{2 \left(\frac{(c_p - R_a)}{R_a} \right) (1 + G^*)^{\frac{R_a}{c_p} - 1} \left(\frac{c_p}{c_v} R_a T \right)} \quad (43)$$

where c_p , c_v , and R_a are the specific heat of air at constant pressure, the specific heat of air at constant volume, and the gas constant for air and p is the static pressure, q the dynamic pressure, and T the absolute temperature.

The resulting true airspeed is compared to the conventional measurement in Fig. 25. The fit provides a reasonable representation of TASX, with a standard error of about 0.4 m/s. This is not much larger than the estimated uncertainty in TASX (about 0.3 m/s), so wind calculations might be based on this value if necessary. However, there is serious danger of over-fitting with this many coefficients and variables, even though the fit was improved significantly with each addition; indeed, the standard error in the q/p fit was reduced by 50% with the addition of the last two variables in the fit. Because of the danger that this variable might not perform as well when used outside the range of this fit (which was $\text{TASX} > 130$, $|\text{ROLL}| < 5$, and $\text{GGALT} > 5000$), it still should be better to base wind measurements from the gust pod on the conventional TASX combined with the relative-wind angles from the gust pod. However, if it is desirable to have a wind measurement that is completely independent of the standard radome-based system, using true airspeed measured with this fit might provide a useful alternative.

In particular, for the DEEPWAVE flights where the standard vertical wind measurement was compromised by an obstruction in the pressure-sensor lines of the radome, the best vertical

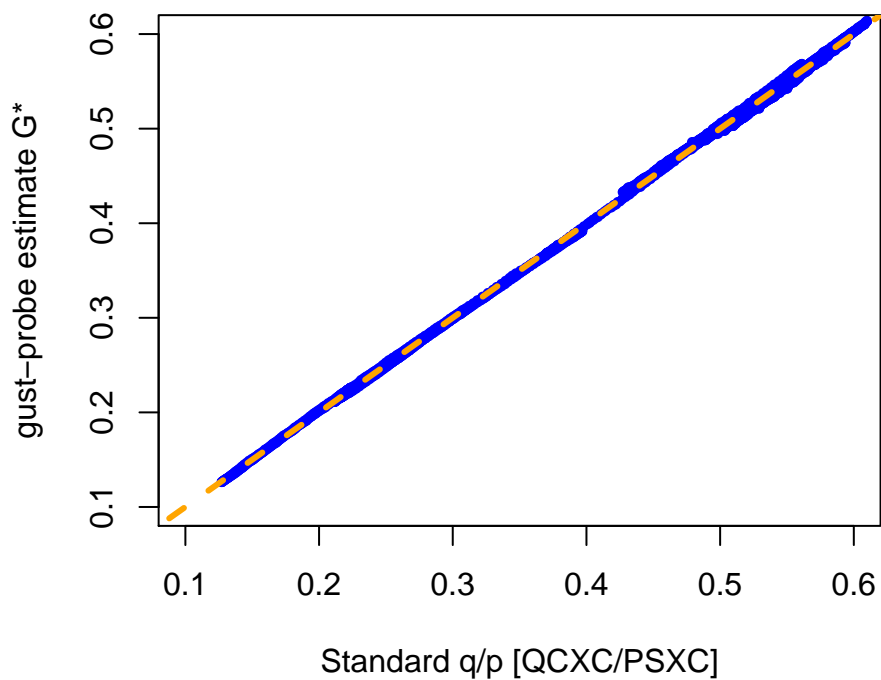


Figure 24: The estimate of q/p obtained from the right side of (42), determined entirely from measurements provided by the gust pod, plotted against the standard measurement obtained from QCXC/PSXC. The coefficients are listed in the text.

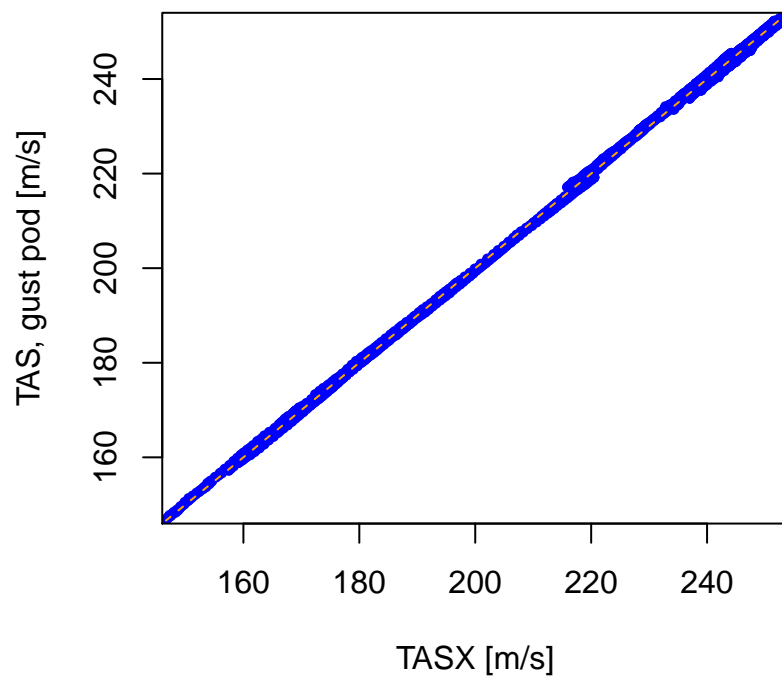


Figure 25: True airspeed obtained from the gust pod, plotted against corresponding measurements from the conventional measurement system (TASX)

wind will be that calculated using (38) for the angle of attack but conventional TASX for the true airspeed, because the pressure ports used to determine TASX were not obstructed.

4.4 Summary of sensitivity coefficients

4.4.1 Angle of Attack

Radome: Eq. (37), coefficients $c_{0,1} = \{4.468, 21.481\}$.¹²

Gust pod: Eq. (38), coefficients $\{b_{i=0,3}\} = \{-0.903, 3.602, 4.286, 1.330\}$ ¹³

4.4.2 Sideslip Angle

Radome and gust pod: Eq. (41), coefficients $\{e_0, e_1\} =$

$\{0.092, 22.302\}$ for the radome,¹⁴

$\{-3.621, 12.184\}$ for the gust pod.

4.4.3 True Airspeed, Gust Pod

Equation (43), with (42) and coefficients $\{b_{i=0,7}\} =$

$\{1.194, 27.2893, -29.0483, 13.6231, -0.5936, -7.5812, 0.1554, 1.2607\}$.

¹²See also the alternative coefficients $\{4.435, 21.166\}$ discussed on page 68.

¹³See also the alternative coefficients $\{-0.808, 3.248, 5.351, 1.282\}$ discussed on page 69.

¹⁴However, see the revision of the first coefficient that follows in Section 6. The value listed in the concluding summary of that section, in Section 6.1.6, should supersede the value listed here.

5 Studies of the Vertical Wind

5.1 Overview

The preceding sections provided extensive information on how vertical wind is measured and how the radome-based system is calibrated. Here, three additional topics not covered well there are discussed to complement those earlier discussions. The sections here deal with the choice and quality of the variable characterizing the vertical motion of the aircraft, some issues related to the relative timing of the measurements entering the calculation of vertical wind, and a proposed method for using detection of the Schuler oscillation of the IRU to correct the measurement of pitch.

5.2 The vertical velocity of the aircraft

5.2.1 Available measurements

There are several independent measurements of the vertical motion of the aircraft:

Variable	Source
VSPD	Honeywell IRU
VSPD_A	Avionics system (Honeywell IRU)
GGVSPD	GPS receiver, possibly with OmniSTAR corrections
CVSPD_GP	CMIGITS IRU, gust pod
CVSPD_LAMS	CMIGITS IRU, LAMS pod

The standard vertical wind calculation depends on a measurement of vertical motion of the aircraft. Past projects have used one of VSPD (from the IRU), VSPD_A, VSPD_G or GGVSPD (from GPS, the first two alternate names for the value provided by the avionics package) or, much earlier, WP3 from a baro-inertial update loop using VSPD. Baro-inertial updating is no longer used because the Honeywell IRU that now provides VSPD already incorporates such updating. For the systems based on the gust pod or LAMS, additional vertical-velocity measurements are provided by their pod-mounted IRUs, respectively CVSPD_GP and CVSPD_LAMS. Changing roll of the aircraft can cause these measurements to differ from the fuselage-based measurements.

Because VSPD as provided by the Honeywell IRU is controlled against the known instability of IRU measurements in the vertical by updating to a reference value provided by pressure altitude, it has some drawbacks. Pressure altitude is not really a measure of altitude but of pressure, so the reference altitude can be biased. Also, the IRU-imposed baro-inertial loop has unknown response characteristics and uncertainty, and the value provided by the IRU has inherent filtering. The advantage of an IRU variable over a GPS measurement has been, until recently, better response at high frequency at the expense of absolute accuracy. GPS measurements have now improved, esp. with OmniSTAR, so it is worth considering what variable or combination of variables should be used in the calculation of vertical wind.

For horizontal wind, the standard solution in use since the early 1990s has been a complementary-filter solution (discussed in Sect. 6.2, where the difference between IRU and GPS measurements is low-pass filtered and the result is added to the IRU measurement. This preserves the high-frequency response of the IRU measurement but causes the low-frequency components to match the GPS measurements, thus providing both absolute accuracy and valid high-frequency measurements. It seems worthwhile to explore a similar approach for the vertical wind, to see if there is an advantage to a variable that is provided by an analogous complementary filter.

Some of the following refers to a variable GGVSPDB, a highest-resolution version of GGVSPD. GGVSPDB was used in this evaluation to ensure that the reduced resolution in GGVSPD did not influence the variance spectra, but GGVSPD is the usual variable used in wind calculation. It has sufficient resolution for that purpose, and there appears to be no advantage to using the higher-resolution variable.

In standard processing, two vertical-wind variables are produced from the radome-based system, WI and WIC. These are called, respectively, “Wind Vector, Vertical Gust Component” and “GPS-Corrected Wind Vector, Vertical Gust Component”. They are calculated by adding the relative wind measured by the radome system to the vertical motion of the aircraft, either VSPD (WI) or GGVSPD (WIC). The former is directly from the Honeywell IRU; the latter is produced by the GPS receiver and may benefit from OmniSTAR accuracy (flagged by GGQUAL equal to 5).

The names are not really appropriate and should be changed, but they appear in many past datasets. Neither is the gust component; both are the full vertical wind including relative wind and aircraft motion. Also, WIC is not GPS-corrected, it is completely based on the GPS and does not use the IRU at all except for the attitude angles need to determine the relative wind (the same for both). These calculations employ the nimbus function “gust”, which implements the algorithm described in Sect. 2.1.

In addition, the Honeywell IRU provides a measurement of vertical acceleration. In a special calculation, this was integrated to get velocity and the result compared to VSPD. The results of the integration and the variance spectrum of that result were quite similar to VSPD, provided that a feedback loop was used to avoid exponentially growing errors from positive feedback, so there is no advantage to using that integrated acceleration in place of VSPD. (It was hoped that some of the filtering imposed on VSPD could be avoided.)

5.2.2 Variance spectra for components affecting the vertical wind

For evaluation of these measurements of aircraft velocity, it is useful to compare the variance spectra among them and to evaluate the contribution made to the vertical wind. For this purpose, one flight from DEEPWAVE, RF16 (4 July 2014) was used because it provided a good example of relatively intense and prolonged vertical motion, with the core 6 h period of the flight from 6:30:00 – 12:30:00 having a standard deviation in vertical wind of 1.0 m/s. Much of the variation in vertical wind was from waves, so the field was not fully developed turbulence, but the signals to be resolved had enough intensity that noise floors on the measurements were not a problem.

Figure 26 shows variance spectra calculated for the entire 6-h period, for a number of mea-

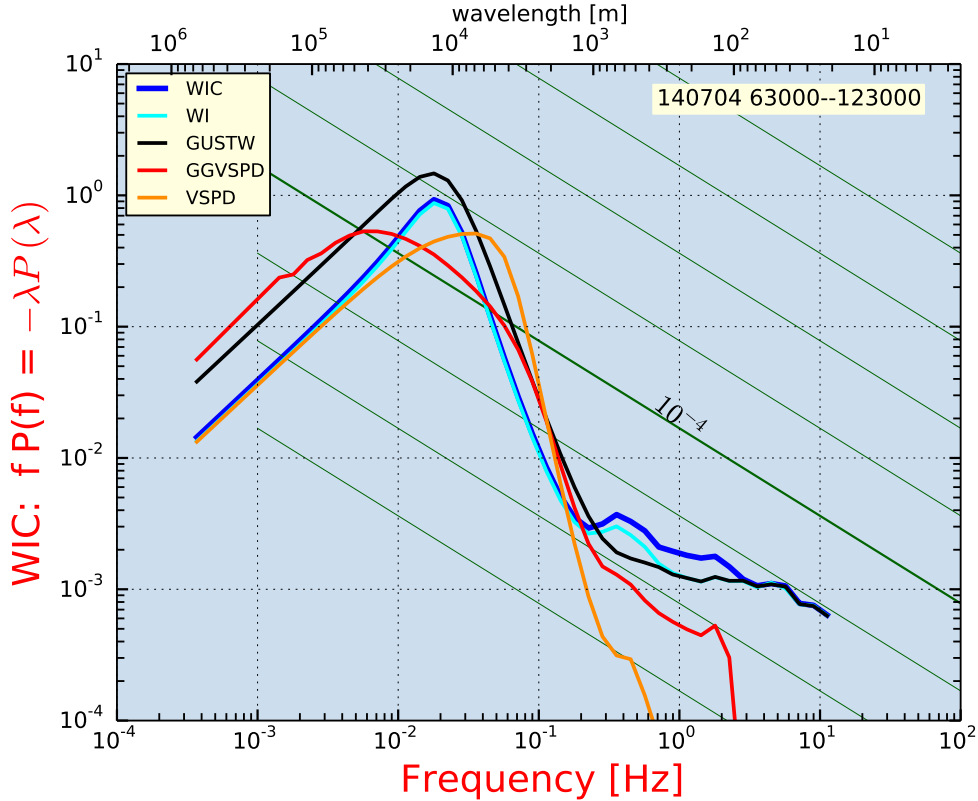


Figure 26: Variance spectra [units: m^2s^{-2} , density functions per logarithmic interval in frequency expressed in Hz] for various components entering vertical-wind calculations. Data are from DEEPWAVE flight 16, 6:30:00–12:30:00 UTC. The thick blue trace is that for the vertical wind variable WIC; others show either measurements of the aircraft vertical motion (VSPD, GGVSPD) or, as GUSTW, the relative-wind contribution to WIC. The green diagonal lines show the slope expected for an inertial subrange; the thicker green line labeled “ $!10^{-4}$ ” corresponds to the spectrum expected for an eddy dissipation rate of $1 \times 10^{-4} \text{ m}^2\text{s}^{-3}$. Other green reference lines are displaced by an order of magnitude in eddy dissipation rate. The calculations are based on the all-poles or maximum-entropy method, with 100 poles; cf. [Press et al. \[1992\]](#). The resolution used was 0.0005, with results smoothed in 50 bins in the logarithm of frequency. Total variance is $1.36 \text{ m}^2\text{s}^{-2}$.

surements entering the vertical-wind calculations.¹⁵ The thick blue trace shows the spectrum for the standard vertical wind measurement WIC, which has a pronounced broad peak near 10 km wavelength, a relatively small inertial subrange extending only to about 2 km, and (after smoothing in 50 logarithmic intervals across the range of the plot) uncertainty estimates that range from about 5% at the lowest frequencies to <1% at the highest frequencies.

The two measures of vertical aircraft motion, GGVSPD (from the GPS receiver) and VSPD (from the inertial reference unit), have important differences in their properties. At high frequency, VSPD (orange line) decreases rapidly with increasing frequency, so it makes negligible contribution to the vertical wind (WI) at frequencies above 1 Hz. In contrast, GGVSPD (red line) does not show a similar steep drop in variance until after about 2 Hz, and it continues to make an important contribution to WIC over the frequency range from about 0.3 to 3 Hz. The absence of spectral variance above about 0.3 Hz in VSPD appears to be the result of internal filtering of this signal in the inertial unit, and indeed some limited information on the properties of the signals does indicate filtering at about this frequency. Because the aircraft motion clearly has components in this frequency range (based on the feel of the ride in turbulence), it appears that WI should not be used for frequencies above about 0.3 Hz.

The inertial-system variable VSPD is also subject to pressure damping, and this may account for the difference between GGVSPD and VSPD at long wavelength. The aircraft normally flies with reference to the pressure altitude, so in a region of varying altitude at a given pressure there are fluctuations in the aircraft geometric altitude (red line) not reflected in the pressure altitude (orange line). Both contribute in ways that result in essentially the same spectral variance for frequencies below 0.3 Hz, as shown by the near coincidence of the blue and cyan lines, so the difference is not significant. Here also, though, the red line representing the GPS measurement is a better measure of how the vertical wind should be affected, because the pressure-damped orange line will not show real vertical motion of the aircraft as it remains on a pressure surface.

For these reasons, WIC is the preferable variable to use for vertical wind. This also answers the question posed earlier regarding the possibility of using a combination of measurements from inertial and GPS systems to obtain better frequency response. The IRU measurements turn out to have poorer frequency response and lead to apparent biases for frequencies around 1 Hz, so this is not a useful combination. Instead, it appears best to use the GPS-provided measurement of vertical aircraft speed directly without further modification.

There is still some reason for concern about the spectral response of GGVSPD at frequencies around 0.5–1 Hz, because there is no evidence that the GPS is providing valid response at this high rate. The unit used provides measurements at 5 Hz and these measurements are interpolated and filtered to higher frequency, so the cut-off apparent in Fig. 26 is a result of that sampling and may remove a real signal at higher frequency. This topic will be reconsidered in the next section when variance spectra for the horizontal wind are examined.

The black trace (labeled GUSTW) is the vertical component of the relative wind, calculated as in Sect. 2.1.2. The sum of GUSTW and GGVSPD determines WIC, and the alternate measure of vertical wind WI is the sum of GUSTW and VSPD from the inertial reference unit. GUSTW

¹⁵This plot is an exception to the goals of "reproducible analysis" explained in the introduction and Appendix B. The calculations used an external spectral-analysis program, not R code, and the specific data are not part of the data archive for the document.

has higher spectral variance than WIC for frequencies below 0.3 Hz, so at these frequencies the aircraft motion tends to counter the relative wind and reduce the measured variance. This would be the case, for example, if there were negligible vertical wind and the relative wind arose entirely from the vertical motion of the aircraft. On the other hand, for frequencies around about 0.5 Hz the spectral variance in the vertical wind exceeds that in the relative wind so the aircraft responds approximately in phase with the vertical gusts.

The high-frequency variance spectrum has a slope differing a small amount from the expected $-5/3$ spectrum, and that is cause for some concern, but the turbulence in this region was not very well developed or consistent so this is probably not cause for alarm. Very good agreement with expectations has been seen in cases of boundary-layer measurements where well-developed turbulence at small scales is expected, but in those cases the intensity of turbulence at small scales was greater also. This is reason to continue to be suspicious of the response around 0.5–1 Hz.

Some of the relative magnitudes shown in Fig. 26 may change for different intensities of turbulence. However, some tentative conclusions seem indicated by this figure and the discussion above:

1. Exclude the variable WI from future data archives. VSPD, on which WI is based, has problems at both high and low frequency. Providing this variable could lead to the mistaken expectation that this is the uncorrected version of WIC, while the two variables actually use different and independent measurements of the vertical motion of the aircraft. The argument for using a variable based on VSPD has been that this formerly represented the high-frequency contribution better than a GPS variable. That is not the case any longer, because GPS measurements have improved greatly and the presently available IRU-provided measurements are obviously filtered at high frequency.
2. VSPD does not have better frequency response than GGVSPDB at high frequency, as might be expected; the reverse is the case, possibly because of filters imposed on VSPD in the inertial unit itself. This argues for direct use of GGVSPDB in the vertical-wind calculation, at least when OmniSTAR corrections are available.
3. The relative-wind variance spectrum shows higher variance than does that of the vertical wind, indicating that the contribution from aircraft motion counters the relative-wind contribution at all but the highest frequencies. The variable GGVSPDB is close to 180° out-of-phase with the relative wind (GUSTW in Fig. 26) for frequencies smaller than 0.2 Hz. At low frequency, the motion of the aircraft probably produces more of the measured vertical component of the relative wind than does the real wind, while at intermediate frequency (near 0.1 Hz) the aircraft perhaps responds to the vertical wind so as to move out-of-phase with it, exaggerating the measured vertical component of the relative wind. There is a transition in phase from being above 180° to being below 180° as the frequency increases through 0.05 Hz, perhaps representing a transition from where the pilots or autopilot cause motions that produce the relative-wind vertical component to where the vertical wind causes the aircraft response.

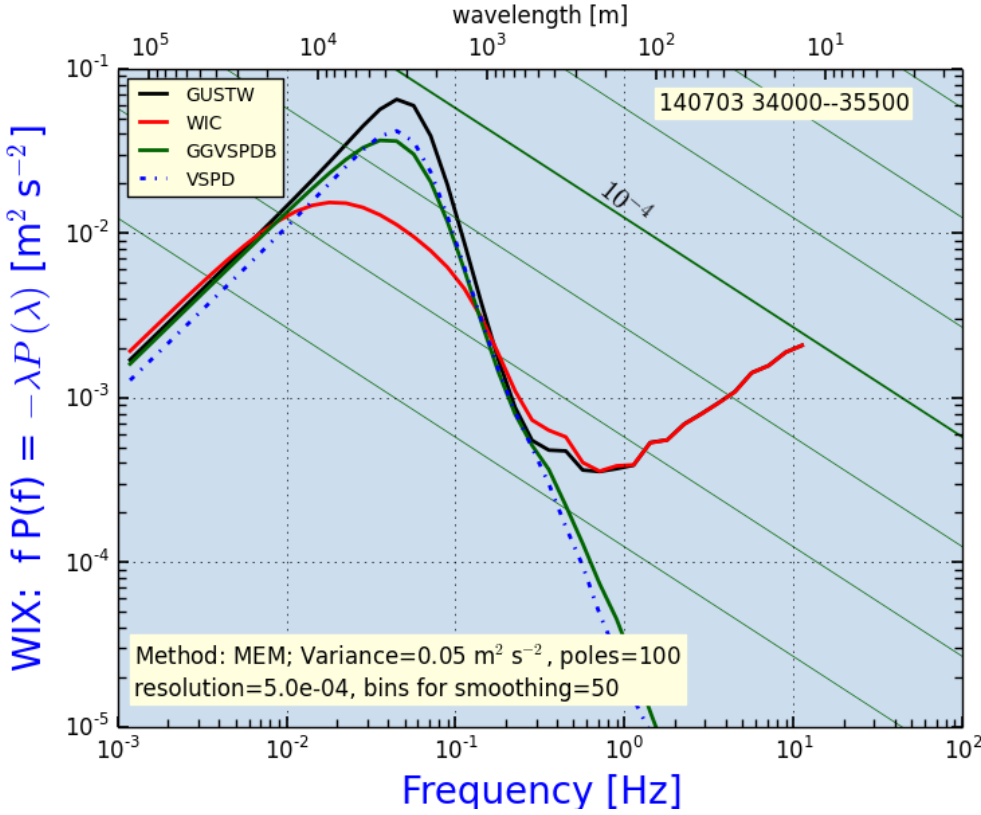


Figure 27: Variance spectra for the vertical wind (here, WIX) and for the contributions to it made by the relative wind (GUSTW) and the aircraft motion (GGVSPDB). Also shown for comparison is the spectrum for the IRU-provided aircraft motion (VSPD, dashed line). Data from DEEPWAVE flight 15, 3:40:00–3:55:00.

4. At high frequency (>0.3 Hz), the gust component dominates over the aircraft response, the coherence between them falls to values between 0.1–0.5, and the phase relationship becomes variable before settling near zero at 0.5 Hz.

An example where there was very low turbulence is shown in Fig. 27. The intensity of vertical-wind fluctuations was quite small for this flight segment, with a standard deviation in vertical wind of only about 0.2 m/s. Some features of this plot are explained below:

1. The measured vertical wind at high frequency (>1 Hz) is a white-noise spectrum with intensity that can be matched by generating a random-noise signal with peak amplitude of 0.15–0.2 m/s, which would lead to a random error of about $(0.15-0.2)/\sqrt{12} \approx 0.05$ m/s. The noise is dominated by the relative-wind contribution; there is essentially no contribution at these frequencies from the motion of the aircraft. The noise arises almost entirely from the angle-of-attack contribution to the relative wind, and specifically from the measurements “ADIFR” and “QCR”, which exhibit noise spectra for frequencies above 1 Hz. In ADIFR, the noise is at a level that would arise from a white-noise signal with peak amplitude of 0.4 hPa or a random error of about 0.1 hPa. Similar noise is present in both

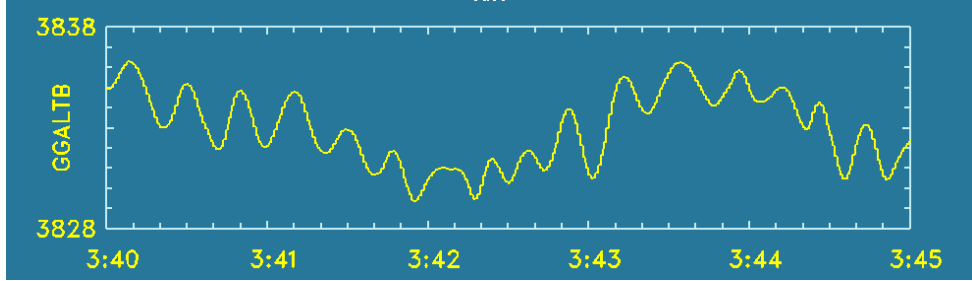


Figure 28: The GPS-measured altitude during a flight segment in very smooth air. Data from DEEPWAVE flight 15, variable GGALTB.

QCR and QCF, so it may be linked to the nature of the transducers used or to some effect originating in the pressure lines connecting the transducers to the ports. The specifications for the pressure transducer that measures ADIFR assert a standard uncertainty of about 0.03 hPa, and as sampled and digitized by the data system the resolution is about 0.002 hPa (± 70 hPa for 2^{16} range digital encoding). Thus the white-noise spectrum indicates a random error about three times greater than expected from the transducer characteristics. This needs further investigation because it imposes an important limit on capability to measure low-intensity turbulence.

2. The relative-wind contribution (GUSTW) and the aircraft-motion contribution (GGVSPDB) both have peaks at about 0.05 Hz, with canceling contributions so that no peak occurs at that frequency in the resulting vertical wind. This peak arises from the autopilot controlling the aircraft, which has a noticeable oscillation about the set altitude with a period of about 15–20 s. A regular oscillation with this period is quite evident in Fig. 28.
3. The disagreement between VSPD and GGVSPDB even at low frequency is another indication that the IRU-provided value (VSPD) should not be used, because the GPS-measured value at low frequency is surely a better measurement than is possible from the IRU. (OmniSTAR corrections were present throughout this flight.)
4. The difference between WIC and GUSTW near 0.3 Hz, seen also as a possible effect in Fig. 26, indicates that both the relative wind and the aircraft motion are making contributions that add at these frequencies. The spectrum of vertical wind here may be suspect because it is not clear if the amplitude of this contribution from the GPS measurements should be trusted at these frequencies. [XXX exploration of high-frequency GGVSPDB might be useful if such are available; they were not present in the 25-Hz file I used.]

5.3 Timing of measurements

The different measurements entering the calculation of vertical wind should be sampled at the same time. That is particularly difficult in the case of samples from the inertial reference system and GPS because they produce sample streams according to their own timing and not in response to requests from the aircraft data system. The variables involved in calculating the vertical wind are:

- Angle of attack, from transducers attached to radome ports via lines that can introduce small lags. No lag is currently used in processing.
- Pitch, from the IRU, transferred to the aircraft data system after some delay that must be removed in processing. The standard processing has a “delay” of -60 ms; i.e., the measurement is advanced in time by 80 ms so as to apply to a time later than when it is received. It is hard to understand how this is justified.
- Other attitude angles (heading and roll), which enter in minor ways if the aircraft is not flying a straight-and-level course. The timing of these can probably be neglected for calculations of vertical wind, but the standard variables are also given a time lag of -60 ms.
- True airspeed, measured using the pitot-tube measurement of dynamic pressure, used also with a measurement of temperature. While no lag is assumed for dynamic pressure, the reference total temperature for DEEPWAVE is RTHR1 (tentatively), and a time lag of -1 s is used for this measurement. (No lag is assumed for RTRL, another candidate for the reference temperature.)
- The vertical speed of the aircraft, taken for the preferred vertical wind variable from GGVSPDB, the variable produced by the Novatel GPS receiver employing OmniSTAR corrections when possible. This variable is only sampled at a rate of 5 Hz, and no time lag is used in processing.

It is useful to try to determine appropriate lags from the data and from appropriate maneuvers. For example, in pitch maneuvers (in which the pitch is alternately increased and decreased with typically a 10-s period) if the timing of measurements of pitch and angle-of-attack are not matched or if the measurement of vertical speed of the aircraft is not timed correctly there will be a residual measured vertical wind, so these maneuvers are particularly stringent tests of relative timing of the signals.

An approximate formula for the vertical wind w is

$$w = V \sin(\alpha - \theta) + w_p \quad (44)$$

where V is true airspeed, α is angle-of-attack, θ is pitch and w_p is the vertical velocity of the aircraft. This equation can be used to adjust relative timing among the signals to minimize the variance in vertical wind during the pitch maneuvers. A good example is that from DEEPWAVE flight 15, 3:15–3:18 UTC. As initially processed using standard processing at the time of DEEPWAVE, the standard deviation in vertical wind through the pitch maneuvers was 0.4 m/s while the variance in vertical motion of the aircraft was 5.6 m/s. A long-standing criterion for acceptable pitch maneuvers is for less than 10% of the imposed velocity to enter the vertical wind, so by this criterion the test was successful. However, a plot of the vertical wind shows a clear match to the imposed velocity, so it is worthwhile to see if better results are possible.

Speed runs have been used to determine the sensitivity coefficients for determining α from the measured pressure differences on the radome, so the sensitivity coefficients should not be

adjusted on the basis of the pitch maneuvers. The relative timing of the measurements entering Eq. 44, however, can be adjusted to determine if the residual vertical wind can be reduced. The sensors producing V and α are located close together and are processed in the standard manner by the data acquisition system, so these can be assumed to determine the reference time except for possible delays introduced by pressure lines. However, the other variables θ and w_p are determined by independent systems and may have timing offsets from the standard measurements, so these are the variables whose lags are explored here.

The approach was to shift the measurements forward or backward in time and, using Eq. 44, recalculate the vertical wind. The best result obtained in this way was to shift PITCH forward 0.04 s and shift GGVSPDB backward 0.04 s. Almost as good was to shift PITCH forward 0.08 s and shift GGVSPDB backward 0.04 s. This reset the assumed lag in PITCH to zero while imposing a small lag of -0.04 s in GGVSPDB. For the purpose of this study, to avoid the phase lag produced by filters at the high-frequency limit, Savitzky-Golay filtering was used for GGVSPDB with 4th-order polynomials applied over 25-measurement intervals to smooth the original measurements. The resulting standard deviation in WIX was 0.22 m/s, vs 0.23 with no shift in GGVSPDB, so it may be preferable to leave the assumed lag for GGVSPDB at zero to avoid the awkwardness of advancing the measurement in time.

With the assumed time lag in PITCH removed, the resulting measurement of vertical wind during the pitch maneuver is shown in Fig. 29. The standard deviation in measured wind through the pitch maneuvers is only 4% of the imposed vertical motion of the aircraft.

There is little signal corresponding to the imposed vertical motion or variations in pitch, and the measured standard deviation in vertical wind is about the same as that for measurements just before and just after the pitch maneuvers. It thus appears that the measuring system is able to remove the effects of the pitch maneuvers with essentially undetectable residual.

5.4 Correcting pitch for the Schuler oscillation

r

5.4.1 Basis for the correction

Before discussing additional aspects of the measurement system like determination of sensitivity coefficients for the radome, it is necessary to explain and document a correction that will be used in that determination and in subsequent studies. The normal primary weakness in measurement of vertical wind is the measurement of pitch, which is provided only by inertial reference systems and therefore has the uncertainty and fluctuations associated with those systems. An inertial system aligns during initialization to detect the local vertical direction and then calculates the new vertical direction as the aircraft moves (changing the local vertical direction) and accelerates (which can cause gyros to precess). Any misalignment present at initialization persists but also can oscillate and can cause errors in roll and pitch to mix as the aircraft changes flight direction. The standard error associated with this measurement is 0.05° for flight duration of a few hours, and the error often increases during the flight as heading errors and accelerometer biases affect the results.

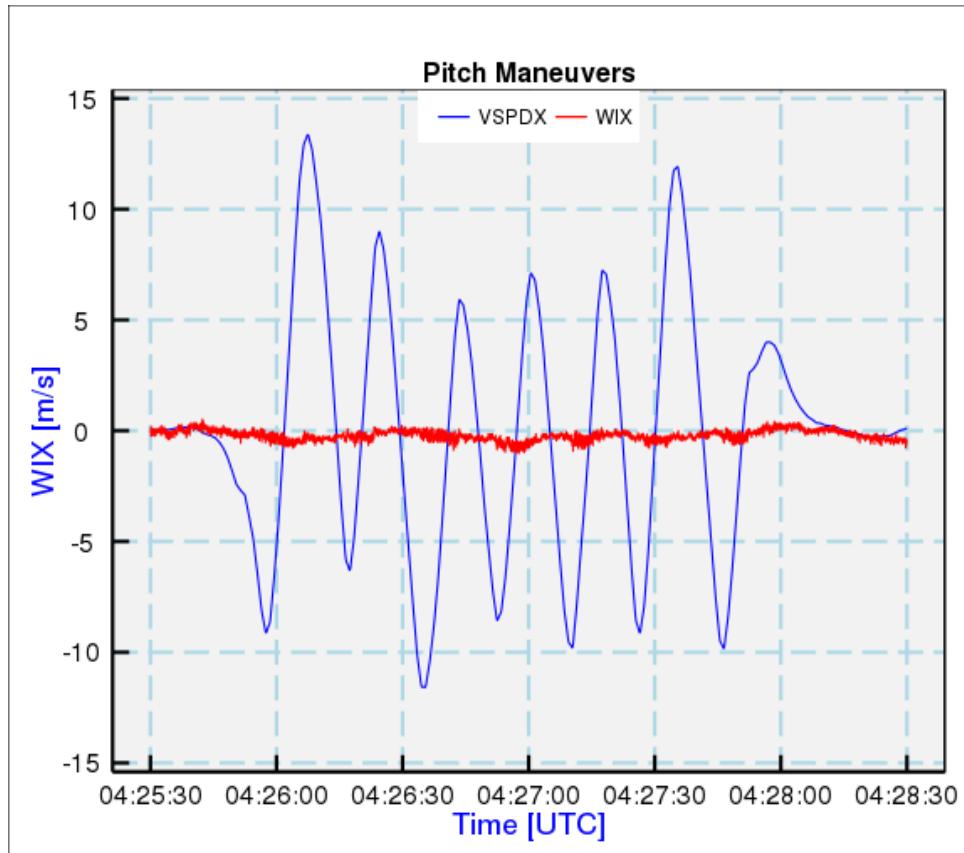


Figure 29: Vertical wind measured during pitch maneuvers. The variable VSPDX (which is GGVSPDB interpolated, filtered, and shifted) shows the vertical motion imposed on the aircraft, and WIX shows the resulting measurement of vertical wind.

Following the work of Schuler ([Schuler \[1923\]](#)), coupling among some of these error sources leads to limits on the growth of errors and simultaneous oscillations in some of the measurement errors. In particular, an error in pitch leads to an error in horizontal acceleration, and integration of that error in horizontal acceleration leads to a position error that compensates for the original error in pitch. However, when the error in pitch is reduced to zero, errors in position and velocity have been accumulated and those lead to growth of the error in pitch in the direction opposite to the original error. The result is a Schuler oscillation having a period of $T_{Sch} = (R_e/g)^{0.5}/(2\pi) \approx 5064\text{ s}$ or 84.4 min, where R_e is the radius of the Earth and g the acceleration of gravity. The existence of this coupling allows estimation of the pitch error if the error in horizontal acceleration is known. That is the case in DEEPWAVE because high-quality measurements of velocity are available from GPS and those measurements can be compared to the uncorrected measurements from the inertial systems to measure the error in velocity and, from its derivative, the error in acceleration. The specified uncertainty for the IRU, 0.05°, contributes an uncertainty in measured vertical wind of about 0.2 m/s, and it is shown later that this is the dominant contribution to uncertainty in that measurement, so improving on this can lead to significant reduction in the uncertainty associated with measurement of vertical wind.

5.4.2 Simple illustration of Schuler oscillation

Although the following is standard material, it is presented here to make the discussion of the Schuler oscillation self-contained and for tutorial purposes. Those familiar with the Schuler oscillation should skip this subsection.

Consider first the case of steady flight to the north. If, at some starting point at rest, there is a pitch error $\delta\theta$, that will cause gravity to be resolved into a NS component, as shown in this diagram where a pitch error of $\delta\theta$ produces an erroneous northward acceleration of $g \sin(\delta\theta) \simeq g\delta\theta$:

The result is that this erroneous acceleration produces a false northward velocity and, integrated, a northward error in position. However, the error then causes the integrated position to become too far north, where the calculated direction toward the center of the earth becomes biased in the opposite direction, and at some point the calculated offset from being too far north equals the pitch bias, as shown in the next figure:

However, at the point where the error in latitude cancels the error in pitch, there is an accumulated error in velocity, so the integrated solution for position overshoots the equilibrium position by an amount such that the error in pitch becomes the negative of the original error, at which point the integrated velocity is zero but the new error in pitch now causes a reversal of the position error. The result is that the errors in pitch, velocity and position all oscillate with a period equal to the Schuler period, $T_s \simeq 5064\text{ s}$, determined from $T = (R_e/g)^{0.5}/(2\pi)$.

Here are the equations predicting how this oscillation will occur:

$$v_n = \frac{dx_n}{dt} = R_e \frac{d\lambda}{dt} \quad (45)$$

$$\frac{d^2x_n}{dt^2} = a_n \quad (46)$$

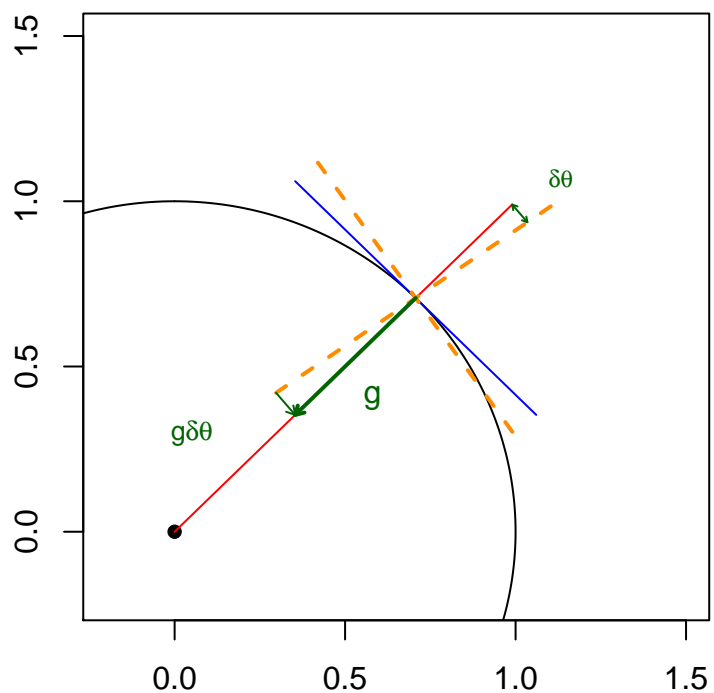


Figure 30: Illustration of how a pitch error of magnitude $\delta\Theta$ leads to a false measurement of horizontal acceleration of magnitude $g\delta\Theta$. The blue line represents the true level plane tangent to the surface of the Earth and g the magnitude and direction of the gravitational acceleration.

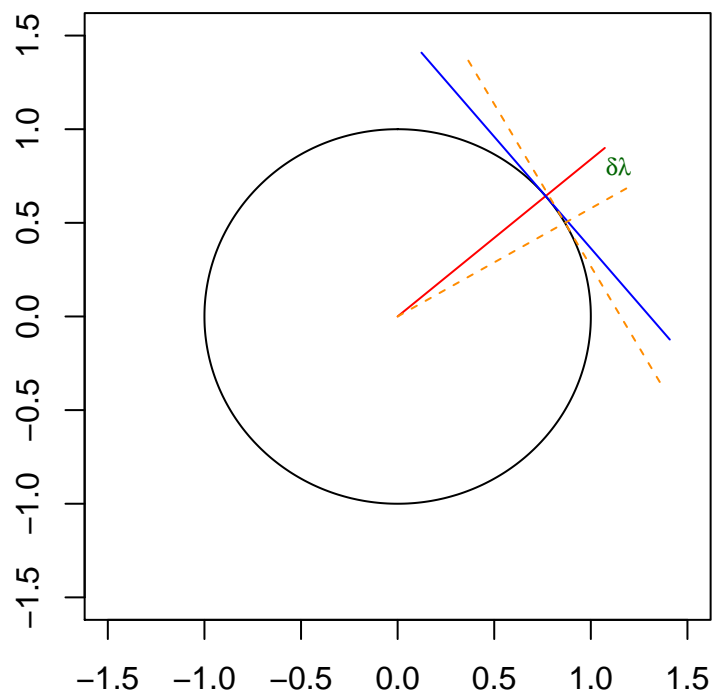


Figure 31: Illustration of how a position error, denoted here as an error in latitude $\delta\lambda$, leads to an error in the direction of the vertical axis and so to a false horizontal acceleration.

where x_n is the north coordinate of the position and a_n is the northward acceleration. However, if $a_n = a_n^* + \delta a_n$ where a_n^* is the true northward acceleration of the aircraft and δa_n is the erroneous acceleration that results from pitch and displacement errors, then

$$\delta a_n = g(\delta\lambda - \delta\theta) \quad (47)$$

with λ the latitude, $\delta\lambda = \delta x_n/R_e$ the error in latitude, and $\delta\theta$ the error in pitch. Then

$$\frac{d(\delta v_n)}{dt} = -g\delta\theta \quad (48)$$

$$\frac{d(\delta\theta)}{dt} = \frac{\delta v_n}{R_e} = -\frac{1}{g} \frac{d^2(\delta v_n)}{dt^2} \quad (49)$$

which has the solution:

$$\delta v_n = V_n \cos(\omega t + \zeta_n) \quad (50)$$

where $\omega = \sqrt{g/R_e} \simeq 0.00124$ is the Schuler angular velocity. The error in the north component of the velocity therefore oscillates with the Schuler period and a phase ζ_n . Integrating in time gives

$$\delta x_n = \int \delta v_n dt = \frac{V_n}{\omega} \sin(\omega t + \zeta_n) \quad (51)$$

The key to developing a correction to the pitch angle is that both δx_n and δv_n are observable because reference measurements are available from GPS. For example,

$$\begin{aligned} \delta x_n &= R_e(\text{LAT} - \text{GGLAT}) \\ \delta v_n &= \text{VNS} - \text{GGVNS} \end{aligned} \quad (52)$$

These observations can determine A_n and ζ_n in (50). From these, the error in pitch can be found from (48):

$$\delta\theta = -\frac{1}{g} \frac{d(V_n \cos(\omega t + \zeta_n))}{dt} = \frac{V_n \omega}{g} \sin(\omega t + \zeta_n) \quad (53)$$

Analogous equations lead to a similar coupling between the roll angle and the east component of the ground velocity:

$$\delta\phi = \frac{V_e \omega}{g} \sin(\omega t + \zeta_e) \quad (54)$$

where ϕ is the roll angle and V_e and ζ_e are determined from fits to the observed error $\delta v_e = \text{VEW} - \text{GGVEW}$.

Thus the observed errors in the components of the aircraft ground speed can be used to find corrections to be applied to the measurements of pitch and roll.

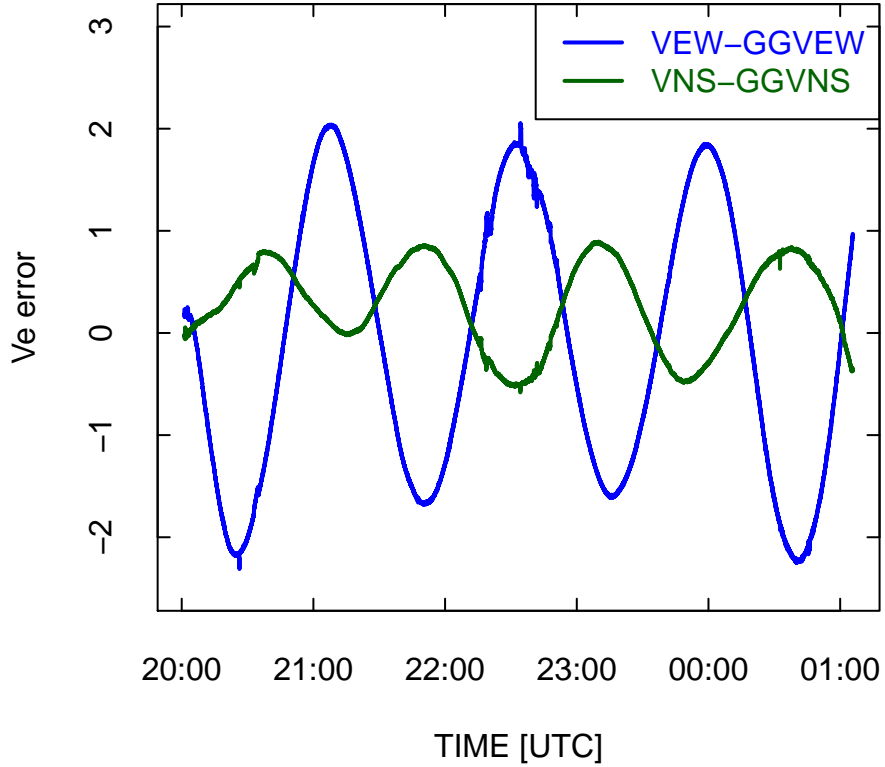


Figure 32: Errors in the NS and EW components of ground speed as determined by comparison to GPS, for DEEPWAVE flight ff02, a ferry flight starting on 1 June 2014 and traveling from Hawaii to Pago-Pago.

5.4.3 Illustrative example

An example from the second ferry flight of DEEPWAVE is shown in Fig. 32. The heading for most of this flight is close to southbound and steady, so to a reasonable approximation the errors in pitch and heading will be given by the respective derivatives in the error terms δv_n and δv_e .

The errors can be determined directly from the time-derivatives of the error terms in (48) and the analogous equation for roll, restated as:

$$\delta\theta = -\frac{1}{g} \frac{d(\delta v_n)}{dt} \quad (55)$$

$$\delta\phi = -\frac{1}{g} \frac{d(\delta v_e)}{dt} \quad (56)$$

Therefore, rather than fitting variations like that shown in Fig. 32 to sine or cosine functions, it

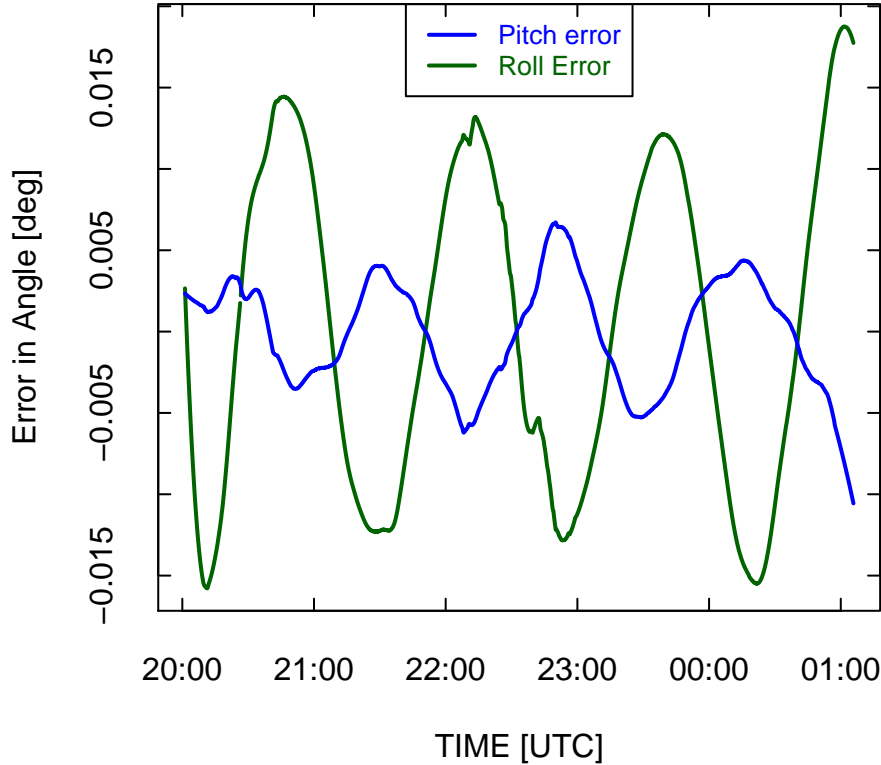


Figure 33: Deduced error in pitch and roll angles for DEEPWAVE ferry flight ff02.

is possible to obtain an estimate of the time derivatives of the velocity-error terms over some shorter interval and then use that derivative in (55) or (56) to find the errors in pitch and roll. It is important to note, though, that this gives errors in the local reference frame with axes eastward, northward, and upward, here called the l-frame, and these errors will then need to be transformed to the aircraft reference frame to get errors in the measured quantities. The choice made here is to estimate the derivatives using Savitzky-Golay polynomials, as shown in Fig. ?? . Savitzky-Golay polynomials were chosen because they are computationally efficient, don't introduce a time shift, and can provide derivatives directly. A rather long averaging period of 1009 s, or about 1/5 of a Schuler oscillation, was used to reduce noise in the result, and interpolation filled some gaps in the measurements.

The result is that the pitch error is limited to about 0.01° in magnitude for most of this flight, except for the final descent, and the roll error is limited to less than about 0.015° for the same period. This is evidence for low uncertainty in the pitch measurement for this flight, well below the specification of 0.05° . Section 5.4.5 contains further discussion of the errors from the research flights, where the estimated errors can be larger.

5.4.4 Transformation of attitude angles

In a reference frame called the l -frame or ENU frame, where the coordinate axes are local-east, local-north, and upward, the preceding subsection showed that the pitch and roll errors are related, via (55) and (56), to the time-derivatives of the errors in horizontal velocity. Pitch and roll as used in these equations will be the respective errors in platform alignment¹⁶ in the north-south and east-west directions, so these angles must be transformed to account for the orientation of the aircraft when it is not flying straight-and-level to the north. Coordinates in the body or b -frame of the aircraft are obtained from those in the ENU or l -frame by applying three rotations to account for the heading, pitch, and roll of the b -frame. This transformation leads to pitch errors in the body frame of the aircraft (where measured pitch and roll are measured and where the pitch measurement affects the calculated vertical wind) that are mixtures of pitch and roll errors in the l -frame, with the mixture dependent primarily on the heading. A positive pitch error for northbound level flight will be a negative pitch error for southbound level flight, and for eastbound flight an l -frame roll error becomes a b -frame pitch error while an l -frame pitch error become a negative b -frame roll error.

Consider a unit vector $\mathbf{b}^{(l)}$ representing the orientation errors in pitch and roll in the l -frame, with components $\{\sin \delta\phi, \sin \delta\theta, \sqrt{1 - \sin^2 \delta\phi - \sin^2 \delta\theta}\}$ or, because the errors are always small, approximately $\{\delta\phi, \delta\theta, 1\}$. The three-angle transformation of this vector from the l -frame to the b -frame is then represented by the following matrices, with $\{\phi, \theta, \psi\}$ denoting {roll, pitch, heading}:

$$R_l^b = \begin{bmatrix} \cos \psi \cos \phi + \sin \psi \sin \phi \sin \theta & -\sin \psi \cos \phi + \cos \psi \sin \phi \sin \theta & -\cos \theta \sin \phi \\ \sin \psi \cos \theta & \cos \psi \cos \theta & \sin \theta \\ \cos \psi \sin \phi - \sin \psi \sin \theta \cos \phi & -\sin \psi \sin \phi - \cos \psi \sin \theta \sin \phi & \cos \theta \cos \phi \end{bmatrix} \quad (57)$$

If the roll and pitch angles are small,

$$\mathbf{b}^{(b)} = R_l^b \mathbf{b}^{(l)} \approx \begin{bmatrix} \cos \psi & -\sin \psi & 0 \\ \sin \psi & \cos \psi & 0 \\ 0 & 0 & 1 \end{bmatrix} \begin{bmatrix} \delta\phi \\ \delta\theta \\ 1 \end{bmatrix} = \begin{bmatrix} \cos \psi \delta\phi - \sin \psi \delta\theta \\ \sin \psi \delta\phi + \cos \psi \delta\theta \\ 1 \end{bmatrix} \quad (58)$$

which leads to $\delta\theta^{(b)}$ and $\delta\phi^{(b)}$, the pitch and roll errors in the b -frame:

$$\begin{aligned} \delta\theta^{(b)} &\simeq \sin \psi \delta\phi + \cos \psi \delta\theta \\ \delta\phi^{(b)} &\approx \cos \psi \delta\phi - \sin \psi \delta\theta \end{aligned} \quad (59)$$

In turns, the roll angle is no longer negligible, so in general the full transformation matrix (57) should be used. Because this matrix imposes rotations by the measured pitch and roll angles,

¹⁶The inertial system used is a strap-down system, so there is no actual motion of the “platform”. Instead, from measured rotations and accelerations, the system calculates the expected orientation if there were a true stabilized platform. The errors referenced here are those relative to that calculated platform orientation.

the unit vector representing the errors in pitch and roll after transformation will have components from which the true pitch and roll can be determined, so subtracting the corrected pitch from the measured pitch gives the error in measured pitch:

$$\delta\theta^{(b)} = \theta - \arctan \frac{b_2^{(b)}}{b_3^{(b)}} \quad (60)$$

This pitch error should then be subtracted from the measured pitch to obtain a corrected value of the pitch for use in the calculation of vertical wind.

5.4.5 Application to research flights

The research flights have frequent changes in heading, with mixing of the roll and pitch errors but also accelerations that affect those errors and introduction of new errors from heading errors. The corrections to pitch therefore appear much less systematic than was the case for the ferry flight. An example, DEEPWAVE flight 1, is presented here. Figure 34 shows the measured errors in ground-speed components, and Fig. 35 shows the deduced pitch and roll errors. There are instances where the pitch error abruptly reverses sign; those are cases where the flight direction changes by about 180 deg. During turns, the full transformation leads to a result significantly different from the small-angle-approximation result, as shown by the orange line in Fig. 35, but when not turning the full-transformation results replicate the small-angle-approximation results (blue line), as indicated by the orange dashed line overlapping the blue line. The proposed solution is to use the full transformation for processing a corrected pitch variable, to be named “PITCHC”, to be used for calculation of the vertical wind. In straight-and-level flight, the needed corrections are about $\pm 0.03^\circ$ at some times, and this error can lead (for true airspeed of 220 m/s) to an error in vertical wind of about ± 0.1 m/s. Correction for this error thus should lead to a significant reduction in the uncertainty associated with the measured vertical wind.

5.4.6 Tests of the correction

Two tests were used to test if these pitch corrections made any significant difference in the measurements of vertical wind. First, wind measurements made before and after level course reversal were compared to see if correcting the pitch reduces the difference in measurements on the two legs before and after turns. Reduction would be expected because if there is a pitch error it would reverse sign between the two legs, increasing their absolute difference. Second, flight-average and project-average vertical wind measurements were compiled without and with the pitch correction.

The following is a tabulation of five instances where the flight track reversed course and remained at the same altitude. A number of other candidates were excluded because conditions were too variable along the legs to produce a small-uncertainty estimate of the vertical wind. In each case, flight periods of about 5 min (sometimes adjusted in times of strong wind to give similar-length segments flown upwind and downwind) are listed before and after the turn, but

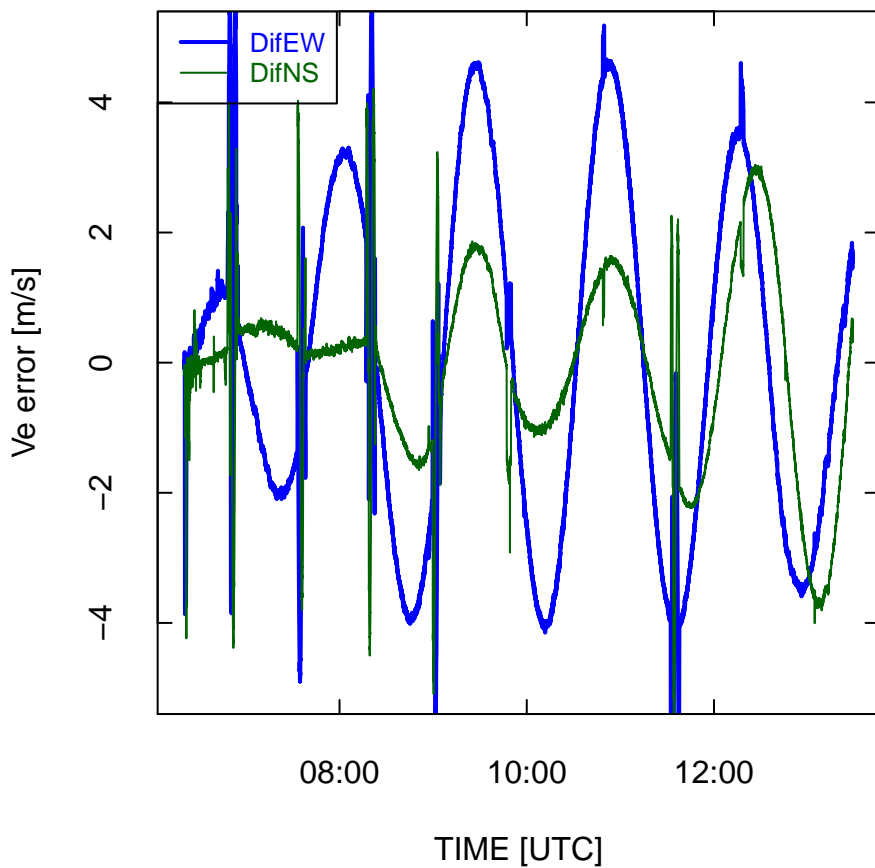


Figure 34: Measured errors in ground-speed components for DEEPWAVE flight 1. VEW and VNS are the east and north components of the ground speed measured by the inertial system, and GGVEW and GGVNS are the corresponding components measured independently by the GPS system.

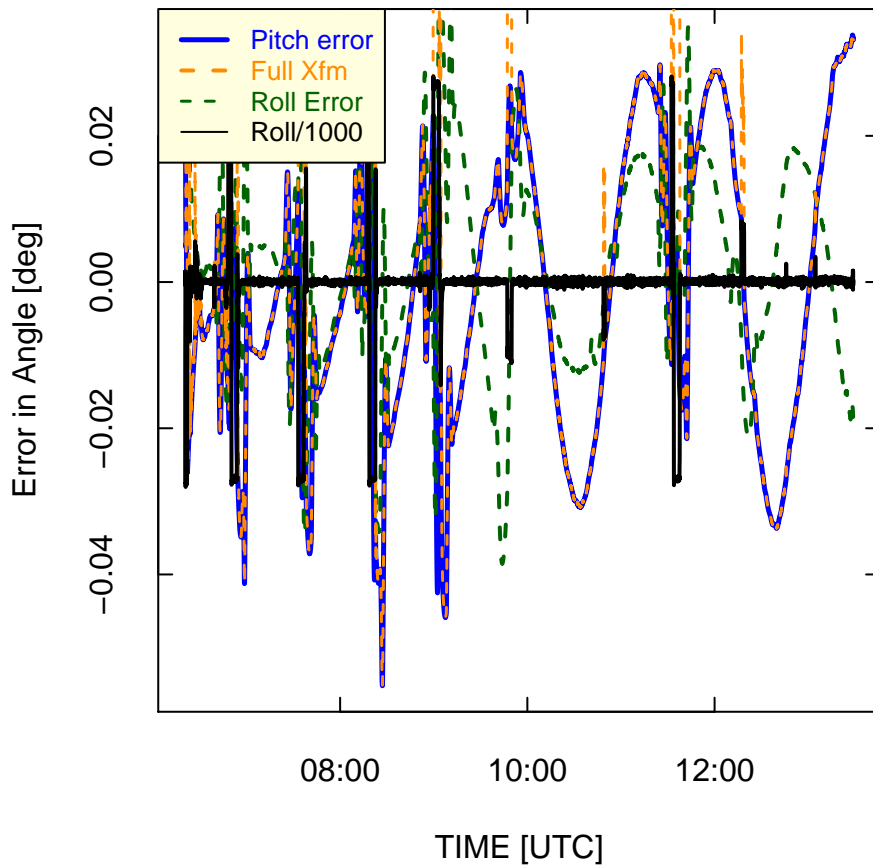


Figure 35: Errors in pitch and roll determined from the measured errors in ground-speed components, after transformation to the reference frame that is the body frame of the aircraft. The orange line labeled 'Full Xfm' uses (58) and (60), while the blue line uses the approximate result (59). The limits ± 0.03 correspond to roll angle of $\pm 30^\circ$ after division by 1000, so the regions with vertical black lines are ones with significant roll.

excluding the turn, to represent approximately overlapping flight segments where it would be expected that the vertical wind would be the same.

Flight	Times before turn	Times after turn
1	81000–81600	82400–83000
2	122500–123000	123700–124300
19	83930–84430	85130–85630
21	85100–85500	90300–90730
21	95630–100130	100800–101300

The difference between average vertical wind measurements for each pair of legs was calculated before and after applying the pitch-correction algorithm developed in this subsection. The measurements were in good agreement without any pitch correction, with an average absolute value of the difference between opposing legs of 0.09 m s^{-1} . The pitch correction kept the averages quite small and improved the agreement, reducing the mean value of the difference to 0.03 m s^{-1} . More significant than this reduction is that the values were so small even before correction. This is a good indicator of the low uncertainty of the pitch measurement even without correction. A course-reversal difference of 0.1 m s^{-1} would result from a pitch error of less than 0.015° , so this suggests that the inertial system is performing significantly better than its specified uncertainty (0.05°). After correction, the mean difference suggests an error of less than 0.005° for the corrected values.

Table 9 lists the mean vertical wind with and without pitch correction for each of the DEEP-WAVE flights. For each flight, all measurements above 25,000 ft with true airspeed above 130 m/s and roll between -5 and 5° were included to emphasize normal research conditions. Any missing measurements were also excluded from the averages, and measurements from flights 6, 7, and 15 are not included because the first two were cases where the conventional vertical-wind measuring system malfunctioned and flight 15 was a flight devoted to calibration with little upper-level flight and frequent turns including circles.

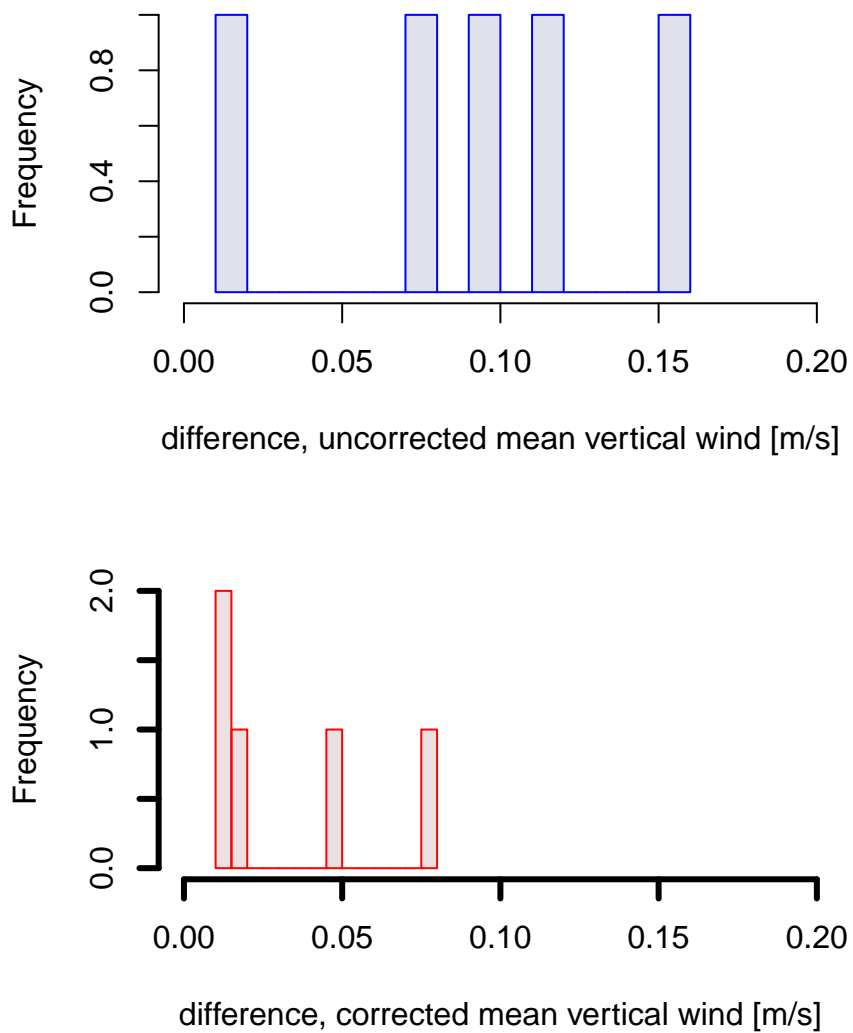


Figure 36: Absolute difference in vertical wind for flight segments before and after level course-reversal maneuvers. The top panel shows the uncorrected measurements and the bottom panel shows the result of applying the pitch correction developed in this subsection.

flight	mean WIC	mean corrected WIC
1	-0.01	-0.02
2	0.03	0.02
3	-0.07	-0.07
4	-0.09	-0.14
5	0.03	-0.02
8	0.01	-0.03
9	0.02	0.01
10	0.15	0.13
11	0.08	0.08
12	0.07	0.04
13	0.02	-0.01
14	0.08	0.08
16	0.07	0.05
17	0.02	0.01
18	-0.07	-0.07
19	0.08	0.08
20	0.07	0.06
21	0.11	0.08
22	0.02	0
23	0.07	0.07
24	0.03	0.03
25	-0.02	-0.02
26	0.03	0.03

Table 9: The average vertical wind for each flight, before and after application of the pitch-correction algorithm developed in this subsection. The data restriction applied was that the true airspeed be above 130 m/s, absolute value of the roll less than 5° , and the flight level above 25,000 ft (to emphasize normal research measurement conditions in the DEEPWAVE project). Flights 6, 7, and 15 are also missing, as explained in the text.

The mean value of the vertical wind, for all flights combined, was 0.03 m/s for the uncorrected measurements and 0.02 m/s for the corrected measurements, with standard deviations of

0.06 m/s, so both are well within expected tolerances. The pitch correction has little effect on these mean measurements or the overall standard deviation. However, the small offset obtained with the pitch corrections applied does not indicate that the measurements are only uncertain within these limits, because most flights are long compared to the Schuler-oscillation period of about 84 min. Flights will average over an oscillating correction and that average may be small compared to the correction applied. The standard deviation of the applied correction is 0.02° when calculated for the entire project. That indicates that the correction to vertical wind arising from application of the pitch-correction algorithm introduces changes with standard deviation of about 0.09 m s^{-1} project-wide. Studies of individual flights show that this varies significantly from flight to flight. This uncertainty, however, is a significant contributor to the uncertainty in vertical wind. Without pitch correction, measurements of vertical wind will have an error with typical period of the Schuler oscillation that, for measurements spanning much shorter periods, will appear as a slowly varying bias.

The correction procedure developed here is not suited to application during normal processing of data files because it uses a fit to the entire sequence of ground-speed measurements to find the corrections while the normal processor is sequential. An R script has been developed to add values of pitch and vertical wind after correction, but this must be run after the original file is generated. The correction only applies to the Honeywell IRUs; The C-MIGITSIII units already incorporate Kalman feedback from a GPS signal and so already apply a correction similar to the one applied here.

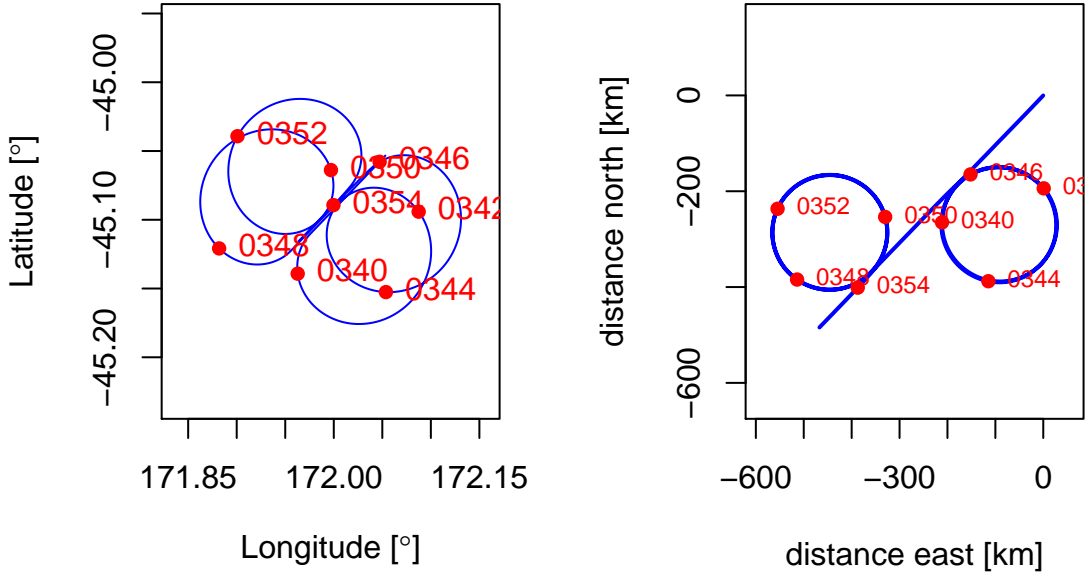


Figure 37: An example of circle flight pattern, from DEEPWAVE flight 15, 3:38:30–3:54:30 UTC. Left side: normal flight track referenced to ground coordinates; right side, flight track plotted in a Lagrangian reference frame drifting with the horizontal wind.

6 Studies of the Horizontal Wind

6.1 Analysis of circle maneuvers

6.1.1 Data Used

During the DEEPWAVE project, several circle patterns were flown to help characterize and check the wind measurements. In these maneuvers, a constant roll angle was maintained so that the flight track drifted with the wind, and that drift alone provides a measurement of mean horizontal wind that is dependent only on the measurement of position from the GPS. The example used here is from DEEPWAVE flight 15, 3:38:30–3:54:30 UTC, during which two circles were flown with left roll and then two with right roll, as shown in Fig. 37.

6.1.2 Constraints arising from the assumption that the wind is steady

The circle maneuver is a stringent test of the wind measurements because, in steady conditions, the measured wind should remain constant around the circles. From the patterns of deviations with orientation in the turn, it is possible to detect an error in true airspeed or an offset in heading or sideslip. A time offset in measured ground speed from the GPS relative to the IRU can be

detected from an apparent change in required heading offset that changes sign with the direction of the turn. In addition, for circles flown with steady bank angle, the drift of the ground track as detected by GPS measures the wind without any reference to the measuring system on the aircraft, so this provides a standard against which the wind measurements can be checked.

For these patterns, the wind should be relatively steady and non-turbulent and the roll angle should be constant. For this flight segment, the left-turn circles had a roll angle of -26.92 ± 0.17 and the right-turn circles had roll angle 27.08 ± 0.12 , while the mean true airspeed for these circles was 153.5 ± 0.5 . Most of the standard deviation in true airspeed arose from the normal fluctuations created by the flight management system, as discussed in Sect. 5.2.2 (cf. Fig. 28). The steadiness of these measurements indicates that this maneuver was flown with good precision and symmetrically, so the following is a good illustration of what can be learned from this maneuver.

6.1.3 Basic equations

The quantity used in all these tests is the relative wind in Earth-based coordinates, with east and north components given approximately by $\{V \sin \psi', V \cos \psi'\}$ where $\psi' = \psi + \beta \cos \phi - \alpha \sin \phi$ with ψ the heading, β the sideslip angle, ϕ the roll angle, and α the angle of attack. In the circle maneuver, $\phi \approx 27^\circ$ so the last two terms in the expression for ψ' do not simplify with the small-angle approximation. If the corresponding components of the horizontal wind are v_x and v_y , the components of the ground speed of the aircraft are

$$\begin{aligned} v_{p,x} &= V \sin \psi' - v_x \\ v_{p,y} &= V \cos \psi' - v_y \end{aligned} \quad (61)$$

and the difference between the motion of the aircraft expressed as (61) and the ground-speed components measured by GPS ($v_{g,x}, v_{g,y}$) is

$$\begin{aligned} \delta v_x &= V \sin \psi' - v_x - v_{g,x} \\ \delta v_y &= V \cos \psi' - v_y - v_{g,y} \end{aligned} \quad . \quad (62)$$

If error terms for true airspeed (δV) and for the adjusted heading angle ($\delta \psi'$) are introduced so that $V = V_m + \delta V$ and $\psi' = \psi'_m + \delta \psi'$ where subscript m refers to the measured quantity, and if it is assumed that the wind components $\{v_x, v_y\}$ are steady around the circles, then estimates for the four fit parameters $\{\delta V, \delta \psi', v_x, v_y\}$ can be found by minimizing the errors given by (62).

Once the average wind direction (λ) and wind speed (v) have been determined either by the above fit or from the mean of measurements around the circles,¹⁷ the error δv_m in the measurement of wind speed (v_m) can be expressed as

$$\delta v_m = v_m - v = -\delta V \cos \xi - V \delta \xi \sin \xi \quad (63)$$

¹⁷With equal weighting for measurements with all orientations relative to the wind, averaging measurements should give correct values even if there are errors in the individual terms

where $\xi = \psi' - \lambda$ is the angle between the relative wind (in the direction ψ' which is the heading adjusted for the roll angle by components from the sideslip and angle of attack) and the direction x of the wind relative to the Earth (λ).

This equation is justified as follows. Because the relative wind transformed to an Earth reference frame is added to the ground-speed vector to find the wind, an error δV in true airspeed leads to an error of the same magnitude in the component of measured wind along the longitudinal axis of the aircraft. The measured wind therefore changes by $-2\delta V$ when the aircraft changes from an upwind to a downwind flight direction, with the negative sign arising from the convention that wind direction is specified as the direction from which the wind blows. The error in true airspeed thus can be determined from the difference between wind measured while flying upwind and that measured while flying downwind. For other flight directions, this error projects to the wind direction as $-\delta V \cos(\psi')$. Similarly, when flying crosswind the wind measurement is determined by the sum of the ground-speed component along the wind direction and the component of the relative wind lateral to the aircraft. If the wind is from the port side of the aircraft (e.g., for an east flight direction with wind from the north), a positive heading error leads to a relative wind component opposing the wind and so to a measurement error of $-V\delta\psi'$. For wind from the starboard side of the aircraft, the sign reverses, and for other angles the error contribution is $-V\delta\psi' \sin(\psi')$.

Fitting to minimize the deviations expressed by (63) can then give estimates of the three fit parameters δV , $\delta\psi'$, and v , or a fixed value can be used for v as given by the mean of measurements or by a previous fit to (62). These fits should give consistent results, but a fit to (63) is particularly illustrative because plots of the error as a function of flight direction relative to the wind clearly reveal the magnitude and source of the deviations. The expected pattern is shown in Fig. 38.

6.1.4 Finding the wind from the GPS ground track

From the definitions (62), the mean wind can be found by adjusting the fit parameters v_x , v_y , δV and $\delta\psi$ to minimize the error measure $\chi^2 = \sum(\delta v_x^2 + \delta v_y^2)$. The results, with wind converted to wind direction λ and wind speed v , are shown in Table 10 for the full circle maneuver and also separately for the right-turn circles and left-turn circles.

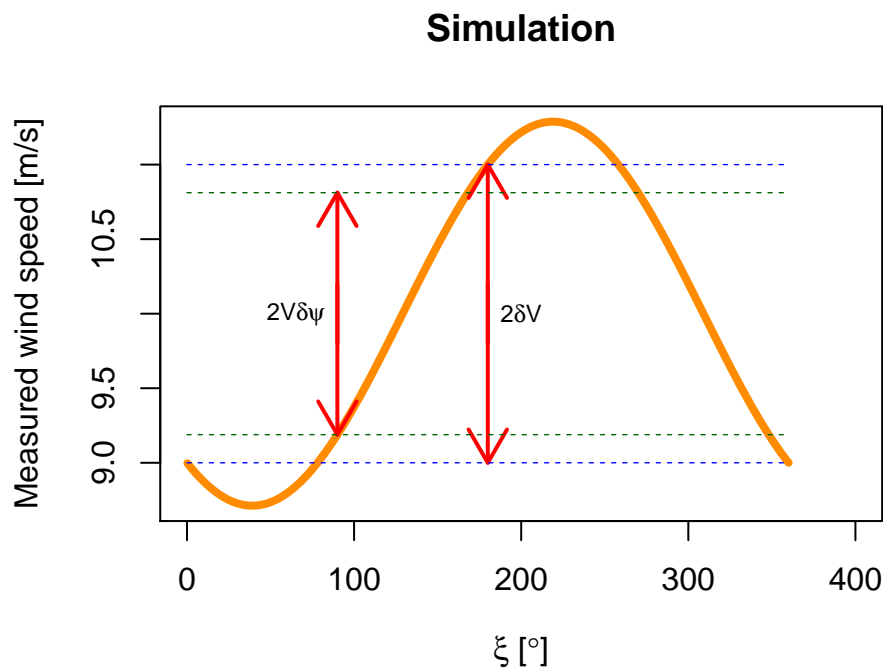


Figure 38: Illustration of the expected variation in measured wind speed with flight angle relative to the wind direction, for assumed errors of $\delta V = 1$ m/s in true airspeed and $\delta\psi' = 0.3^\circ$ in heading and for an assumed true wind speed of 10 m/s. The assumed true airspeed is 155 m/s. The red arrows show the differences in measured wind speed between 90° and 270° directions and between 0° and 180° directions.

	λ [°]	v [m/s]	δV [m/s]	$\delta \psi'$ [°]	residual error [m/s]
all turns	222.8	17.7	0.4	-0.05	1.0
mean of measurements	222.8	18.0			
left turns	222.9	18.3	0.5	-0.05	1.0
left-turn measurements	222.8	18.5			
right turns	222.6	17.2	0.3	-0.06	0.4
right-turn measurements	222.8	17.5			

Table 10: The best-fit parameters that minimize the errors given by (62) for the first circle maneuver from DEEPWAVE flight 15, 3:38:30–3:56:30 UTC, at an altitude of about 4.1 km (13,500 ft). The lines "mean of measurements", "left-turn measurements" and "right-turn measurements" are based on the wind measurements from the aircraft data system.

There is an apparently significant difference of about 1 m/s in mean wind speed, both measured and resulting from the fits, between the right-turn circles and the left-turn circles. This is apparently a real difference between wind conditions in the regions where the circles were flown and is supported by the difference between maximum and minimum ground speed for the two sets of circles. Conditions are more uniform for the right-turn circles, as reflected in the lower residual error for those circles, so more weight will be given here to the results from the right-turn circles.

The fits point to a very small heading error that is consistent for the two turn directions. That result is very sensitive to the timing of signal acquisition; any difference in timing between the ground-speed components from the GPS and the heading measurement from the IRU will produce an indicated error in heading that changes sign with turn direction. Shifting either pitch or ground-speed components by 40 ms changes the indicated errors in heading by 0.07°, so these lags are very sensitive to the assumed delay. The results here were obtained for a heading shift of -50 ms, slightly different from the conventional shift of -80 ms, and with no shift imposed on the GPS measurements of ground-speed components. Also, no offset was applied to heading. For documentation, the attributes for the heading variable as processed for this study are listed here:

```
## [1] "attributes for variable"
## [1] "_FillValue: -32767"
## [1] "units: degree_T"
## [1] "long_name: IRS Aircraft True Heading Angle"
## [1] "standard_name: platform_orientation"
## [1] "valid_range: c(0, 360)"
## [1] "actual_range: c(0.00287811458110809, 359.997497558594)"
## [1] "Category: Analog"
## [1] "SampledRate: 25"
## [1] "TimeLag: -50"
```

```
## [1] "TimeLagUnits: milliseconds"
## [1] "DataQuality: Preliminary"
## [1] "CalibrationCoefficients: c(0, 1)"
## [1] "modulus_range: c(0, 360)"
```

Two other circle patterns were flown on this same flight, at about 4:35:00–4:53:00 and 5:30:00–5:53:00 UTC. Similar tables for those circle maneuvers are shown in Tables 11 and 12. In these three cases, indicated airspeed corrections from individual circles varied from -0.6 to 0.6 m/s and angular corrections (combining heading and sideslip errors) varied from 0.01 to 0.23° , with mean values of 0.2 ± 0.2 m/s and $0.13 \pm 0.03^\circ$.

	λ [$^\circ$]	v [m/s]	δV [m/s]	$\delta\psi'$ [$^\circ$]	residual error [m/s]
all turns	230.7	22.8	0.5	-0.01	0.6
mean of measurements	230.4	22.2			
left turns	231.3	22.6	0.5	-0.02	0.6
left-turn measurements	231.2	22			
right turns	230.1	23	0.6	-0.01	0.4
right-turn measurements	229.6	22.5			

Table 11: The best-fit parameters that minimize the errors given by (62) for the second circle maneuver from DEEPWAVE flight 15, 4:35:00–4:53:00 UTC, at an altitude of about 6.1 km (20,000 ft). The lines "mean of measurements", "left-turn measurements" and "right-turn measurements" are based on the wind measurements from the aircraft data system.

	λ [$^\circ$]	v [m/s]	δV [m/s]	$\delta\psi'$ [$^\circ$]	residual error [m/s]
all turns	253.7	7	-0.2	-0.04	1.3
mean of measurements	253.7	7.2			
left turns	256.6	7.1	-0.6	-0.14	1.4
left-turn measurements	256.4	7.6			
right turns	250.9	6.9	0.2	0.05	0.8
right-turn measurements	251.1	6.8			

Table 12: The best-fit parameters that minimize the errors given by (62) for the third circle maneuver from DEEPWAVE flight 15, 5:30:30–5:53:00 UTC, at an altitude of about 9.1 km (30,000 ft). The lines "mean of measurements", "left-turn measurements" and "right-turn measurements" are based on the wind measurements from the aircraft data system.

6.1.5 Minimizing the variation in measured wind speed in circle maneuvers

The fit results in Tables 10–12 and also the mean measurements of the wind in those tables provide reference angles for the wind direction, so those angles can be used in fits that minimize (63). Because there is significant variation among the circles, the tabulated values for fitted values for the appropriate set (all turns, left turns, or right turns) will be used as the value of λ when fitting. An appropriate error function to minimize to find values for the parameters δV , $\delta \psi'$, and v in (63) is $\chi^2 = \sum \delta v_m^2$.

Tables 13–15 show the fit results for the three circles:

	v [m/s]	δV [m/s]	$\delta \psi'$ [$^\circ$]	residual error [m/s]
all turns	18	0.5	-0.15	0.6
left turns	18.5	0.7	-0.20	0.2
right turns	17.5	0.2	-0.10	0.2

Table 13: The best-fit parameters that minimize the errors given by (63) for the first circle maneuver from DEEPWAVE flight 15, 3:38:30–3:56:30 UTC.

	v [m/s]	δV [m/s]	$\delta \psi'$ [$^\circ$]	residual error [m/s]
all turns	22.3	0.7	-0.08	0.3
left turns	22	0.8	-0.07	0.2
right turns	22.5	0.7	-0.08	0.2

Table 14: The best-fit parameters that minimize the errors given by (63) for the second circle maneuver from DEEPWAVE flight 15, 4:35:00–4:53:00 UTC.

	v [m/s]	δV [m/s]	$\delta \psi'$ [$^\circ$]	residual error [m/s]
all turns	7.1	-0.5	0.17	1.0
left turns	7.5	-1.1	0.37	0.7
right turns	6.8	0.2	0.00	0.5

Table 15: The best-fit parameters that minimize the errors given by (63) for the third circle maneuver from DEEPWAVE flight 15, 5:30:00–5:53:00 UTC.

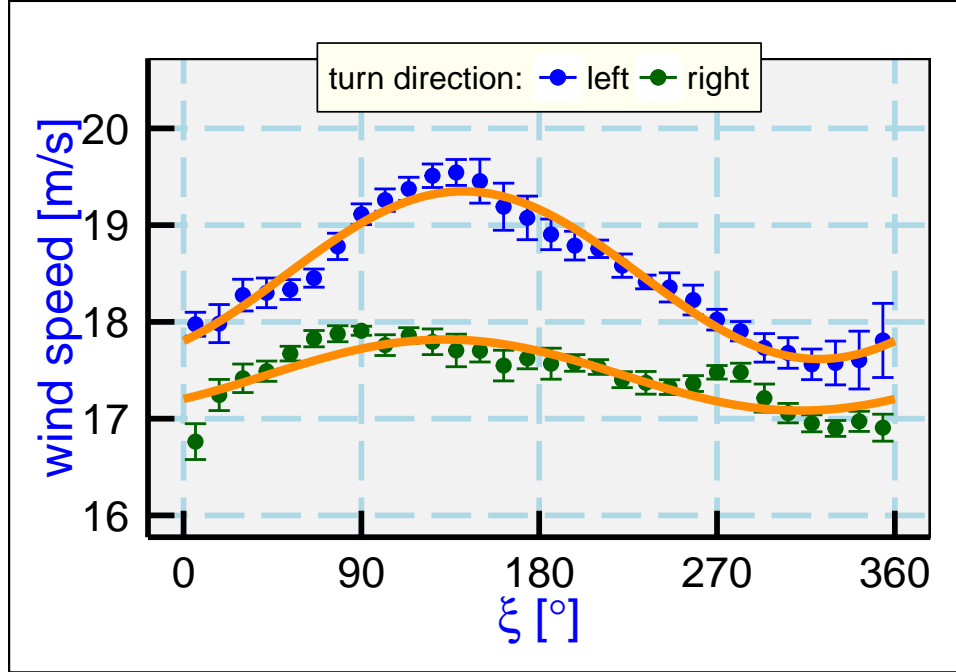


Figure 39: Measured wind speed from the left-turn and right-turn circles in the circle pattern shown in Fig. 37, as a function of ξ , the difference between the adjusted heading and the mean wind direction. Orange lines are the results of fitting (63) to the measurements, with results as listed in Table 13.

Figures 39–41 show the mean measurements of wind speed as a function of the angle between the mean wind direction and the adjusted heading representing the motion of the aircraft relative to the air. The two turn directions are shown separately in each figure because they often require a different mean wind speed, as also shown in Tables 10–12 where the fit results are tabulated. The fits to (63), found by minimizing the defined χ^2 , are also shown in this figures (orange lines).

Some of the fits, notably the left-turn circles from the third maneuver, don't conform very well to the expected sinusoidal error pattern. The residual error about the fit was the largest of the circles, with the right-turn circles having almost as large a residual error, which may indicate that conditions were not sufficiently uniform to use these maneuvers. However, if all six are averaged, the mean values for the indicated error in airspeed is 0.25 ± 0.32 m/s, and the indicated error in adjusted heading ψ' is $-0.01 \pm 0.09^\circ$, where the indicated ranges are the standard deviations estimated for the mean values. These are useful constraints on the uncertainty associated with these key contributors to uncertainty in measured wind.

Offset in Sideslip In the preceding, the error $\delta\psi'$ was discussed as an error in adjusted heading, but that adjustment includes the sideslip so the error could also be one in sideslip. These errors are difficult to separate, and normal sideslip calibration (Sect. 4.2 even with reverse-heading maneuvers does not provide a separation. Furthermore, heading errors may change

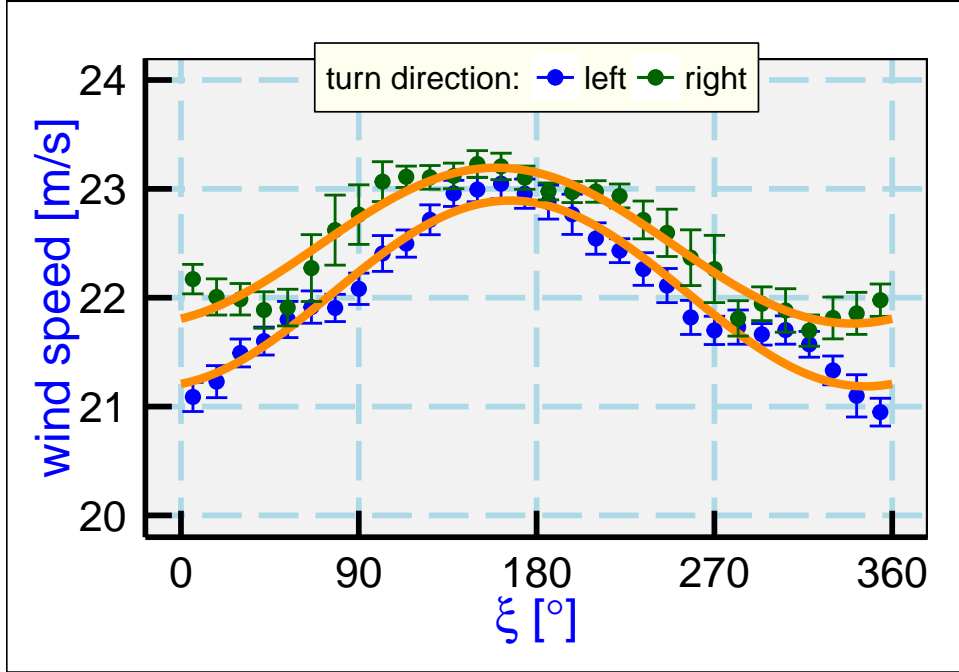


Figure 40: Measured wind speed from the left-turn and right-turn circles in the second circle pattern as a function of ξ , the difference between the adjusted heading and the mean wind direction. Orange lines are the results of fitting (63) to the measurements, with results as listed in Table 14.

during a flight because error terms undergo a Schuler oscillation and are also affected by horizontal accelerations such as occur persistently in turns like those in the circle maneuver.

The error term determined as in the above tables should be represented by $\delta\psi'$ given by

$$\delta\psi' = \delta\psi + \cos\phi\delta\beta \quad (64)$$

where ϕ is the roll angle and $\delta\beta$ is the offset in sideslip.¹⁸ Because the dependence in (64) is on the cosine of the roll which is an even function, left and right turns are affected in the same way and also cannot distinguish the two terms in the equation. Even though three different altitudes were used for these circle maneuvers, the GV flight management system maintains nearly the same roll angle for all three maneuvers so changes in roll also cannot be used to distinguish the contributions from heading offset and sideslip offset.

One approximate test is to compare the sideslip measurement in left vs right turns. The measurements of sideslip¹⁹ are shown in Fig. 42. In the turns, some sideslip is introduced as the aircraft configuration remains slightly nose-up during the turn, and that sideslip should reverse sign by symmetry when the flight pattern changes from left-turn to right-turn circles. The lift required to maintain altitude would be the same if the roll angles were opposite, as they nearly

¹⁸The angle of attack was determined by separate calibration in Sect. 4.1.2 so that contribution to ψ' is not included in the error term.

¹⁹The sensitivity coefficients as determined in Sect. 4.2 have been used to construct this figure.

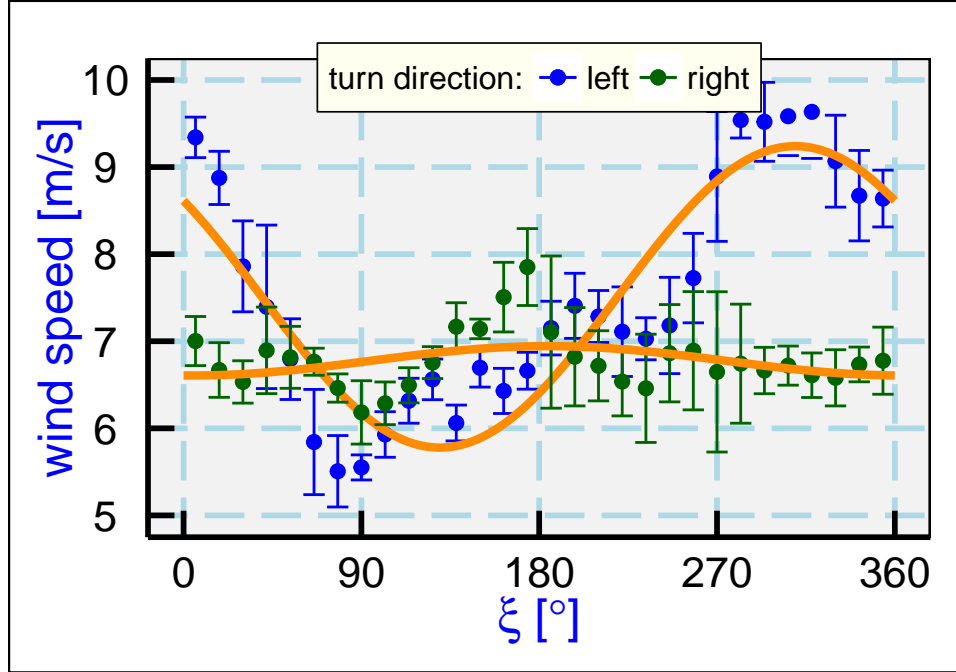


Figure 41: Measured wind speed from the left-turn and right-turn circles in the third circle pattern as a function of ξ , the difference between the adjusted heading and the mean wind direction. Orange lines are the results of fitting (63) to the measurements, with results as listed in Table 15.

are for these maneuvers (0.45° larger for right turns), and the angle of attack is also close to the same, so the expected sign reversal in sideslip can be used to estimate the offset in sideslip.

```
## [1] " mean for maneuver: 0.01; left turns -0.30 and right turns 0.30"
```

The mean value for the full maneuver, and the average of the right-turn and left-turn circles, both indicate that there is no offset in the sideslip. However, this approach is sensitive to any variations in pitch, and there were small but significant variations in pitch in the maneuvers.²⁰ The alternative is to take into account the influence of all angles on vertical wind. The transformation equations from [Lenschow and Spyers-Duran \[1989\]](#) (see also [Lenschow \[1972\]](#)), with some small-angle simplifications, lead to this equation for the vertical wind:

$$u_z = w_p + V(\sin \phi \tan \beta + \cos \phi \tan \alpha - \sin \theta) \quad (65)$$

where w_p is the vertical motion of the aircraft, V its true airspeed, ϕ the roll angle, β the sideslip angle, α the angle of attack, and θ the pitch angle. If it is assumed that the vertical wind is zero, in the circle maneuver this equation predicts that the sideslip angle will be β^* given by

$$\beta^* \approx \frac{\theta - \alpha \cos \phi - (w_p/V)}{\sin \phi} . \quad (66)$$

²⁰This was first noticed in circle maneuvers by the C-130, where pitch variations are more significant during circles and this approach is necessary.

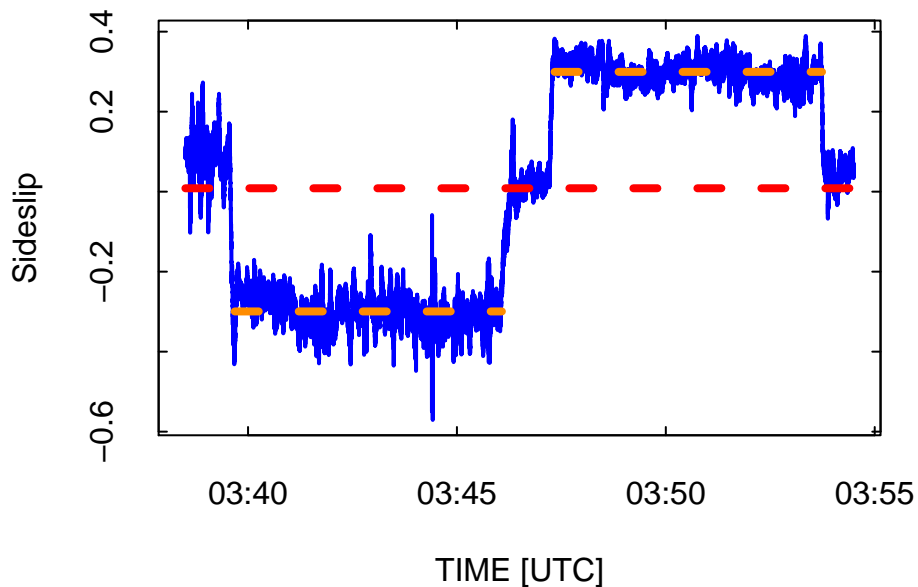


Figure 42: Measurement of sideslip during the first circle maneuver from DEEPWAVE flight 15, with left-turn circles from 3:40:00 – 3:46:00 UTC, followed by a straight segment and then right-turn circles 3:47:30 – 3:53:40 UTC.

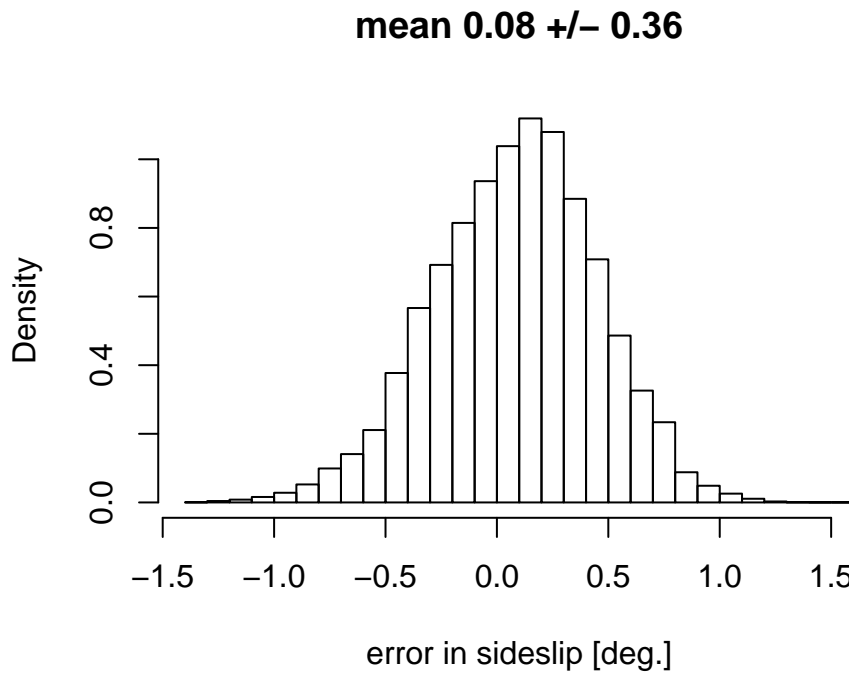


Figure 43: Distribution of measurements of sideslip error determined from (67) for all measurements in turns from the three circle maneuvers.

This is not useful in straight flight where the roll is near zero, but it provides a valid equation for sideslip in the case of steady turns. The key assumption is that the vertical wind is zero; a vertical wind of 0.1 m/s will typically increase the deduced sideslip from this equation by about 0.06° , so it is important that the circle maneuver be flown where there is no mean updraft. It is then possible to determine the offset in sideslip by comparing this prediction to the measured sideslip β_m :

$$\delta\beta = \beta_m - \beta^*. \quad (67)$$

```
## [1] "mean error in sideslip: 0.084 +/-0.001"
```

This result, indicating that 0.084° should be subtracted from the sideslip measurements,²¹ is different from the indication from Fig. 42, where no offset was required. The uncertainty in the estimated mean of this result is very low, and this result is more general because it uses measured values of the pitch, so this value will be used to correct the sideslip offset. This indicates that the sideslip sensitivity coefficients should be $\{e_0, e_1\} = \{0.008, 22.302\}$. Because this result is dependent on the vertical wind being zero, an uncertainty of at least 0.03° should be assigned to the first coefficient to recognize that the vertical wind might typically be ± 0.05 m/s in a region such as this.

²¹The value is the measurement error so the required correction is the negative of that value.

The results of the circle analyses point to a combined error from heading and sideslip of $-0.01 \pm 0.09^\circ$, so the indicated heading error calculated from (64) is $-0.09 \pm 0.09^\circ$. The required heading correction is then the negative of this value, and the result of this calibration is to make compensating adjustments in the offsets for heading and sideslip.

6.1.6 Summary

The results obtained from analysis of the circle maneuvers are these:

1. The circle maneuvers indicate that the measured true airspeed (TASX) with current LAMS-based pressure corrections is accurate to within expected uncertainty. The fits indicate an error in true airspeed of 0.25 ± 0.32 m/s, which is within the expected (± 0.3 m/s) uncertainty limits for TAS deduced using the LAMS calibration (Cooper et al. [2014]). The uncertainty includes the calibrated value, so it appears better to make no adjustment to true airspeed.
2. The indicated error in sideslip is 0.08° , so the first sensitivity coefficient should be reduced by this amount. That leads to sensitivity coefficients for the radome of $\{0.008, 22.302\}$. Cf. the discussion in Section 4 and the summary section 4.4.2 at the end of that section. It appears reasonable to consider that the bias in this measurement may be uncertain by about 0.03° because the mean offset is determined with this standard deviation from the combination of the available circle maneuvers and this is also the sensitivity to 0.05 m/s vertical wind during the maneuvers.
3. With the preceding sensitivity coefficients, an offset should be introduced to heading of magnitude $-0.06 \pm 0.09^\circ$. The evidence from the circle fits is that the combined bias associated with the heading and sideslip offsets is $-0.01 \pm 0.09^\circ$. The heading and sideslip offsets are coupled, so the two offsets indicated by the circle fits should be used together.
4. The ground-speed measurements GGVIEW and GGVNS from the Novatel GPS need to coincide with the inertial measurements. An assumed lag for pitch of 50 ms, along with no offset in GGVIEW and GGVNS, was indicated by the comparison between the two directions used for the circle maneuvers.

6.2 The complementary filter

Wind measurements combine a measurement of relative wind with a measurement of aircraft motion to determine the air motion relative to the ground. The aircraft motion has long been measured by an IRS, and recently also by a GPS. These have complementary strengths: The IRS provides very good information on short-term motion but drifts with a characteristic period of more than an hour, while the GPS provides good absolute accuracy but sometimes is unable to receive the GPS signals and (except in differential-GPS mode) can have short-term errors that make short segments of the track look jagged. To take advantage of the strengths of each, a complementary-filter calculation was developed and implemented in the 1980s, but it was never

documented publicly. This section is partly an attempt to remedy that and partly a suggestion to make some minor changes to how it is implemented. This discussion is complementary to the information in ProcessingAlgorithms.pdf, section 3.4, and contains additional detail as well as notes regarding implementation of changes.

To accomplish this combining of measurements, a low-pass filter, $F_L(\{GVNS, GVEW\})$, is applied to the GPS measurements of ground speed, $\{GVNS, GVEW\}$, which are assumed to be valid for frequencies at or lower than the cutoff frequency f_c of the filter. Then the complementary high-pass filter, denoted $(1 - F_L)(\{VNS, VEW\})$, is applied to the IRS measurements of ground speed, $\{VNS, VEW\}$, which are assumed valid for frequencies at or higher than f_c . Ideally, the transition frequency would be selected where the GPS errors (increasing with frequency) are equal to the IRS errors (decreasing with frequency). The filter used is a three-pole Butterworth low-pass filter, coded following the algorithm described in [Bozic \[1980\]](#), p. 49. The digital filter used is recursive, not centered, to permit calculation during a single pass through the data. If the cutoff frequency lies where both the GPS and INS measurements are valid and are almost the same, then the detailed characteristics of the filter in the transition region (e.g., phase shift) do not matter because the complementary filters have cancelling effects when applied to the same signal. The transition frequency f_c was chosen to be (1/600) Hz (but this value can be overridden via the “defaults” file). The Butterworth filter was chosen because it provides flat response away from the transition. The resulting variables for aircraft motion, $\{VNSC, VEWC\}$, are then each the sum of two filtered signals, calculated as described in the following box:

$VNS =$ IRS-measured north component of the aircraft ground speed
 $VNS =$ IRS-measured north component of the aircraft ground speed
 $GVEW =$ GPS-measured east component of the aircraft ground speed
 $GVNS =$ GPS-measured north component of the aircraft ground speed
 $F_L() =$ three-pole Butterworth low-pass recursive digital filter

$$\{VNSC\} = \{VNS\} + F_L(\{GVNS\} - \{VNS\})$$

$$\{VEWC\} = \{VEW\} + F_L(\{GVEW\} - \{VEW\})$$

This is straightforward and effective when both sets of measurements (IRS and GPS) are available. The approach in use becomes more complicated when the GPS signals are lost, as sometimes happens in sharp turns. Then some means is needed to avoid sudden discontinuities in velocity (and hence wind speed), which would introduce spurious effects into variance spectra and other properties dependent on a continuously valid measurement of wind. To extrapolate measurements through periods when the GPS measurements are not available, a fit is determined to the difference between the best-estimate variables $\{VNSC, VEWC\}$ and the IRS variables $\{VNS, VEW\}$ for the period before GPS reception was lost, and that fit is used to extrapolate through periods when GPS reception is not available. The procedure is described in section 3.4 of ProcessingAlgorithms.pdf.

The following provides more documentation of the fit procedure used to determine the Schuler oscillation. The errors are assumed to result primarily from this oscillation, so the three-term fit

is of the form $\Delta = c_1 + c_2 \sin(\Omega_{Sch}t) + c_3 \cos(\Omega_{Sch}t)$, where Ω_{Sch} is the angular frequency of the Schuler oscillation (taken to be $2\pi/(5067\text{ s})$) and t is the time since the start of the flight. A separate fit is used for each component of the velocity and each component of the position (discussed below under LATC and LONC). The fit matrix used to determine these coefficients is updated each time step but the accumulated fit factors decay exponentially with about 30-min decay constant, so the terms used to determine the fit are exponentially weighted over the period of valid data with a time constant that decays exponentially into the past with a characteristic time of 30 min. This is long enough to determine a significant portion of the Schuler oscillation but short enough to emphasize recent measurements of the correction. The procedures for accumulating the matrices for the fit are as follows:

Define u_G as the aircraft eastward velocity measured by the GPS and u_I the corresponding velocity measured by the IRS, so that the difference is

$$\delta u = u_G - u_I$$

If Ω_S is the Schuler oscillation period, with $\Omega_S = 2\pi/T_s$ where $T_s = 5040\text{ s}$, τ_u is the time constant for the update (1800 s), t is the time from the start of the flight, and the measurement matrix is A_{ij} , then updated terms of the measurement matrix each sample period ($A'_{i,j}$) are (for δu):

$$\begin{aligned} A'_{0,1} &= A_{0,1}\left(1 - \frac{1}{\tau_u}\right) + \delta u \\ A'_{1,1} &= A_{1,1}\left(1 - \frac{1}{\tau_u}\right) + \delta u \sin(\Omega_S t) \\ A'_{2,1} &= A_{2,1}\left(1 - \frac{1}{\tau_u}\right) + \delta u \cos(\Omega_S t) \end{aligned}$$

The matrix components $A_{j,0}$ apply to the northward velocity component and so are represented by the same equations with δu replaced by δv . Similar matrices are calculated for latitude θ and longitude ϕ , based on the differences $\delta\theta$ and $\delta\phi$ between GPS and IRS measurements. The information matrix H_{ij} is calculated via

$$H_{i,j} = H_{i,j}\left(1 - \frac{1}{\tau_u}\right) + V_{i,j}$$

where $V_{0,0} = 1$, $V_{0,1} = V_{1,0} = \sin(\Omega_S t)$, $V_{0,2} = V_{2,0} = \cos(\Omega_S t)$, $V_{1,1} = \sin^2(\Omega_S t)$, $V_{1,2} = V_{2,1} = \sin(\Omega_S t) \cos(\Omega_S t)$, and $V_{2,2} = \cos^2(\Omega_S t)$. When the fit is needed, the matrix $H_{i,j}$ is inverted and the result multiplied by the measurement matrix $A_{i,j}$ to get the fit coefficients C_{ij} to use for predicting the results for δu , δv , $\delta\theta$, and $\delta\phi$ via equations like $\delta u = C_{0,1} + C_{1,1} \sin(\Omega_S t) + C_{2,1} \cos(\Omega_S t)$.

A Appendix: Conventions for uncertainty analysis

So that this document might serve as a model for future analyses of uncertainty, this appendix documents some of the conventions followed here and suggested for standardized use.

A.1 Why perform analyses of uncertainty?

When measurements are made to test scientific theories, provide input to models, or characterize nature, they are only useful if accompanied by some sense of their reliability. A key use of uncertainty analysis is to provide this sense, in as quantitative terms as can be justified. A quoted value should be considered incomplete unless accompanied by some sense of the associated uncertainty. A target is to estimate confidence limits to be associated with measurements or to be propagated to final scientific results. Although it is usually impossible in a strict statistical sense to provide formal estimates of confidence limits, this target still underlies approaches to uncertainty analysis. If those who make measurements don't characterize their reliability, others must make their own (probably less informed) evaluations.

There are additional benefits of analyzing measurement uncertainty. If an uncertainty analysis is done before an experiment, it may suggest ways to refine the experiment to minimize critical uncertainty contributions, and it should be possible to judge if the desired uncertainty is attainable. An uncertainty analysis also highlights the dominant sources of error and so can guide efforts to improve instruments.

A.2 Error, accuracy, and uncertainty

The *error* in a measurement is the difference between the measurement and the correct value of the measurand. A measurement is of little use unless there is some way of estimating how large this error may be. This estimate is called the *uncertainty*.²² The uncertainty usually can be estimated in some way from knowledge of the performance of an instrument or from calibrations, intercomparisons, or statistical analysis of repeated measurements of the same quantity.

The term *accuracy* is often used erroneously where *uncertainty* would be appropriate. *Accuracy* is determined by the presence or absence of error, not uncertainty; a measurement may by chance be accurate and still have a large uncertainty. *Measurement uncertainty* is the correct term for an estimate of the limits to the experimental error; it is incorrect to refer to this as the measurement *accuracy*, although that is unfortunately common usage. *Accuracy* is sometimes used to refer to error, not uncertainty, but because accuracy is an absolute term even this usage is best avoided. A measurement will either be accurate or not.

²²Results are sometimes classified according to their use: *indication* based only on primary measures such as sample means or correlation coefficients; *determination* based on primary and secondary statistics, so that some estimate of uncertainty is obtained; and *inference*, in which a specific mathematical model is used to assess uncertainty quantitatively. Often, a considerable amount of information about the underlying distribution must be known (or assumed) before statistical inference is possible. Experimental results are usually appropriately quoted as determinations.

A.3 Standards for evaluating uncertainty

Many different measures are used to characterize measurement error, often making it difficult to determine which interpretation should be associated with a quoted uncertainty. However, there is now an established international consensus, defined by the International Organization for Standardization (ISO) and by the US National Institute of Standards and Technology (NIST), and this or modified forms have also been adopted by many engineering societies. Acceptance of this methodology followed decades of debate within engineering societies and among international groups, and finally reached standardization through the recommendations of the International Committee on Weights and Measures. The two key publications defining these standards are the [Guide to the Expression of Uncertainty in Measurement](#) (often referred to as the “GUM”) and NIST Technical Note 1297 [1994 revision], [“Guidelines for Evaluating and Expressing the Uncertainty of NIST Measurement Results.”](#) The latter is available in full from the web link and will be the primary reference followed in this document.²³

A.4 Classification of sources of error and of uncertainty

Errors are often classified as “systematic” or “random,” the former arising from consistent and repeatable sources (like an offset in calibration) and the latter from fluctuations about the measurand that are expected to average to zero in a repeated series of measurements. The former are also called “biases” when they arise from characteristics of an instrument. It is straightforward to differentiate these error classes by this test: Random errors are reduced when an experiment is repeated many times and the results averaged together, while systematic errors remain the same. Systematic errors can be reduced by better equipment or better calibration or better experimental procedures. Figure 44 illustrates these terms.

²³While the methodology described here is consistent with recommendations from those publications, it seems appropriate in addition to advocate separate estimation of the uncertainty associated with systematic errors because the validity of such estimates often depends on judgment and so is much harder to defend than in the case of random error.

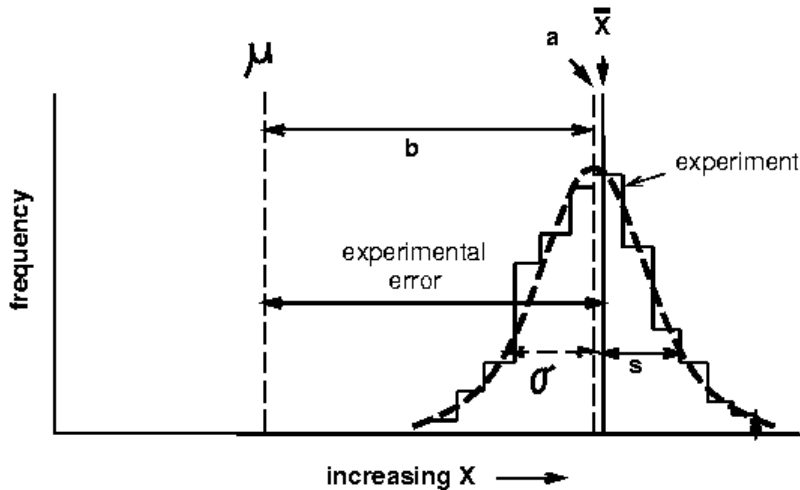


Figure 44: Illustration of the separate effects of bias errors and random errors. The true population mean is μ , but an instrument is used that has a bias b and measures with random error (in each observation) σ . The resulting estimate of the mean, obtained from \bar{x} , is in error because of the separate contributions of the bias error b and the random error in the measurement of the mean, in this case $(\bar{x} - a)$. The precision of the instrument is σ , so the estimated random error in the mean is $\sigma/N^{1/2}$. The actual error in an experiment is the difference between the true value μ and the measured value \bar{x} . The histogram represents a frequency distribution measured in a particular experiment, with mean shown as the solid line labeled \bar{x} . In a large number of observations, it would be expected that the results would tend toward the smooth dashed curve with mean $a = \mu + b$. The measured standard deviation is s , but the limiting value for a large number of measurements is expected to be σ .

It is awkward that most of the mathematical treatments of errors deal with random errors, while most errors encountered in experimental research are instead systematic errors. Digitization noise²⁴ and the errors introduced when counting finite numbers of events²⁵ are among the few good examples of random errors in modern experiments.²⁶ Analyses of uncertainty are made more difficult when most sources of uncertainty are Type-B. Evaluation of standard uncertainty for such sources is often subjective, based on judgment, and hard to quantify or defend rigorously. Repeated calibrations, intercomparisons among different instruments, and long-term stability of the calibrations can all provide information on Type-B uncertainty.

Error contributions thought to be random may really be systematic, and evaluating their associated uncertainty via Type-A methods may not reveal that dependence. An example often

²⁴I.e., the error that results when a continuously varying measurement is measured by a digital instrument that must round the measurement to the nearest digital value.

²⁵When, for example, the average measurement might be the possibly fractional value x but the actual value must be an integer.

²⁶The prevalence of systematic error is a particularly compelling reason to follow the methodology advocated here, because that approach features parallel treatment of systematic and random errors and focuses attention on their different characteristics. These separate error sources should be investigated and treated in different ways, and should be reported separately.

cited as a possible source of random error is a dependence of an instrument on line voltage, causing fluctuations in the response function of an instrument during an experiment. However, line voltage fluctuations are seldom random, and are probably biased in a particular direction relative to the conditions at the time of calibration, so it is likely that in a given experiment or series of experiments such fluctuations will introduce a bias. Furthermore, such errors are likely to be correlated in time, so the usual procedure of assuming random error contributions to be independent for different measurements will not be valid. Estimating the associated uncertainty via standard Type-A methods can thus be misleading in such a case. Close inspection of other common sources of error shows that they are often biases, and this increases the importance of estimating the associated uncertainty appropriately. Other examples will be given in later sections.

A.5 Recommended Guidelines

These are central features of the methodology recommended and used here:

1. Components introducing uncertainty are classified into two categories, Type-A and Type-B (as defined in section A.4), and *standard uncertainties* are evaluated for each component. The estimated coverage associated with these evaluations is, in the case of Type-A components, that corresponding to one standard deviation. This is not quantifiable in a manner that can be defended rigorously in the base of Type-B errors, but estimating a standard uncertainty remains a goal.
2. To obtain the combined evaluation of uncertainty resulting from the net effects of many uncorrelated sources, the standard uncertainties are combined in quadrature,²⁷ and the number of degrees of freedom in the combined uncertainty is estimated from the Welch-Satterthwaite equation (cf. (68)). For cases with correlations among components, methods that treat these correlations must be used, as specified in a subsequent section. A complete uncertainty report should also include an estimate of the number of degrees of freedom associated with the result.
3. If some standard uncertainties are asymmetrical, the positive and negative values should be combined separately to obtain separate upper and lower composite values.
4. The recommended uncertainty to be reported is the combined standard uncertainty, evaluated to represent a single standard deviation. Other estimates (e.g., that covering a specified level of confidence) can be obtained readily from this, provided that the number of degrees-of-freedom in the result is also reported.
5. [Not part of the standard:] The uncertainty report should also include separate estimates of precision and bias in the result.

An uncertainty report will normally include a tabulated list of sources of uncertainty, which should have separate sections for distinct influences like those arising from calibration, data collection, and data analysis. It is also useful to include associated estimates of precision, degrees

²⁷i.e., $s^2 = \sum_i s_i^2$.

of freedom, and bias for each contribution shown in the table. Such tabulations make it possible to isolate major sources of error, to consider the validity of other investigators' estimates of error sources, and to repeat the analyses for a new case when only one of the contributions has changed.

An important aspect of this methodology is that the degrees of freedom associated with cited estimates should be calculated and quoted. This becomes important when the number of degrees of freedom in the result is small, so that error limits and propagated errors have non-Gaussian character. Even if it is assumed that the individual measurements are distributed according to a Gaussian error distribution, the true standard deviation for an average of n samples, σ_n , is not known and must be estimated from the observations. The test statistic $t = (\bar{x} - \xi)/S_n$ (where \bar{x} is the average of n measurements, ξ is the true value of x , and S_n is the estimated standard deviation of the average \bar{x} about ξ , determined from $S_n = [\sum_{i=1}^n (x_i - \bar{x})^2 / (n(n-1))]^{1/2}$) will not be Gaussian distributed. The appropriate distribution for such averages is the Student-t distribution. The difference between the Gaussian and Student-t distributions is generally insignificant when the number of degrees of freedom²⁸ exceeds about thirty, but for small sample sizes the differences can be quite important. For this reason, when $n < 30$, the confidence limits used should be taken from the Student-t distribution rather than from the normal distribution.

Figure 45 shows the relationship between the 95% confidence limits and the t statistic for the Student-t distribution. If the final number of degrees of freedom is larger than thirty, the range to select for the precision error limit in the result is easily determined by use of the estimated standard deviation in the result, the approximate 68% confidence limit. Otherwise, it is necessary to know the effective number of degrees of freedom in the final result, as shown in Fig. 45. The Welch-Satterthwaite formula provides an estimate:

$$n_r = \frac{[\sum_i S_{Y,i}^2]^2}{\sum_i S_{Y,i}^4/n_i} \quad (68)$$

where n_r is the number of degrees of freedom in the final result, $S_{Y,i}$ is the standard deviation in Y that would result from error source i alone, and n_i is the number of degrees of freedom in that source of uncertainty.

The format advocated and followed here for an analysis of uncertainty includes these components:

²⁸In the case of an average of n values, the number of degrees of freedom is $n - 1$.

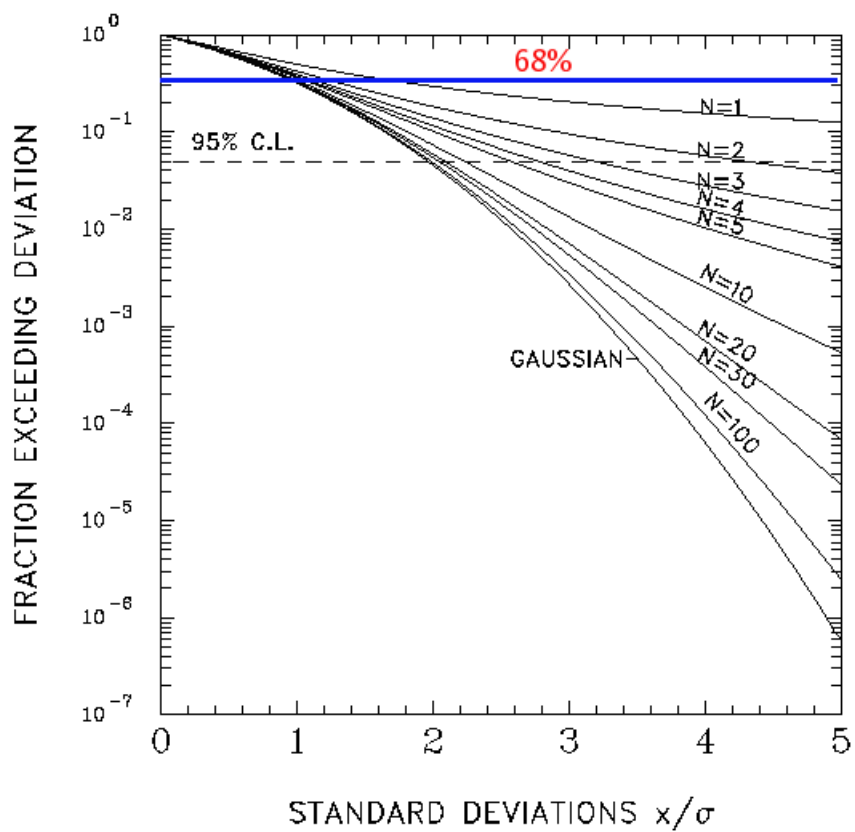


Figure 45: Confidence limits for the Student's t distribution.

1. *Description of the measurement system with discussion of the limits within which the analysis to be presented is valid.* For example, the uncertainty in measurements of wind for a research aircraft might be specified for straight-and-level flight within three hours of takeoff (because of drift of the inertial navigation system), perhaps within some altitude range. This description should discuss the calibration procedures, tests to characterize measurement uncertainty, data processing, and propagation of uncertainty to derived quantities.
2. *Tabulation and classification of the elemental sources of uncertainty.* An example will be shown in Table 2.1. Each elemental source should be listed with its associated standard uncertainty u_i and, for Type-A sources, the number of degrees of freedom (n_i). It is also convenient to tabulate the effect of the error source on the final measurement Y by including entries for $u_i(\partial Y / \partial x_i)$ in the tables, where u_i is the standard uncertainty in the uncertainty-component x_i . This simplifies propagation to the final result, although special treatment is still needed in cases where the contributions are correlated. The sources should be classified into groups contributing to calibration, data acquisition, and data processing, or into similarly meaningful groups for the instrument under consideration.
3. *Discussion of each elemental source of uncertainty in the table(s) along with a description of the basis for the evaluation.* These discussions should reflect the evidence for the tabulated values.
4. *The resulting combined standard uncertainty, combining all sources into one value.* It is also useful to combine contributions to random and systematic error (or precision and bias) into separate composite values.
5. *Summarize the results and the uncertainty limitations of the measurement.* It is helpful here to highlight the main sources of error and possible actions that could improve the measurements.

A.6 Estimating uncertainties

Like errors, estimates of *uncertainty* are also classified into two categories, “Type-A” (evaluated by statistical methods) and “Type-B” (evaluated by other means).

A.6.1 Type-A evaluation

A Type-A evaluation of uncertainty is based on statistical analysis of repeated measurements or knowledge of the statistical character of the observations. Standard statistical measures and approaches including the standard deviation, analysis of variance, propagation of error, etc., can provide the needed estimate. For example, the standard deviation s_i in repeated measurements of the same quantity leads to an estimate of standard uncertainty $u_i = s_i$. Statistical means can also provide the required estimate of the degrees of freedom associated with the standard uncertainty.

Two important points need to be made in regard to Type-A evaluations:

1. “Type-A” refers to how the estimate is obtained, not to the type of error. Type-A evaluations often result in estimates of systematic error. For example, a random error affecting calibration of an instrument can subsequently produce a systematic error when the instrument is used, but the uncertainty can still be estimated via a Type-A evaluation. This uncertainty component is therefore Type-A, even though the associated error being characterized is systematic. This has sometimes been called “fossilization” of error: The random error in the calibration procedure becomes a bias when that calibration is used.
2. Variability in a measurement may result from random measurement error, but it also may result from variability in the quantity being measured. Variations in a measurement arising from true variation in the quantity being measured cannot be used to estimate random measurement error, although they may place upper limits on that error. When using a standard deviation in repeated measurements to estimate standard uncertainty, it is necessary to correct for any contribution from natural variability.

A particularly clear example of a Type-A evaluation leading to a proper estimate of precision is that where the measurement consists of counting discrete events, such as cloud droplets or particles. The uncertainty in such measurements is expected to be characterized by Poisson statistics if the events occur at times determined from random distribution of the droplets in space.

A.6.2 Type-B evaluation

A Type-B evaluation of standard uncertainty is more dependent on judgment and experience so it is harder to defend than Type-A evaluations. Some guidance can be obtained from the following, but it must be acknowledged that these are imperfect and not quantitative, so another analyst with different judgment and experience could well disagree with the estimate. In place of statistical measures, information obtained from intercomparisons with other instruments, performance against standards, repeated calibrations, stability of the measurements, and specifications of components can all contribute to Type-B estimates of uncertainty. Nevertheless, it is useful to attempt to make Type-B evaluations that are as far as possible comparable to Type-A evaluations. For example, it is a goal that the “coverage” of the estimate be comparable to a standard deviation. The following may provide some guidance when developing such estimates:

- If the error source is expected to be within the limits $\pm a$ 50% of the time, then $u_j \approx 1.5a$.
- If it is expected to be within those limits about 2/3 of the time, then $u_j \approx a$.
- If the quantity is expected to be within those limits 100% of the time, but equally probable anywhere in this range, then use $u_j \approx a/\sqrt{3}$.
- If the limits are interpreted as 3-standard-deviation limits, then $u_j \approx a/3$. (The NIST TN and GUM provide other examples also.)

A.7 The composite or net uncertainty

The tabulated standard uncertainties should then be combined to a single standard uncertainty, u_c , which incorporates all sources of uncertainty. Where possible, degrees of freedom should also be provided. The recommended uncertainty to quote with results is the standard uncertainty u_c ; This is a departure from earlier practice, favoring standard deviations or 95% confidence limits.²⁹ NIST continues to accept such estimates also, and uses the term *expanded uncertainty* (symbol U) such that $U = 2u_c$.

A.8 Propagation of uncertainty estimates

The interesting quantities for research are often derived from the basic measurements by calculations that combine many measurements into final quantities, transform the measurements, apply filters, or otherwise convert the fundamental measurements into derived quantities. In such cases, the uncertainty characteristics of the derived quantities can become quite complicated and difficult to understand without a prescribed methodology, and serious errors in interpretation can result. For example, some attempts to derive correlations between radar reflectivity (Z) and rainfall (R) have been distorted by the problem that both are based on different calculations from the same characteristics of the drop size distributions, and hence there is a natural correlation between the two that arises purely from correlated error sources. If data sources are used that provide imprecise estimates of Z and R , a correlation will appear that is purely the result of these correlated error contributions and does not reflect a natural correlation between radar reflectivity and rainfall rate. It would be a serious error to use the correlation determined in this way to estimate rainfall from radar reflectivity.

The following develops a consistent approach, often called “error propagation,” that makes it possible to determine the uncertainty characteristics in derived quantities if the characteristics of the fundamental measurements are known. Let $\{x\} = \{x_\ell, \ell = 1, L\}$ be a set of measured quantities with known measurement uncertainties.³⁰ Consider derived quantities $\{Y\} = \{Y_m, m = 1, M\}$, each of which is a function of the measured quantities $\{x\}$:

$$Y_m = Y_m(x_1, x_2, \dots, x_L) \text{ or } \mathbf{Y} = \mathbf{Y}(\mathbf{x}). \quad (69)$$

The mean values of x_ℓ , \bar{x}_ℓ , are then the “best” values for x_ℓ in the sense that they minimize the squares of the deviations from these best values. In the same sense, the “best” values for Y_m are the values $Y_m(\bar{x}_1, \bar{x}_2, \dots, \bar{x}_L)$.³¹

The one-standard-deviation uncertainties in $\{Y\}$ are those that represent the range over which $\{Y\}$ can vary while $\{x\}$ remain within one-standard-deviation of their measured values. For small deviations, a first-order Taylor expansion relates deviations in $\{Y\}$ to deviations in $\{x\}$:

$$Y_m(x_1, x_2, \dots, x_L) = Y_m(\bar{x}_1, \bar{x}_2, \dots, \bar{x}_L) + \sum_{k=1}^L \frac{\partial Y_m(x_1, x_2, \dots, x_L)}{\partial x_k} \Big|_{\bar{x}} (x_k - \bar{x}_k). \quad (70)$$

²⁹“Confidence limits” should only refer to Type-A evaluations; the term “coverage probability” is sometimes used to emphasize the difference between Type-B evaluations and those obtained via statistical analysis.

³⁰Brackets denote multidimensional quantities and bold-face symbols denote matrices.

³¹These values do not necessarily minimize the sum of the squared deviations from $\{\bar{Y}\}$, the derived quantities, unless the relationship to the measured quantities is linear.

The variance in Y_m is then obtained by averaging over the N measurements, indicated by index i :

$$V_{Y_m Y_m} = \frac{1}{N} \sum_{i=1}^N (Y_m(\{x\}_i) - Y_m(\{\bar{x}\}))^2 \quad (71)$$

$$= \frac{1}{N} \sum_{i=1}^N \left[\left(\sum_{j=1}^L \frac{\partial Y_m}{\partial x_j} \Big|_{\bar{x}} (x_i - \bar{x}_j) \right) \left(\sum_{k=1}^L \frac{\partial Y_m}{\partial x_k} \Big|_{\bar{x}} (x_k - \bar{x}_i) \right) \right] \quad (72)$$

$$= \sum_j \sum_k \frac{\partial Y_m}{\partial x_j} \Big|_{\bar{x}} \frac{\partial Y_m}{\partial x_k} \Big|_{\bar{x}} \left(\frac{1}{N} \sum_i (x_{ji} - \bar{x}_j)(x_{ki} - \bar{x}_k) \right). \quad (73)$$

The matrix elements

$$H_{jk}^{-1} = \frac{1}{N} \sum_{i=1}^N (x_{ji} - \bar{x}_j)(x_{ki} - \bar{x}_k) \quad (74)$$

entering (73) are the variances and covariances of the measured quantities, so \mathbf{H}^{-1} is called the *covariance matrix* or the *error matrix*. If the relationship between $\{Y\}$ and $\{x\}$ is linear or is assumed linear (as in the first-order Taylor expansion) over the range of fluctuations, then this matrix is particularly useful for determining the variances in derived quantities because those variances can be expressed as

$$V_{Y_m Y_n} = \langle (Y_m - \bar{Y}_m)(Y_n - \bar{Y}_n) \rangle \quad (75)$$

$$= \sum_{j=1}^L \sum_{k=1}^L \frac{\partial Y_m(x)}{\partial x_j} \Big|_{x=\bar{x}} \frac{\partial Y_n(x)}{\partial x_k} \Big|_{x=\bar{x}} H_{jk}^{-1} \quad (76)$$

or, in matrix notation,

$$V = T^t H^{-1} T \quad (77)$$

where $T_{mj} = \partial Y_m / \partial x_j$ is the element of the (column) matrix of derivatives of the derived quantity Y_m with respect to the measured quantity x_j and the superscript t denotes the transpose matrix. This general form is valid for any correlations among the original measurements (which will be represented by off-diagonal elements of H) and properly represents the correlations among dependent variables.

EXAMPLE 0.1: A thermocouple can be used to measure temperature, because a junction between two metals will produce a voltage difference in the two metals that is dependent on (and nearly proportional to) the temperature of the junction. A common experimental set-up is shown in Fig. 46.

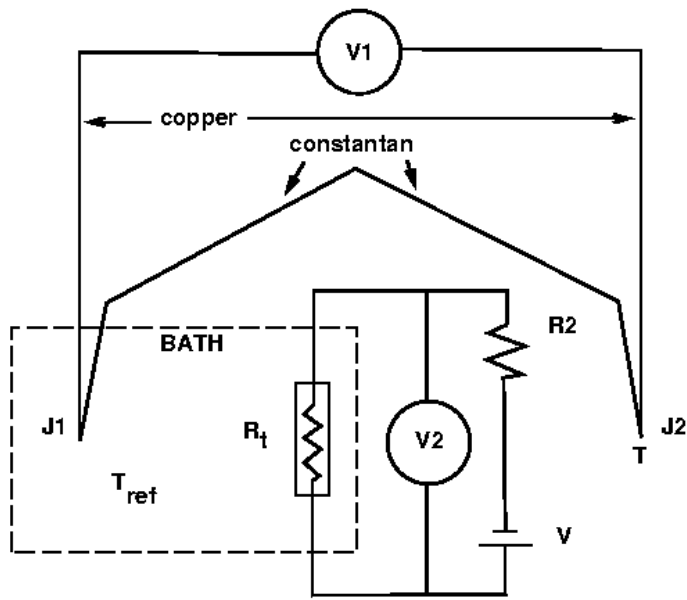


Figure 46: *Experimental configuration for measuring temperature with a thermocouple. Junctions J1 and J2 are junctions between copper and constantan wire, so the voltage V1 is a measure of the temperature difference between T and T_{ref}. A thermistor R_t measures the bath temperature via the voltage V2, and so provides a reference temperature to be added to the temperature difference measured by the thermocouple.*

The thermocouple junctions both produce voltage differences, dependent respectively on the temperature T and on the reference bath temperature T_{ref} . The reason for using this arrangement is that both the wires leading to the instrument measuring the voltage V are then copper wires, and can connect to copper junctions at the voltmeter without introducing additional contact potentials such as would result if the constantan wire were connected directly to the voltmeter. The uncertainty in T is then caused by two sources: (a) the uncertainty in the measurement of $\Delta T = T - T_{ref}$, and (b) the uncertainty in T_{ref} . Often, a thermistor is used to measure the temperature of the reference bath (or of a metal block used in the same way).

If a thermistor is used to determine the temperature of the reference junction, as shown, there are two voltages that must be measured to determine the unknown temperature T : V_1 , produced by the pair of thermocouples, and V_2 , produced by the thermistor. These are related to the temperature difference $\Delta T = (T - T_{ref})$ and to T_2 , the temperature of the thermistor junction, by functions Y_1 and Y_2 , which often are almost linear relationships:

$$\Delta T = Y_1(V_1) = a_1 V_1 \quad (78)$$

$$T_2 = Y_2(V_2) = a_2 V_2. \quad (79)$$

Then the first two fundamental quantities affecting the measurement, in the earlier notation, are $x_1 = V_1$ and $x_2 = V_2$.

If V_1 and V_2 are measured by the same voltmeter, part of the uncertainty in V_2 will be correlated with that in V_1 because bias in the voltmeter will affect both measurements in the same way. This will be reflected in off-diagonal terms in the error matrix, representing correlations between errors in V_1 and V_2 .

There will also be an error in the measurement of T introduced by the assumption that $T_{ref} = T_2$, because the temperature bath or constant-temperature block may not be uniform in temperature. Another function $Y_3 = x_3 = T_{ref} - T_2$ can be introduced to account for this error source, which probably will be a systematic error. The measurement T is then determined from

$$T = \Delta T + (T_{ref} - T_2) + T_2 = Y_1(V_1) + Y_2(V_2) + Y_3. \quad (80)$$

Suppose that the voltmeter has a precision of S_i and a systematic error of B_i when measuring V_i , and that the random errors are uncorrelated but the bias errors are always the same (as might occur for a calibration error). If the only sources of error are these random and systematic errors and a non-zero value of Y_3 , the error matrix for the random component of the uncertainty is

$$H_r^{-1} = (S_1^2) \quad (81)$$

and the bias component is

$$H_s^{-1} = ((B_1^2)) \quad (82)$$

when expressed in terms of the fundamental quantities x_1 , x_2 , and x_3 representing the two measurements and the unmeasured difference between T_{ref} and T_2 .

The sum of these matrices can be used in (77) to evaluate the variance in the measured temperature:

$$V_{TT} = (a_1) (S_1^2 + B_1^2) \begin{pmatrix} a_1 \\ a_2 \\ 1 \end{pmatrix} \quad (83)$$

$$= a_1^2 S_1^2 + a_2^2 S_2^2 + (a_1 B_1 + a_2 B_2)^2 + B_3^2. \quad (84)$$

The first two terms show that the random contributions add to the net variance in quadrature, as expected for independent error sources. The next term shows that the bias contributions, however, add linearly. This results because a bias error affects measurements of ΔT and T_2 in the same way, so the error enters the final result additively.

A.9 Monte Carlo techniques

Sometimes the functional relationships are so complex or non-linear that the preceding analytical formulas are unwieldy. In such cases, an alternative is to employ what is conventionally called a *Monte Carlo* technique. In this approach, the measured quantities are varied randomly in ways that represent the experimental uncertainties, and the calculations leading to the final answer are repeated with these artificial quantities. This is done repeatedly, and the variances and covariances in the resulting final answers are calculated. Random number generators are

available on computer systems that generate variables having zero mean, unity variance, and a Gaussian probability distribution. Correlated fluctuations can be represented by defining linear combinations of such independent variables. In cases where the error propagation is especially complex (e.g., where the final answer might depend on non-linear fits to the input data), Monte Carlo techniques may be the only feasible way of determining the uncertainty in the final result.

A.10 Reference Material

This section provides, for reference, specific definitions of some of the other terms used in the analysis of uncertainty. This information is included here because this terminology is sometimes in conflict with nonscientific usage and is not always used consistently even in scientific papers.

With many of these terms, it is necessary to distinguish between the characteristics of a *parent* distribution and the estimates of those characteristics obtained from a specific sample from the parent population. For example, one may want to estimate characteristics of the parent population from measurements taken on only a specific subset from that population. A common convention, followed here, is to use Greek letters for population characteristics and Roman letters for sample characteristics. Thus, for example, \bar{x} will denote the average of a set of measurements, but μ will denote an average characteristic of the underlying population.

Precision is a measure of reproducibility or scatter in the results, without regard for the accuracy of the result. It is a measure of random error only; systematic errors will not affect the precision of a result, although they do affect the accuracy.

The *mean* of a set of measurements $\{x_1, x_2, \dots, x_N\}$ is the average:

$$\bar{x} = \frac{1}{N} \sum_{i=1}^N x_i. \quad (85)$$

The *expectation value* of a quantity is the value expected if averaged over the entire parent population, and will be denoted by angle brackets: $\langle \rangle$. For example, the mean in the parent population that corresponds to the sample mean x is

$$\mu = \langle x \rangle = \lim_{N \rightarrow \infty} (\bar{x}). \quad (86)$$

There is an important distinction to be made between the standard deviation characterizing the random error of a measurement and the standard deviation characterizing a set of accurate observations and hence reflecting physical reality. The latter is often encountered in experimental research, and pertains to the natural variability in the parameter being measured; e.g., the temperature may really vary when measured over a path through the atmosphere. The former represents the precision with which a constant value of that parameter could be measured in a particular experiment. For example, in experiments using airborne instrumentation variance spectra for measured variables seldom show evidence of noise except at low levels that correspond to digitization noise. This indicates that random measurement errors seldom contribute significantly to the uncertainty in such a measurement. However, there usually is high natural variability that causes repeated sets of measurements in presumably identical conditions to vary

significantly, and the standard deviations among repeated measurements of, for example, fluxes of water vapor are large. This standard deviation reflects natural variability, not the random error in the measurement. It results from the variability of particular samples about the underlying population mean, and that variability would still characterize measurements from error-free sensors.

The *median* is the value that divides the population into equal halves; i.e., half the members lie above and half below the median. The *most probable value* is that observed most frequently, sometimes referred to as the *mode* of a distribution. As an example, the expected distribution of time intervals between randomly occurring events is

$$N(t) = N_0 e^{-t/\tau} \quad (87)$$

where $N(t)$ is the number of events per time interval that occur at time t , N_0 is the total number of events, t is the time, and τ is a time constant characterizing the process. For this distribution, the mean time is τ , the median time is $\tau \ln(2)$, and the mode occurs for $t=0$.

A *deviation* δ is the difference between a specific measurement or value and the mean. The *standard deviation* σ is the “root-mean-square” value of the deviations, obtained from

$$\sigma = \left[\lim_{N \rightarrow \infty} \left(\frac{1}{N} \sum_{i=1}^N (x_i - \mu)^2 \right) \right]^{\frac{1}{2}}. \quad (88)$$

For a sample of measurements, the conventional estimate s of the population standard deviation σ is

$$s = \left[\frac{1}{N-1} \sum_{i=1}^N (x_i - \bar{x})^2 \right]^{\frac{1}{2}}. \quad (89)$$

The *variance* is the average of the squares of the deviations, or the square of the standard deviation.

If x_j is a possible observation, the observed fraction of observations having the value x_j is $P(x_j) = N(x_j)/N$ where N is the total number of observations and $N(x_j)$ is the number having value x_j . The underlying population distribution function is then

$$\Phi(x_j) = \lim_{N \rightarrow \infty} P(x_j). \quad (90)$$

The preceding quantities can then be expressed in terms of the distribution function; for example, the mean is

$$\mu = \sum_{j=1}^N x_j \Phi(x_j) \quad (91)$$

and the variance is

$$\sigma^2 = \sum_{j=1}^N (x_j - \mu)^2 \Phi(x_j) = \left(\sum_{j=1}^N x_j^2 \Phi(x_j) \right) - \mu^2 = \langle x^2 \rangle - \mu^2. \quad (92)$$

The extensions to continuous distribution functions are these:

$$\sum_j P(x_j) \rightarrow \int P(x) dx \quad (93)$$

$$\mu = \int_{-\infty}^{\infty} x\Phi(x)dx \quad (94)$$

$$\sigma^2 = \int_{-\infty}^{\infty} (x - \mu)^2\Phi(x)dx. \quad (95)$$

Similarly, the expectation value for any function f of measurable characteristics x is

$$\langle f(x) \rangle = \int f(x)\Phi(x)dx \quad (96)$$

where x can be a set of variables and the multidimensional integration must then cover all possible values of x .

Other characteristics sometimes cited are the *probable error*, the magnitude of the deviation exceeded by 50% of the deviations, and the *average deviation*, the expectation value for the absolute magnitude of the deviations. For a Gaussian distribution, the probable error, average deviation, and standard deviation have the ratios 0.674:0.800:1.

If the distribution in measurement errors follows a known probability distribution, then *confidence intervals* determined from that distribution can be used to obtain quantitative estimates of probabilities associated with such errors. It is this relationship that establishes the often used correspondence between standard deviation and probability, for the Gaussian distribution. Specifically, measurements falling more than two standard deviations ($\pm 2\sigma$) from the true value are expected with about 0.05 probability, so 2σ limits correspond to approximate limits providing 95% coverage. Other distribution functions can be treated in the same way.

B Appendix: Reproducibility

This document is constructed in ways that support duplication of the study. The processing programs are incorporated into the same file that generates this document, using principles and techniques described by Xie [2013] as implemented in the R package 'knitr' (Xie [2014]). The core program, 'WindUncertainty.Rnw', is archived on 'GitHub' in the directory at [this URL](#). There is some supplemental material in that directory, like the bibliography and many code segments saved in the 'chunks' subdirectory, so the full directory should be downloaded in order to run the program. The calculations use the programming language R (R Core Team [2013]) and were run within RStudio (RStudio [2009]), so this is the most straightforward way to replicate the calculations and the generation of this document.

A package named Ranadu, containing auxillary functions, is used extensively in the R code. It is available on GitHub as <https://github.com/WilliamCooper/Ranadu.git>. The specific version used for calculations in this report is included in the 'zip' archive listed below.

The data files used are also preserved in the NCAR High Performance Storage System (HPSS) in files that are available, and they can be provided via a request to <mailto:mailto:raf-dm@eol.ucar.edu>. The original files representing the data as produced by the NCAR Earth Observing Laboratory, Research Aviation Facility, were in netCDF format (cf. [this URL](#)), but in many cases special reprocessing was used and the files may change after reprocessing so a separate archive is maintained for this document. The data files in this archive represent R data.frames and are preserved as binary-format 'Rdata' files via R 'save' commands. The code in the GitHub archive has appropriate 'load' commands to ingest these data files from a subdirectory named 'Data' but this is not part of the GitHub repository because it is too large to be appropriate there. To reproduce this research, those data files have to be transferred separately from the NCAR HPSS to the 'Data' directory.

Extensive use has been made of attributes assigned to the data.frames and the variables in those data.frames. All the attributes from the original netCDF files have been transferred, so there is a record of how the original data were processed, for example recording calibration coefficients and processing chains for the variables. Once the data.frames are loaded into R, these attributes can be viewed and provide additional documentation of what data were used. Key information like the processing date, the program version, and the selection of primary variables is thus preserved.

PROJECT:	WindUncertainty
ARCHIVE PACKAGE:	WindUncertainty.zip
CONTAINS:	attachment list below
PROGRAM:	WindUncertainty.Rnw
ORIGINAL DATA:	/scr/raf_data/DEEPWAVE/
GIT:	https://github.com/WilliamCooper/WindUncertainty.git

Attachments: WindUncertainty.Rnw
WindUncertainty.pdf
chunks/*
SessionInfo
Ranadu_2.1-15-3-8.tar.gz

Acknowledgments

The analyses reported here were mostly performed using R³²R Core Team [2013], with RStudio³³ RStudio [2009] and knitr³⁴ Xie [2013, 2014]. Substantial use also was made of the ggplot2 package³⁵ Wickham [2009] for R.

³²R Core Team (2014). R: A language and environment for statistical computing. R Foundation for Statistical Computing, Vienna, Austria. URL <http://www.R-project.org/>.

³³RStudio (2012). RStudio: Integrated development environment for R (Version 0.98.879) [Computer software]. Boston, MA. Available from <http://www.rstudio.org/>

³⁴Xie, Y. (2013), “knitr: A general-purpose package for dynamic report generation in R. R package version 1.3,” Version 1.6 was used for this work. See also Xie, Y (2014), “Dynamic documents with R and knitr,” CRC Press, Chapman and Hall, 190 pp.

³⁵H. Wickham. ggplot2: elegant graphics for data analysis. Springer, New York, 2009.

References

- S. M. Bozic. *Digital and Kalman filtering: An introduction to discrete-time filtering and optimum linear estimation*. John Wiley and Sons, New York, NY, USA, 1980. ISBN 978-0713134100.
- W. A. Cooper, S. M. Spuler, M. Spowart, D. H. Lenschow, and R. B. Friesen. Calibrating airborne measurements of airspeed, pressure and temperature using a doppler laser air-motion sensor. *Atmospheric Measurement Techniques*, 7(9):3215–3231, 2014. doi: 10.5194/amt-7-3215-2014. URL <http://www.atmos-meas-tech.net/7/3215/2014/>.
- D. H. Lenschow. The measurement of air velocity and temperature using the NCAR Buffalo Aircraft Measuring System. Technical report, 1972. URL <http://nldr.library.ucar.edu/repository/collections/TECH-NOTE-000-000-000-064>.
- D. H. Lenschow and P. Spyers-Duran. Measurement techniques: air motion sensing. Technical report, 1989. URL <https://www.eol.ucar.edu/raf/Bulletins/bulletin23.html>.
- W. H. Press, S. A. Teukolsky, W. T. Vetterling, and B. P. Flannery. *Numerical Recipes in C (2nd Ed.): The Art of Scientific Computing*. Cambridge University Press, New York, NY, USA, 1992. ISBN 0-521-43108-5.
- R Core Team. *R: A language and environment for statistical computing*. R Foundation for Statistical Computing, Vienna, Austria, 2013. URL <http://www.R-project.org>.
- RStudio. *RStudio: Integrated development environment for R (Version 0.98.879)*, 2009. URL <http://www.rstudio.org>.
- M. Schuler. The perturbation of pendulum and gyroscope instruments by acceleration of the vehicle. *Physik. Z.*, 24(16):344–357, 1923. URL <http://www.webcitation.org/6JBR8WNRq>.
- S. M. Spuler, D. Richter, M. P. Spowart, and K. Rieken. Optical fiber-based laser remote sensor for airborne measurement of wind velocity and turbulence. *Appl. Optics*, 50(6):842–851, FEB 20 2011. ISSN 1559-128X. doi: 10.1364/AO.50.000842.
- H. Wickham. *ggplot2: elegant graphics for data analysis*. Springer New York, 2009. ISBN 978-0-387-98140-6. URL <http://had.co.nz/ggplot2/book>.
- Y. Xie. *Dynamic Documents with R and knitr*. Chapman and Hall/CRC, Boca Raton, Florida, 2013. URL <http://yihui.name/knitr/>. ISBN 978-1482203530.
- Y. Xie. *knitr: A general-purpose package for dynamic report generation in R*, 2014. URL <http://yihui.name/knitr/>. R package version 1.6.